Copyright Warning & Restrictions

The copyright law of the United States (Title 17, United States Code) governs the making of photocopies or other reproductions of copyrighted material.

Under certain conditions specified in the law, libraries and archives are authorized to furnish a photocopy or other reproduction. One of these specified conditions is that the photocopy or reproduction is not to be "used for any purpose other than private study, scholarship, or research." If a, user makes a request for, or later uses, a photocopy or reproduction for purposes in excess of "fair use" that user may be liable for copyright infringement,

This institution reserves the right to refuse to accept a copying order if, in its judgment, fulfillment of the order would involve violation of copyright law.

Please Note: The author retains the copyright while the New Jersey Institute of Technology reserves the right to distribute this thesis or dissertation

Printing note: If you do not wish to print this page, then select "Pages from: first page # to: last page #" on the print dialog screen

NJIT
New Jersey's Science &
Technology University

The Van Houten library has removed some of the personal information and all signatures from the approval page and biographical sketches of theses and dissertations in order to protect the identity of NJIT graduates and faculty.

ABSTRACT

NEW FULL WAVE THEORY FOR PLANE WAVE SCATTERING BY A ROUGH DIELECTRIC SURFACE –THE FICTITIOUS CURRENT METHOD

by
Byung-Tae Yoon

A new full wave method for scattering of plane waves from a rough dielectric surface is developed. This new theory begins by postulating a zero–order field solution which does not satisfy Maxwell's source–free field equations. The zero-order field, however, is made to satisfy Maxwell's source equations. This is done by introducing a fictitious volume current distribution. Since the original problem does not possess a volume current distribution, its introduction represents a measure of the error in the postulated zero-order solution. To improve this solution, the fictitious volume current distribution is cancelled by the introduction of a second fictitious current distribution, consisting of an infinite number of fictitious sheet current densities. Each sheet current distribution meanwhile produces a mode field that does not satisfy Maxwell's source-free equations. To insure that the mode fields are electromagnetic fields, they are required to satisfy Maxwell's equations with sources; this dictates the introduction of fictitious first-order volume current distributions. The superposition of the mode fields constitutes the first-order solution. The procedure is continued so as to generate a series solution. The theory is developed for both TE- and TM- polarization.

This new full wave theory is shown to yield good agreement with Method of Moments (MoM) solutions, which are extremely accurate but computationally intensive, whereas the new full wave theory provides a formula with a single integration. The new

theory is applied to both random rough surfaces and deterministic rough surfaces. The solution in first-order satisfies reciprocity and the theory intrinsically provides an error criterion to assess its accuracy. The results are also shown to yield the correct solution for plane wave scattering from perfect metal rough surfaces. This new full wave method for scattering by a dielectric rough interface provides enhanced physical insight and permits a systematic procedure for obtaining higher-order terms in the series representation of the scattered field.

NEW FULL WAVE THEORY FOR PLANE WAVE SCATTERING BY A ROUGH DIELECTRIC SURFACE –THE FICTITIOUS CURRENT METHOD

by
Byung-Tae Yoon

A Dissertation
Submitted to the Faculty of
New Jersey Institute of Technology
in Partial Fulfillment of the Requirements for the Degree of
Doctor of Philosophy in Electrical Engineering

Department of Electrical and Computer Engineering

May 2003

Copyright © by Byung-Tae Yoon

ALL RIGHTS RESERVED

APPROVAL PAGE

NEW FULL WAVE THEORY FOR PLANE WAVE SCATTERING BY A ROUGH DIELECTRIC SURFACE –THE FICTITIOUS CURRENT METHOD

Byung-Tae Yoon

Dr. Gerald M. Whitman, Dissertation Advisor — Date
Director, Center for Microwave and Lightwave Engineering, NJIT

Dr. Felix K. Schwering, Committee Member — Date
Chief Scientist, U.S. Army CECOM, retired

Dr. Gregory A. Kriegsmann, Committee Member — Date
Professor, Department of Mathematical Sciences, NJIT

Dr. Haim Grebel, Committee Member — Date
Professor, Department of Electrical and Computer Engineering, NJIT

Dr. Edip Niver, Committee Member — Date
Associate Professor, Department of Electrical and Computer Engineering, NJIT

Dr. Ali Abdi, Committee Member — Date
Assistant Professor, Department of Electrical and Computer Engineering, NJIT

BIOGRAPHICAL SKETCH

Author: Byung-Tae Yoon

Degree: Doctor of Philosophy

Date: May 2003

Undergraduate and Graduate Education:

- Doctor of Philosophy in Electrical Engineering,
  New Jersey Institute of Technology, Newark, NJ, 2003

- Master of Science in Electrical Engineering,
  Polytechnic University, Brooklyn, NY, 1998

- Bachelor of Science in Electronic Engineering,
  Kyungpook National University, Daegu, Korea, 1988

Major: Electrical Engineering

to eunsook

ACKNOWLEDGEMENT

I extend my deepest gratitude to Dr. Gerald Whitman for his great guidance about science and life. A debt of gratitude is owed to Dr. Felix Schwering for his ideas in this research. I would also thank to my dissertation committee members, Dr. Gregory Kriegsman, Dr. Haim Grebel, Dr. Edip Niver and Dr. Ali Abdi, whose comments were greatly appreciated. I would also like to give my special thanks to New Jersey Center for Wireless Telecommunications that offered me the grants for this research.

This work would not have been possible if not for my wife, Eunsook, who gave me the courage to go on. I thank her.

TABLE OF CONTENTS

TABLE OF CONTENTS
(Continued)

LIST OF FIGURES

LIST OF FIGURES
(Continued)

Figure **Page**

LIST OF FIGURES
(Continued)

Figure **Page**

CHAPTER 1

INTRODUCTION

Since all real surfaces are rough, scattering from such surfaces is of interest in many diverse research areas, such as, optics, spectroscopy, radio-astronomy, remote sensing, physics of solids, sonar detection, medical ultra-sonic, radar imaging and communication theory. As such, an extensive number of journal publications exists on the subject. Lord Rayleigh first undertook the study of rough surface scattering in 1877 and since 1950 an intensified development has occurred to address this important problem. At present, all analytical methods that have been developed to study rough surface scattering have yielded approximate solutions that apply over a limited range of surface parameters. Hence, the general scattering problem still remains an unsolved problem and strong interest persists to develop new analytical approaches to obtain better solutions.

In the research here, a new full-wave method for scattering by one-dimensional dielectric rough surfaces is developed for TE- and TM- polarization. In Chapter 2, the new full-wave method is formulated and used to treat the specific case of TE polarization. The method consists of initially postulating a zero-order field solution, called the primary field, at the local elevation of the rough surface. The postulated primary or zero-order field solution satisfies all boundary conditions but does not satisfies Maxwell's source-free equations. The primary field, however, does satisfy Maxwell's equations but with current sources. Since these current densities are not physically present in the original problem, they are referred to as fictitious primary volume current densities. These fictitious volume current densities have to be eliminated in order to obtain the field

solution to the original problem. This is accomplished by introducing fictitious first-order sheet current densities to fill the region where the primary volume current densities exist. The sheet current densities are taken such that they cancel the fictitious volume current sources. The sheet currents are generated by constructing appropriate modal fields. These wave fields satisfy the boundary conditions and Maxwell's equations with source and form a complete, orthogonal system. A superposition of these modal fields yields the first-order field solution. When added to the primary field solution, an approximate expression for the total field is obtained both above and below the rough surface. The modal fields satisfy Maxwell's equations with first-order fictitious volume current sources. These first-order volume current sources must be smaller that the primary volume current sources in order for the method to yield a good approximate series solution that converges.

The field solution for the TM polarization case is obtained in a similar fashion as the TE case and is described in Chapter 3. While the primary field of the TE case satisfies the rough surface boundary conditions, the primary field of the TM case requires the introduction of fictitious surfaces currents to insure satisfaction of the surface boundary conditions. Hence, obtaining the scatter field for the TM case is more involved. Verification of this new full wave theory for both polarization is presented in Chapter 4, where the scatter fields are shown to satisfy reciprocity and to reduce to the correct solutions for the case of plane wave scattering from a perfectly conducting rough surface. An error criterion is also developed.

Numerical results are presented in Chapter 5. The new full wave theory is compared to patterns determined by using a purely numerical method. The numerical

method called the Method of Moments (MoM) is used to evaluate the rigorous integral equations for both TE- and TM- polarization. Comparisons are presented for two different surface characterizations, Gaussian random surfaces and deterministic surfaces. Data for the scatter patterns resulting from random surfaces were produced using the Monte Carlo method. It is shown through these comparisons that the fictitious current method produces results that agree very well with the results generated by the Method of Moments.

CHAPTER 2

THE TE CASE

An obliquely incident TE polarized monochromatic electromagnetic plane wave is assumed to be scattered by a one-dimensional dielectric rough surface that separates air from an ideal dielectric. Scattered fields exist both in the air region and in the dielectric

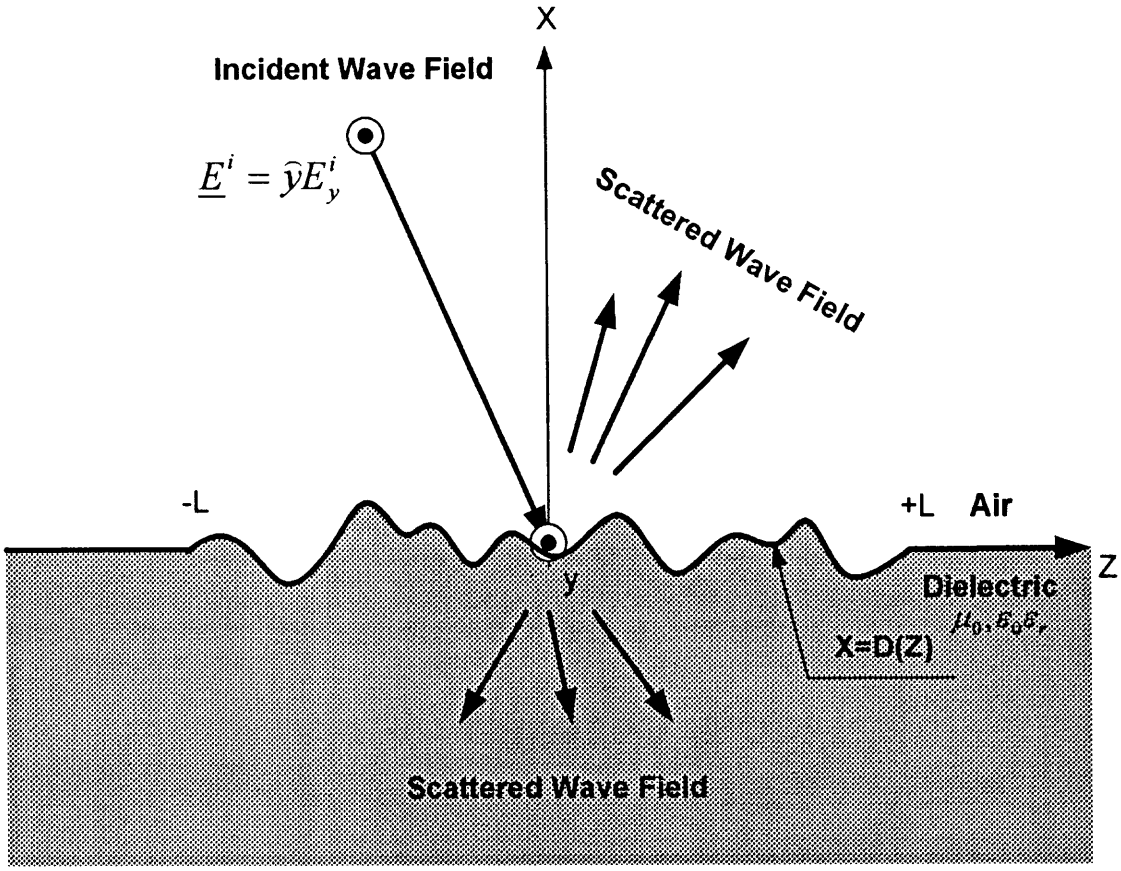

Figure 2.1 The physical geometry under consideration.

region. The physical geometry under consideration is two-dimensional with no variation along the y-axis and is shown in Figure 2.1. A finite rough surface segment is shown to lie in the range from $z = -L$ to $z = +L$. The surface is arbitrary and is specified by the

profile $x=D(z)$ with the constraints $D(\pm L)=D'(\pm L)=0$, where the prime indicates differentiation with respect to z. The region $x < D(z)$ is filled with a lossless dielectric with dielectric constant ε_r.

To be a solution, the total field must satisfy both the time-harmonic source free Maxwell's equations and all boundary conditions. The initial postulate for the total field solution, i.e., the primary or zero-order field, is obtained by requiring first that the boundary conditions be satisfied. This field is chosen to satisfy the boundary conditions, but does not satisfy the Maxwell's source free equations. However, the primary field satisfies Maxwell's equations with fictitious volume current densities given, in general, by

$$\nabla \times \boldsymbol{E} = -j\omega\mu_0 \boldsymbol{H} - \boldsymbol{M} \tag{2.1a}$$

$$\nabla \times \boldsymbol{H} = j\omega\varepsilon \boldsymbol{E} + \boldsymbol{J} \tag{2.1b}$$

$$\nabla \cdot \boldsymbol{E} = 0 \tag{2.1c}$$

$$\nabla \cdot \boldsymbol{H} = 0 \tag{2.1d}$$

For the TE polarization case, the fictitious electric volume current density $\boldsymbol{J}$ is non-zero while the fictitious magnetic volume current density is zero. The volume currents do not exist physically, but are needed to support the primary field. To obtain a solution to the original problem depicted in Figure 2.1, these current distributions have to be eliminated. This is accomplished by introducing a second fictitious current distribution of equal magnitude but 180° out of phase with the primary volume current density.

This second fictitious current distribution consists of a superposition of orthogonal sheet currents, chosen such that they form a complete, orthogonal system. Each sheet current lies in a plane at $z = z_1$ ($-L \le z_1 \le L$, $-\infty < x < \infty$) and is defined by a postulated modal field structure. More details will be presented in Section 2.2.

2.1 Primary Field

The expression for the primary or first-order field due to scattering from the rough surface defined above is inferred by the structure of the field scattered from a planar or flat surface that is prescribed by the surface profile $x=D$=constant. This auxiliary problem, i.e., the determination of the field above and below a planar interface between air and a dielectric that results when an obliquely incident TE polarized plane wave from air strikes an ideal dielectric is well known. The rigorous solution to this scatter problem consists of incident, reflected and transmitted plane waves. This wave set satisfies the boundary conditions of continuity of both the tangential electric field and tangential magnetic field at the planar surface. A similar field structure for the rough surface profile $x=D(z) \neq 0$ is then postulated. The incident electric field is the same for both cases, but the reflected and transmitted electric fields are modified to include the surface profile $D(z)$. As is shown below, the plane wave set for the rough surface profile ($x=D(z) \neq$ constant) reduces to the plane wave set for the planar dielectric surface adjusted to the local elevation D =constant.

For the rough surface, the primary wave field is assumed to be expressed as

$$E_{ya}^{p} = E_y^i + E_y^r \quad , \quad x > D(z) \tag{2.2a}$$

$$E_{yb}^{p} = E_{y}^{t} \qquad , \; x < D(z) \tag{2.2b}$$

where subscript a and b denote above the interface in air and below the interface in the dielectric, respectively. The geometry and the primary wave field are shown in Figure 2.2, where D=$D(z)$.

The incident wave in air is assumed to be

$$\underline{E}^{i} = \hat{y}E_{y}^{i} = \hat{y}E_{0}^{i}e^{-j\beta_0 z + ju_0 x} \tag{2.3}$$

where β_0 and u_0 are the z and x components of the incident wave vector with magnitude

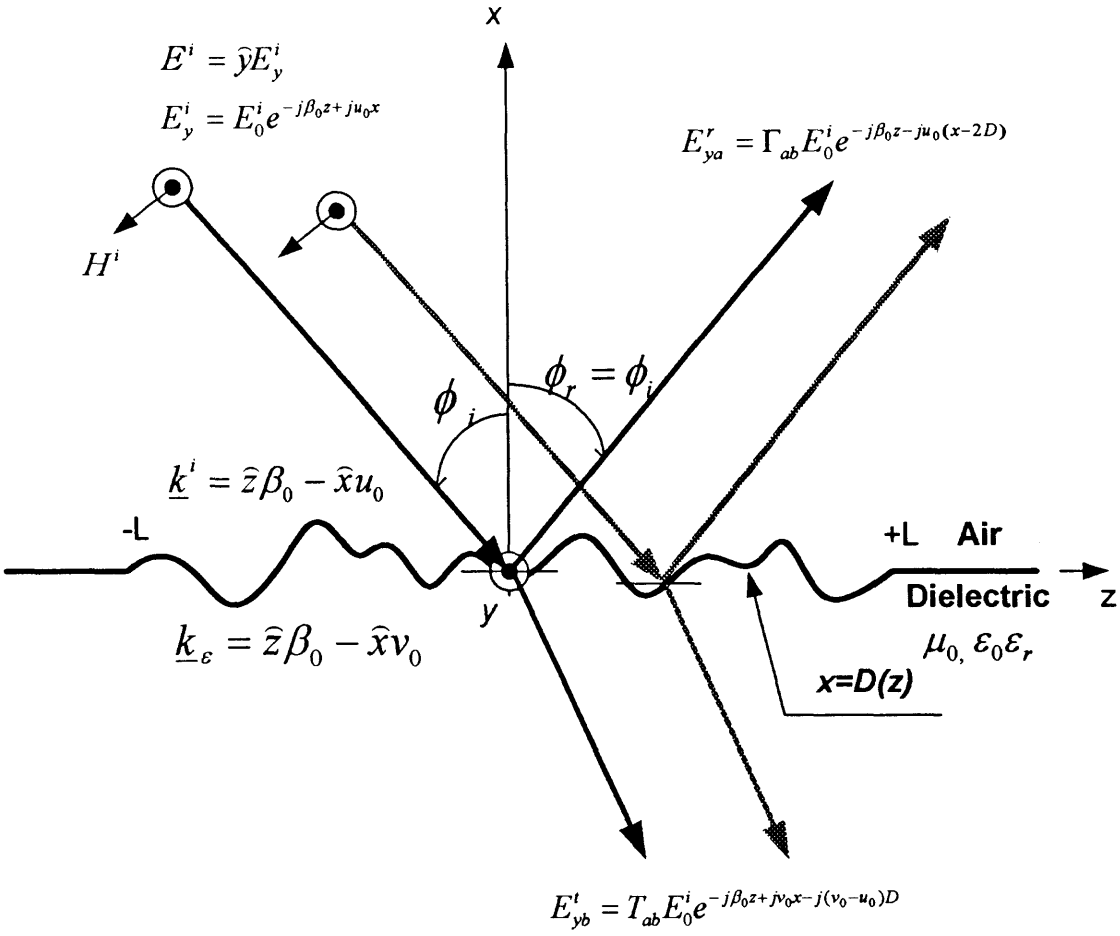

Figure 2.2 Geometry and primary wave field.

k_0 in air, respectively. In the TE-case, Maxwell's equations with source terms reduce to

$$\frac{\partial E_y}{\partial z} = jk\eta H_x + M_x \tag{2.4a}$$

$$\frac{\partial E_y}{\partial x} = -jk\eta H_z - M_z \tag{2.4b}$$

$$\eta\left[\frac{\partial H_x}{\partial z} - \frac{\partial H_z}{\partial x}\right] = jkE_y + \eta J_y \tag{2.4c}$$

where, k and η represent the wave number and intrinsic wave impedance, respectively, in each half-space. The tangential components of the primary electric field intensity and the tangential and normal components of the primary magnetic field intensities are continuous at the surface. These boundary conditions are written as

(a) continuity of tangential E-fields: $E^p_{ya} = E^p_{yb}$ @ x=$D(z)$ (2.5a)

(b) continuity of tangential of H-fields: $H^p_{za} + D'H^p_{xa} = H^p_{zb} + D'H^p_{xb}$ @ x=$D(z)$ (2.5b)

(c) continuity of normal H-fields: $H^p_{xa} - D'H^p_{za} = H^p_{xb} - D'H^p_{zb}$ @ x=$D(z)$ (2.5c)

where $D' = dD(z)/dz$. Equations (2.5) reduce to

$$E^p_{ya} = E^p_{yb},\ H^p_{za} = H^p_{zb},\ H^p_{xa} = H^p_{xb} \ @\ x=D(z) \tag{2.6}$$

The primary electric field is postulated in the upper half-space (i.e., $x \geq D$) to be

$$E^p_{ya} = E^i_0(e^{-j\beta_0 z + ju_0 x} + \Gamma_{ab} e^{-j\beta_0 z - ju_0(x-2D)}) \tag{2.7a}$$

and in the lower half- space (i.e., in the region $x \leq D$) to be

$$E^p_{yb} = E^i_0 T_{ab} e^{-j\beta_0 z + jv_0 x + j(u_0 - v_0)D} \tag{2.8a}$$

Note that the incident field in (2.7a) satisfies the source-free Maxwell's equations, while both the reflected and the transmitted fields satisfy the Maxwell's equations with sources.

The remaining magnetic field components are found using Maxwell's equations (2.4a,b) with $M_x=M_z=0$. Hence, the primary magnetic fields in the upper half-space $(x \geq D)$ are

$$H_{za}^{p} = -\frac{u_0}{k_0\eta_0} E_0^i [e^{-j\beta_0 z + ju_0 x} - \Gamma_{ab} e^{-j\beta_0 z - ju_0(x-2D)}] \tag{2.7b}$$

$$H_{xa}^{p} = -\frac{1}{k_0\eta_0} E_0^i [\beta_0 e^{-j\beta_0 z + ju_0 x} + (\beta_0 - 2u_0 D')\Gamma_{ab} e^{-j\beta_0 z - ju_0(x-2D)}] \tag{2.7c}$$

and the primary magnetic fields in the lower half-space $(x \leq D)$ are

$$H_{zb}^{p} = -\frac{v_0}{k_0\eta_0} E_0^i T_{ab} e^{-j\beta_0 z + jv_0 x + j(u_0 - v_0)D} \tag{2.8b}$$

$$H_{xb}^{p} = -\frac{1}{k_0\eta_0} E_0^i T_{ab} [\beta_0 - (u_0 - v_0)D'] e^{-j\beta_0 z + jv_0 x + j(u_0 - v_0)D} \tag{2.8c}$$

where $D=D(z)$ and the Γ_{ab} and T_{ab} denote reflection and transmission coefficients expressed as

$$\Gamma_{ab} = \frac{u_0 - v_0}{u_0 + v_0} \tag{2.9a}$$

$$T_{ab} = \frac{2u_0}{u_0 + v_0} \tag{2.9b}$$

v_0 is the x-component of the wave vector in the dielectric, i.e., $v_0 = \sqrt{k_\varepsilon^2 - \beta_0^2}$, with $k_\varepsilon = \omega\sqrt{\mu_0\varepsilon_0\varepsilon_r} = \sqrt{\varepsilon_r}k_0$ and $\eta_0 = \sqrt{u_0/\varepsilon_0}$.

The actual field solution must satisfy the Maxwell's source free equations with both M_z and J_y equal to zero in (2.4) and the boundary conditions in (2.6). The primary field solutions (2.7) and (2.8) satisfy the boundary conditions, but do not satisfy (2.4c) with J_y=0. However, the primary field does satisfy Maxwell's equations (2.4) with a

single source term, namely, a fictitious electric current source J_y^p, called the primary volume current density. The primary volume current density in each space can be found by substituting (2.7,8) into (2.4c). They are

$$J_{ya}^p(x,z;u_0) = -jE_0^i \frac{2u_0}{k_0\eta_0}\left(\frac{u_0 - v_0}{u_0 + v_0}\right)[2\beta_0 D' - 2u_0 D'^2 + jD'']e^{-j\beta_0 z - ju_0(x-2D)}, \quad x > D \qquad (2.10a)$$

$$J_{yb}^p(x,z;v_0) = -jE_0^i \frac{2u_0}{k_0\eta_0}\left(\frac{u_0 - v_0}{u_0 + v_0}\right)[2\beta_0 D' - (u_0 - v_0)D'^2 + jD'']e^{-j\beta_0 z + jv_0 x + j(u_0 - v_0)D}, \quad x < D$$

(2.10b)

The primary current densities are zero beyond the rough surface region (i.e., in regions $|z| > L$) according to (2.10). The primary volume currents are not physically present and, therefore, are called fictitious current distributions. They are needed to support the primary field. To remove the primary volume current distributions, sheet current distributions are introduced. The sheets of current are assumed to be placed on planes located at $z=z_1$, which extend throughout the entire region where the primary volume currents are assumed to exist, i.e., throughout the region $-L \le z_1 \le +L$, and extend to ± infinity in the x and y directions; see Figure 2.3. Each sheet current is defined by a modal field specific to the geometry under investigation that satisfies the boundary conditions and Maxwell's equations. Hence, the modal wave set consists of incident, reflected and transmitted plane waves (to be clarified later) that propagate in particular directions to the right and to the left of the sheet current.

Consider the primary volume current density at a specific point $P(x, z_1)$ in the xz-plane. It can be cancelled by a superposition of "all" the first-order sheet currents that pass through this same point. The sheet currents themselves are expressed in terms of

groups of plane waves -called mode groups (to be clarified later). Sum of the mode groups forms a complete, orthogonal system. The superposition of these plane wave mode groups constitutes an integral representation over one spatial transform real variable u in the range $0 \le u < \infty$. Thus, the cancellation of the volume current by the superposition of the sheet currents is mathematically written as:

$$J_y^p(x, z_1; u_0) + \int_{u=0}^{\infty} J_{sy}^{(1)}(x, z = z_1, u) du = 0 \tag{2.11}$$

where the superscript (1) in $J_{sy}^{(1)}$ denotes a first-order sheet current density. A plane wave integral representation is valid for a linear, homogeneous, stationary (time independent) and unbounded medium [11]. In the problem studied here, the geometry consists of two half- spaces and therefore the integral representation involves groups of plane waves that satisfy the boundary conditions at the interface. The first-order current sheets are determined by appropriately constructed orthogonal and complete mode fields, which will be discussed in Section 2.2.1.

2.2 Sheet Current

The expansion of the primary volume current ($J_y^p(x,z)$) in terms of a superposition of sheet currents is constructed such that they form a complete system of orthogonal

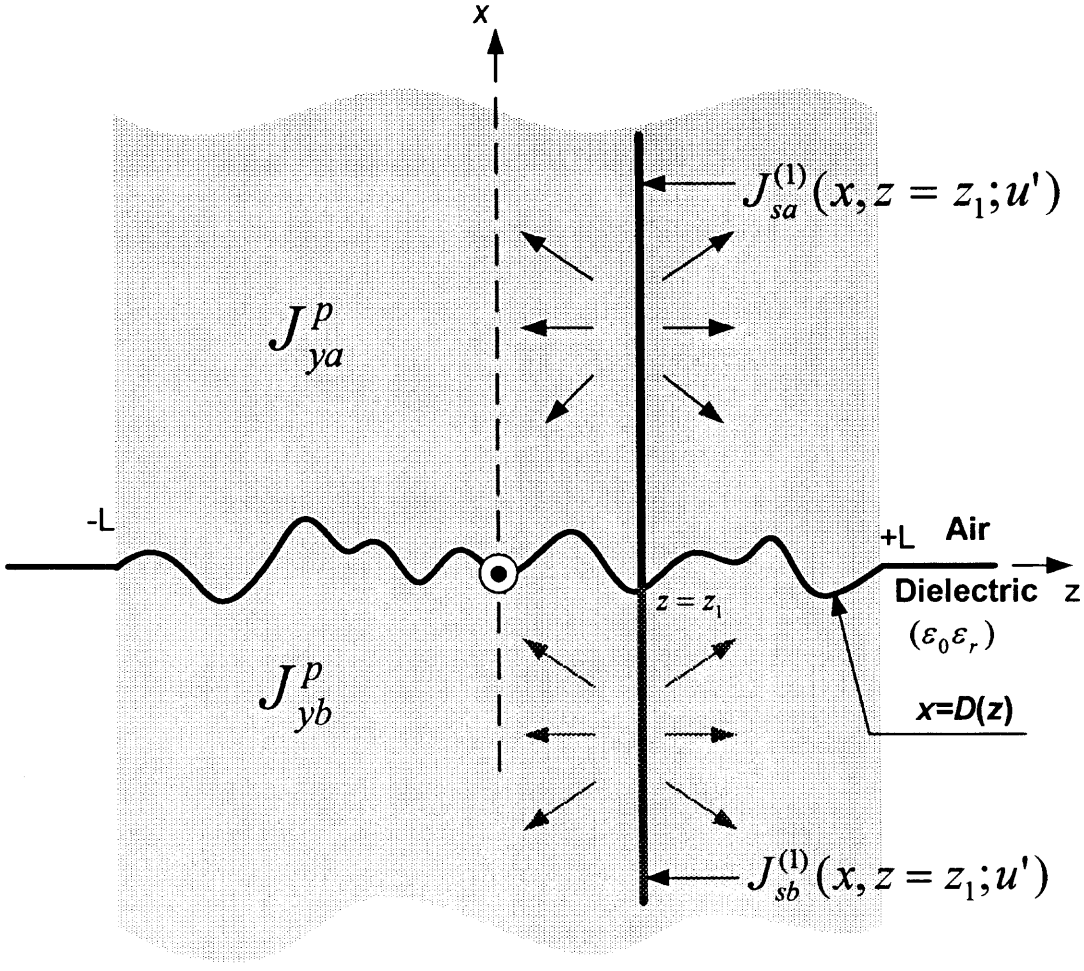

Figure 2.3 Primary volume current and first order sheet current densities

functions. To obtain such a representation, each sheet current distribution in the plane $z=z_1$ is assumed to produce a particular group of plane waves- called the group modal field. Such a mode wave field is constructed to satisfy the boundary conditions and to

satisfy Maxwell's equations, but with first-order volume current density $J_y^{(1)}$. At first, the structure of the mode fields is suggestive of the primary wave field, which consists of incident, reflected and transmitted plane waves. This structure is not satisfactory. Because of the geometry, two modal group fields are required and their structure is as follows. The group-1 mode field is chosen such that the only outgoing wave field of the group appears in the upper half-space. The group-2 mode field is chosen to have a single outgoing wave field in the lower half-space. These field structures are necessary to insure that the field decays in the far field.

2.2.1 Mode Structure

A schematic illustration of the group modal field structures that are used is depicted in Figure 2.4. For convenience, the plane waves constituting the mode groups in the regions $z<z_1$ are omitted. They can easily be visualized by constructing the mirror images about the symmetry plane $z= z_1$. The first mode group is seen to include one outgoing plane wave in the upper air region whereas the second mode group is shown to possess a single outgoing plane wave in the lower dielectric region.

For mode group-1, the outgoing plane wave in the upper air region is characterized by real values of u in the range $0 \le u < \infty$ with $\beta^2 = k_0^2 - u^2$ (see Figure 2.4) and mode amplitude $E_0^{g1}(u,z_1;u_o)$. The values v and β specify the direction of the associated constituent plane wave of group-1 in the lower region that travels toward the interface. The x-components of the wave vectors in the air and dielectric regions are related by

$$v^2 - u^2 = k_0^2(\varepsilon_r - 1) \tag{2.12}$$

Note that β is the same in the air and dielectric regions because of the continuity of the tangential electric fields at the interface at $x=D(z)$. $A_1E_0^{g1}$ and $B_1E_0^{g1}$ are the mode amplitudes of the wave constituents that travel toward the interface in the air region and in the dielectric region, respectively. As mentioned, mode group-1 satisfies Maxwell's equations (with fictitious electrical volume current density) and satisfies the boundary conditions. The second mode group (mode group-2) is similar to the first mode group,

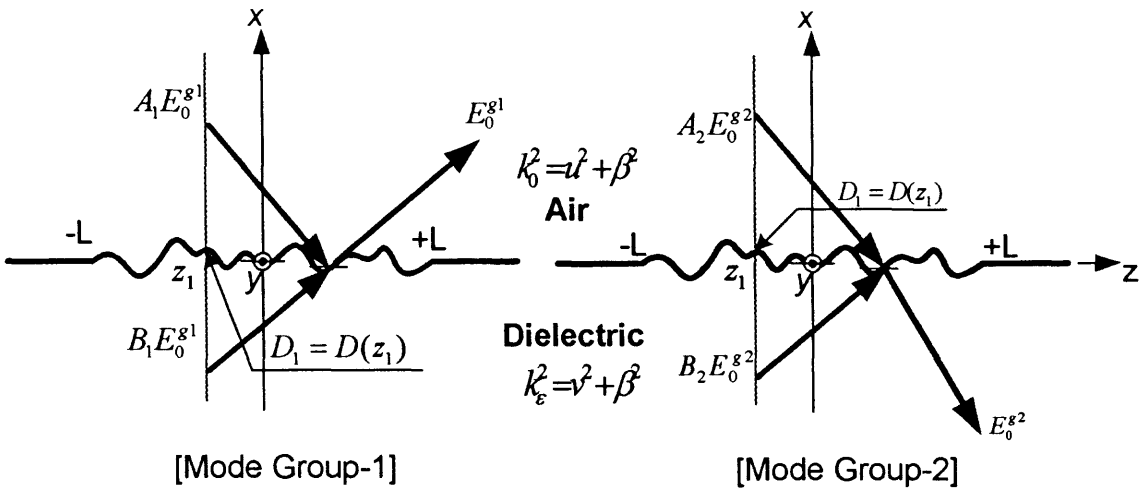

Figure 2.4 Mode structure.

but as noted has only one outgoing plane wave that exists in the dielectric. For plane waves belonging to the second mode group, v is real and ranges over $0 \le v < \infty$ with $\beta^2 = k_\varepsilon^2 - v^2$; since v is defined to be real, u for mode group-2 can be real and purely imaginary (see Figure 2.6). The relative amplitudes for the plane waves traveling toward the interface A_1 and B_1 (or A_2 and B_2 for mode group-2) are found by using the boundary conditions to be:

$$A_1 = \frac{u-v}{u+v} = \Gamma_{ab} \tag{2.13a}$$

$$B_1 = \frac{2u}{u+v} = T_{ab} \tag{2.13b}$$

$$A_2 = \frac{2v}{u+v} = T_{ba} \tag{2.13c}$$

$$B_2 = \frac{v-u}{u+v} = \Gamma_{ba} \tag{2.13d}$$

All field components in mode group-1 are obtained as

$$E_{ya}^{g1}(x,z) = E_0^{g1}[e^{-jux} + (\frac{u-v}{u+v})e^{ju(x-2D)}]e^{-j\beta|z-z_1|} \tag{2.14a}$$

$$H_{za}^{g1}(x,z) = \frac{E_0^{g1}}{\eta_0 k_0} u[e^{-jux} - (\frac{u-v}{u+v})e^{ju(x-2D)}]e^{-j\beta|z-z_1|} \tag{2.14b}$$

$$H_{xa}^{g1}(x,z) = -\frac{E_0^{g1}}{\eta_0 k_0}[\ddot{\beta}e^{-jux} + (\ddot{\beta} + 2uD')(\frac{u-v}{u+v})e^{ju(x-2D)}]e^{-j\beta|z-z_1|} \tag{2.14c}$$

$$E_{yb}^{g1}(x,z) = E_0^{g1}(\frac{2u}{u+v})[e^{-jvx-j(u-v)D}]e^{-j\beta|z-z_1|} \tag{2.14d}$$

$$H_{zb}^{g1}(x,z) = \frac{E_0^{g1}}{\eta_0 k_0}(\frac{2uv}{u+v})[e^{-jvx-j(u-v)D}]e^{-j\beta|z-z_1|} \tag{2.14e}$$

$$H_{xb}^{g1}(x,z) = -\frac{E_0^{g1}}{\eta_0 k_0}(\frac{2u}{u+v})[\{\ddot{\beta} + (u-v)D'\}e^{-jvx-j(u-v)D}]e^{-j\beta|z-z_1|} \tag{2.14f}$$

The field components in mode group-2 are

$$E_{ya}^{g2}(x,z) = E_0^{g2}(\frac{2v}{u+v})[e^{jux-j(u-v)D}]e^{-j\beta|z-z_1|} \tag{2.15a}$$

$$H_{za}^{g2}(x,z) = -\frac{E_0^{g2}}{\eta_0 k_0}\left(\frac{2uv}{u+v}\right)[e^{jux-j(u-v)D}]e^{-j\beta|z-z_1|} \tag{2.15b}$$

$$H_{xa}^{g2}(x,z) = -\frac{E_0^{g2}}{\eta_0 k_0}\left(\frac{2v}{u+v}\right)[\{\ddot{\beta}+(u-v)D'\}e^{jux-j(u-v)D}]e^{-j\beta|z-z_1|} \tag{2.15c}$$

$$E_{yb}^{g2}(x,z) = E_0^{g2}[e^{jvx} + \left(\frac{v-u}{u+v}\right)e^{-jv(x-2D)}]e^{-j\beta|z-z_1|} \tag{2.15d}$$

$$H_{zb}^{g2}(x,z) = -\frac{E_0^{g2}}{\eta_0 k_0}v[e^{jvx} - \left(\frac{v-u}{u+v}\right)e^{-jv(x-2D)}]e^{-j\beta|z-z_1|} \tag{2.15e}$$

$$H_{xb}^{g2}(x,z) = -\frac{E_0^{g2}}{\eta_0 k_0}[\ddot{\beta}e^{jvx} + (\ddot{\beta}-2vD')\left(\frac{v-u}{u+v}\right)e^{-jv(x-2D)}]e^{-j\beta|z-z_1|} \tag{2.15f}$$

where $\ddot{\beta} = \mathrm{sgn}(z-z_1)\beta$.

Similar to the primary fields, the first-order (mode) fields given by (2.14)-(2.15) require the introduction of a fictitious electrical volume current distribution to be a solution to Maxwell's equations. The first-order volume current densities for mode group-1 and group-2 are calculated by substituting (2.14) and (2.15) into (2.4c). Thus,

$$J_{ya}^{g1}(x,z) = j\frac{E_0^{g1}}{\eta_0 k_0}\left(2u\frac{u-v}{u+v}\right)[2\ddot{\beta}D' + 2uD'^2 + jD'']e^{ju(x-2D)-j\beta|z-z_1|} \tag{2.16a}$$

$$J_{yb}^{g1}(x,z) = j\frac{E_0^{g1}}{\eta_0 k_0}\left(2u\frac{u-v}{u+v}\right)[2\ddot{\beta}D' + (u-v)D'^2 + jD'']e^{-jvx-j(u-v)D-j\beta|z-z_1|} \tag{2.16b}$$

$$J_{ya}^{g2}(x,z) = j\frac{E_0^{g2}}{\eta_0 k_0}\left(2v\frac{u-v}{u+v}\right)[2\ddot{\beta}D' + (u-v)D'^2 + jD'']e^{jux-j(u-v)D-j\beta|z-z_1|} \tag{2.16c}$$

$$J_{yb}^{g2}(x,z) = j\frac{E_0^{g2}}{\eta_0 k_0}\left(2v\frac{u-v}{u+v}\right)[2\ddot{\beta}D' - 2vD'^2 + jD'']e^{-jv(x-2D)-j\beta|z-z_1|} \tag{2.16d}$$

The first-order fictitious volume current densities are eliminated by introducing a superposition of the second-order sheet currents. By continuing this procedure, higher-order field solutions are obtained.

The first-order mode fields are produced by sheet currents with unspecified modal field amplitudes E_0^{g1} and E_0^{g2}. These model amplitudes are determined by imposing the condition that a superposition of the first-order sheet currents eliminate the primary volume currents. For convenience, each sheet current density at $z=z_1$ is re-expressed in terms of orthogonal functions.

2.2.2 Modal Amplitude

The boundary condition - continuity of the tangential electric fields at the $z=z_1$ - shows that the electric field to the right equals the electric field to the left of the sheet currents located in a plane at $z=z_1$. This result is used in expressions (2.14)-(2.15) to show that $E_0^{g1} = E_{0>}^{g1} = E_{0<}^{g1}$, $E_0^{g2} = E_{0>}^{g2} = E_{0<}^{g2}$ at $z=z_1$. The normal components of the magnetic fields, H_z^{g1} and H_z^{g2}, are also continuous; this is seen by substituting $z=z_1$ into (2.14b,e) and (2.15b,e). The last boundary condition, which is the discontinuity in the tangential x-components of the magnetic fields at $z=z_1$, is used to determine the first- order sheet current density J_{sy} since

$$\underline{J}_s = \hat{z} \times [\underline{H}_> - \underline{H}_<]_{z=z_1} \tag{2.17a}$$

This boundary condition is rewritten as

$$\underline{J}_s = \hat{y} J_{sy} = \hat{y}[H_{x>} - H_{x<}]_{z=z_1} \tag{2.17b}$$

which results in

$$J_{sy}^{g1} = F_1(u)\psi_{TE}^{g1}(x, z_1; u) \tag{2.18a}$$

$$J_{sy}^{g2} = F_2(v)\psi_{TE}^{g2}(x, z_1; v) \tag{2.18b}$$

where,

$$F_1(u) = E_0^{g1}\frac{2\beta(u)}{\eta_0 k_0} \tag{2.19a}$$

$$F_2(v) = E_0^{g2}\frac{2\beta(v)}{\eta_0 k_0} \tag{2.19b}$$

and the mode functions for each groups, ψ^{g1} and ψ^{g2}, are

$$\psi_{TE}^{g1}(x, z_1; u) = \begin{Bmatrix} e^{-jux} + \dfrac{u-v}{u+v}e^{ju(x-2D_1)}, & x \geq D_1 \\ \dfrac{2u}{u+v}e^{-jvx-j(u-v)D_1}, & x \leq D_1 \end{Bmatrix} \tag{2.20a}$$

$$\psi_{TE}^{g2}(x, z_1; v) = \begin{Bmatrix} \dfrac{2v}{u+v}e^{jux-j(u-v)D_1}, & x \geq D_1 \\ e^{jvx} + \dfrac{v-u}{v+u}e^{-jv(x-2D_1)}, & x \leq D_1 \end{Bmatrix} \tag{2.20b}$$

Note that the modal amplitudes E_0^{g1} and E_0^{g2} are defined for each value of u or v, respectively, for the same z-component of the wave vectors β and for each value of z_1, with $D_1 = D(z_1)$. The first-order mode fields (2.14) to (2.15) are completely determined by finding the modal amplitudes via (2.11). This is accomplished by expressing the sheet currents in terms of the orthogonal functions given in (2.20). The orthogonal relations for the mode functions ψ_{TE}^{g1} and ψ_{TE}^{g2} can be shown to be (see Appendix A)

$$\int_{x=-\infty}^{+\infty} \psi_{TE}^{g1}(x, z_1; u')\psi_{TE}^{*g1}(x, z_1; u)dx = 2\pi\delta(u - u') \tag{2.21a}$$

$$\int_{x=-\infty}^{+\infty} \psi_{TE}^{g2}(x,z_1;v')\psi_{TE}^{*g2}(x,z_1;v)dx = 2\pi\delta(v-v') \tag{2.21b}$$

$$\int_{x=-\infty}^{+\infty} \psi_{TE}^{g1}(x,z_1;u')\psi_{TE}^{*g2}(x,z_1;v)dx = 0 \tag{2.21c}$$

$$\int_{x=-\infty}^{+\infty} \psi_{TE}^{g2}(x,z_1;v')\psi_{TE}^{*g1}(x,z_1;u)dx = 0 \tag{2.21d}$$

where * denotes complex conjugation.

To find $E_0^{g1}(x,u;u_0)$, substitute (2.10) and (2.18) into (2.11), multiply by $\psi^{*g1}(x,z_1;u)$, and integrate with respect to x from -∞ to +∞ to obtain

$$\int_{-\infty}^{+\infty} J_y^p \psi_{TE}^{*g1} dx + \int_{-\infty}^{+\infty}\int_{0}^{+\infty} F_1(u')\psi_{TE}^{g1}\psi_{TE}^{*g1} du'dx + \int_{-\infty}^{+\infty}\int_{0}^{+\infty} F_2(v')\psi_{TE}^{g2}\psi_{TE}^{*g1} dv'dx = 0 \tag{2.22}$$

Use of the orthogonality relations in (2.21) reduces (2.22) to

$$\int_{-\infty}^{+\infty} J_y^p \psi_{TE}^{*g1} dx = -2\pi F_1(u) \tag{2.23a}$$

By replacing $\psi_{TE}^{*g1}(x,z_1;u)$ with $\psi_{TE}^{*g2}(x,z_1;v)$, (2.22) yields

$$\int_{-\infty}^{+\infty} J_y^p \psi_{TE}^{*g2} dx = -2\pi F_2(v) \tag{2.23b}$$

where $F_1(u)$ and $F_2(v)$ are given in (2.19). Note that the orthogonality relations given in (2.21) are written formally as shown, but more precisely can be written as $\int_{-\infty}^{+\infty}\int_{0}^{+\infty} F_1(u')\psi_{TE}^{g1}\psi_{TE}^{*g1} du'dx = 2\pi F_1(u)$, which can be verified rigorously. By solving (2.22), the first-order modal amplitudes for mode group-1 and mode group-2 are determined to be

$$E_0^{g1}(z_1,u;u_0) = -jE_0^i \frac{u_0}{2\pi\beta}\left(\frac{u_0 - v_0}{u_0 + v_0}\right) e^{-j\beta_0 z_1 + j(u_0 - u)D_1}$$

$$\times\left[W_1(D_1)\left(\frac{v^* + u_0}{v^* + u}\right)\varsigma_1(u,u_0) + W_2(D_1)\left(\frac{-j2u}{(u+v^*)(v_0+v^*)}\right)\right] \quad (2.24a)$$

$$E_0^{g2}(z_1,v;u_0) = -jE_0^i \frac{u_0}{2\pi\beta}\left(\frac{u_0 - v_0}{u_0 + v_0}\right) e^{-j\beta_0 z_1 + j(u_0 - v)D_1}$$

$$\times\left[W_1(D_1)\left(\frac{-j2v}{(u^*+v)(u_0+u^*)}\right) + W_2(D_1)\left(\frac{u^* + v_0}{v + u^*}\right)\varsigma_2(v,v_0)\right] \quad (2.24b)$$

where

$$W_1(D_1) = 2\beta_0 D_1' - 2u_0 D_1'^2 + jD_1'' \quad (2.25a)$$

$$W_2(D_1) = 2\beta_0 D_1' - (u_0 - v_0)D_1'^2 + jD_1'' \quad (2.25b)$$

and

$$\varsigma_1(u,u_0) = \pi\delta(u - u_0) + jP\left(\frac{2u}{u^2 - u_0^2}\right) \quad (2.26a)$$

$$\varsigma_2(v,v_0) = \pi\delta(v - v_0) + jP\left(\frac{2v}{v^2 - v_0^2}\right) \quad (2.26b)$$

Note that $P(1/u)$ is called the principal value of u; when $u \neq 0$ it behaves like $1/u$, but for $u=0$, it vanishes.

The first-order electric field is obtained by superimposing the modes of both groups given by (2.14a) and (2.15a) with modal amplitudes E_0^{g1}, E_0^{g2} specified in (2.24). The superposition is a double integral which extends first over all values of the x-

component of the wave vector for each group, i.e., $u \in [0, \infty)$ for mode group-1 and $v \in [0, \infty)$ for mode group-2, and then over the physical space $z_1 \in [-L, L]$.

2.3 First-order Scattered Far Field

The expression for the first-order field solution depends on the location of the observation point relative to the spatial location of the sheet currents. There are three different expressions for the first-order field solution; each pertains to one of the regions $z>L$, $z<-L$ and $-L<z<L$ (since the phase term differs in each region). The far field is found from the expression pertinent to the region $|z|> L$.

2.3.1 Upper Half-Space

The first-order field in the upper half-space ($x>D(z)=0$ for $|z|>L$) is expressed as a superposition of the orthogonal mode fields belonging to mode group-1 and mode group-2 as follows:

$$E_{ya}^{(1)}(x,z) = \int_{-L}^{L}\int_{0}^{\infty} E_{ya}^{g1}(x,z;z_1,u)\,du\,dz_1 + \int_{-L}^{L}\int_{0}^{\infty} E_{ya}^{g2}(x,z;z_1,v)\,dv\,dz_1 \tag{2.27}$$

where E_{ya}^{g1} and E_{ya}^{g2} are specified in (2.14a) and (2.15a), respectively, i.e.,

$$E_{ya}^{g1}(x,z;z_1,u) = E_0^{g1}(z_1,u)\psi_{TE}^{g1}(x,z_1;u)e^{-j\beta|z-z_1|}$$

$$E_{ya}^{g2}(x,z;z_1,v) = E_0^{g2}(z_1,v)\psi_{TE}^{g2}(x,z_1;v)e^{-j\beta|z-z_1|}$$

and the dependence on u_o in E_0^{g1} and E_0^{g2} is suppressed.

Evaluations of the integrations over u and v in (2.27) give an expression for the field that displays a dependence on the surface height $D(z)$ and on the square of the

surface slope $D'(z)^2$, but not on the second derivative $D''(z)$. Because the mode field amplitudes E_0^{g1} and E_0^{g2} have singularities at $u=u_o$ and $v=v_o$ expressed by ς_1 and ς_2 in (2.26), respectively, these evaluations are done by first deforming the paths of integration off the real u or real v axes to avoid the singularities (see Figure 2.5), followed by the imposition of Cauchy's theorem. It can be shown that

$$\int_0^\infty f(u)\varsigma_1(u)du = \int_\Omega f(u)j\left(\frac{2u}{u^2-u_0^2}\right)du \tag{2.28}$$

where $\varsigma_1(u)$ is given in (2.26a), with a similar expression for $\varsigma_2(v)$. Figure (2.5) shows

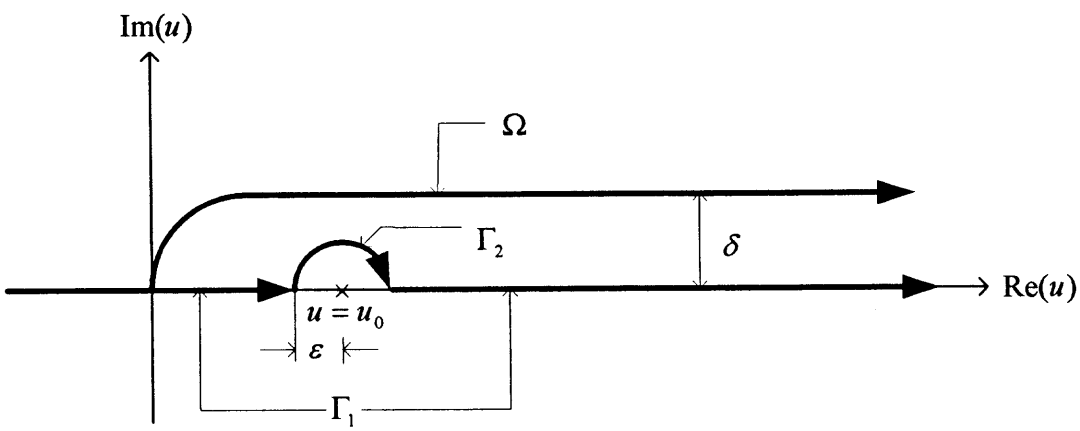

Figure 2.5 The integration path in the complex u plane.

that no singularities are encountered in the deformation of the path off the real axis. Thus, the integral over the deformed path Ω is equivalent to the integral over the original path along the real u-axis or real v-axis. Note that the path segments Γ_1 along the real u-axes involves only the principal part of $\varsigma_1(u)$ in the integrand since the singularity at $u=u_o$ is not included; ε is a small, positive number. Similar discussion applies to integration path in the v-plane. The order of integrations in the double integrals in (2.27) can be

interchanged provided the integration over u and v take place along such deformed paths. Setting $D(z)$=0 and substituting (2.14a), (2.15a) into $E_{ya}^{g1}(x,z;z_1,u)$, $E_{ya}^{g2}(x,z;z_1,v)$ gives for (2.27) the following expression for the first-order field in the regions $|z|>L$:

$$E_{ya}^{(1)}(x,z)=\int_{\Omega}\int_{-L}^{L}E_0^{g1}(z_1,u)\left[e^{-jux}+(\frac{u-v}{u+v})e^{jux}\right]e^{-j\beta|z-z_1|}dz_1du$$

$$+\int_{\Omega}\int_{-L}^{L}E_0^{g2}(z_1,v)(\frac{2v}{u+v})e^{jux}e^{-j\beta|z-z_1|}dz_1dv \qquad (2.29)$$

Substituting (2.24) into modal amplitudes (E_0^{g1},E_0^{g2}) in (2.29) and integrating by parts over z_1 yields the following integral evaluations:

$$\int_{-L}^{L}W_1(D_1)e^{j(u_0+u)D_1-j\beta|z-z_1|-j\beta_0z_1}dz_1$$

$$=(u_0-u)\int_{-L}^{L}\left[1-e^{j(u_0+u)D_1}\right]e^{-j\beta|z-z_1|-j\beta_0z_1}dz_1-(u_0-u)\int_{-L}^{L}D_1'^2e^{j(u_0+u)D_1}e^{-j\beta|z-z_1|-j\beta_0z_1}dz_1 \quad (2.30a)$$

$$\int_{-L}^{L}W_2(D_1)e^{j(u_0+u)D_1-j\beta|z-z_1|-j\beta_0z_1}dz_1$$

$$=(u_0-u)\int_{-L}^{L}\left[1-e^{j(u_0+u)D_1}\right]e^{-j\beta|z-z_1|-j\beta_0z_1}dz_1+(v_0+v)\int_{-L}^{L}D_1'^2e^{j(u_0+u)D_1}e^{-j\beta|z-z_1|-j\beta_0z_1}dz_1 \quad (2.30b)$$

$$\int_{-L}^{L}W_1(D_1)e^{j(u_0-v)D_1-j\beta|z-z_1|-j\beta_0z_1}dz_1$$

$$=\frac{v_0^2-v^2}{(u_0-v)}\int_{-L}^{L}\left[1-e^{j(u_0-v)D_1}\right]e^{-j\beta|z-z_1|-j\beta_0z_1}dz_1-(u_0+v)\int_{-L}^{L}D_1'^2e^{j(u_0-v)D_1}e^{-j\beta|z-z_1|-j\beta_0z_1}dz_1 \quad (2.30c)$$

$$\int_{-L}^{L} W_2(D_1) e^{j(u_0-v)D_1 - j\beta|z-z_1| - j\beta_0 z_1} dz_1$$

$$= \frac{v_0^2 - v^2}{(u_0 - v)} \int_{-L}^{L} \left[1 - e^{j(u_0-v)D_1}\right] e^{-j\beta|z-z_1| - j\beta_0 z_1} dz_1 - (v_0 - v) \int_{-L}^{L} D_1'^2 e^{j(u_0-v)D_1} e^{-j\beta|z-z_1| - j\beta_0 z_1} dz_1 \quad (2.30d)$$

where $W_1(D_1)$ and $W_2(D_1)$ are given in (2.25). Note that it was assumed that $D(\pm L)=D'(\pm L)=0$.

The far field is accounted for by retaining only the propagating modes since the evanescent modes do not contribute to the far field. The integration ranges for u and v in (2.27) or (2.29) are, therefore, chosen such that both u and β are real and positive in the air region. For the modes of group-1, β is real, when u lies in the range $0 \le u \le k_0$. For the modes of group-2, using the relations

$$\beta = \sqrt{\varepsilon_r k_0^2 - v^2} \quad (2.31a)$$

$$u = \sqrt{v^2 - k_0^2(\varepsilon_r - 1)} \quad (2.31b)$$

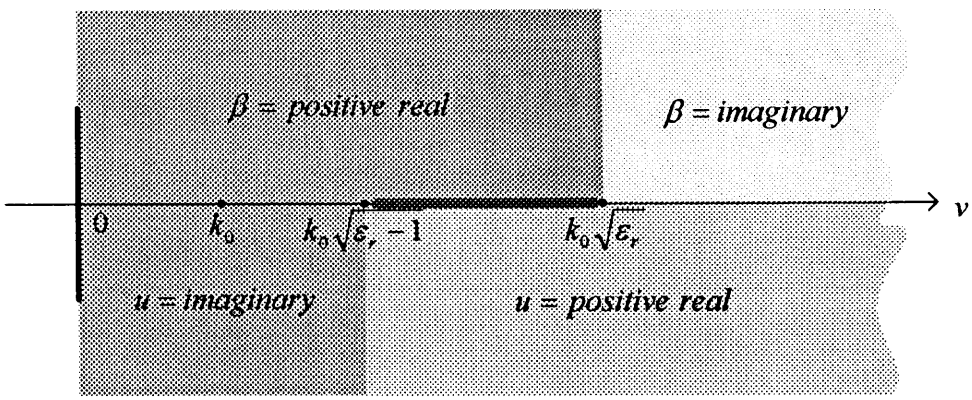

Figure 2.6 Dependency of u and β on v for mode group-2 in the upper-half space.

it is clear that for both u and β to be positive real numbers, the v-integration range in (2.29) must lie in the range $k_0\sqrt{\varepsilon_r - 1} \le v \le k_0\sqrt{\varepsilon_r}$; refer to Figure 2.6.

Equation (2.29) is rewritten using (2.30) and setting $v=v^*$ to give

$$E_{ya}^{(1)}(x,z) = \left[\frac{E_0^i}{\pi}\frac{u_0}{u_0+v_0}k_0^2(\varepsilon_r - 1)\right]$$

$$\times\left[\int_0^{k_0}\int_{-L}^{L}\frac{u}{(v+u)(u+u_0)}\left\{[1-e^{j(u_0+u)D_1}]-[1-\frac{u+u_0}{v+v_0}]D_1'^2 e^{j(u_0+u)D_1}\right\}e^{-jux-j\beta|z-z_1|-j\beta_0 z_1}dz_1\frac{du}{\beta}\right.$$

$$-\int_0^{k_0}\int_{-L}^{L}\frac{u(v-u)}{(v+u)^2(u+u_0)}\left\{[1-e^{j(u_0+u)D_1}]-[1-\frac{u+u_0}{v+v_0}]D_1'^2 e^{j(u_0+u)D_1}\right\}e^{+jux-j\beta|z-z_1|-j\beta_0 z_1}dz_1\frac{du}{\beta}$$

$$\left.-\int_{k_0\sqrt{\varepsilon_r-1}}^{k_0\sqrt{\varepsilon_r}}\int_{-L}^{L}\frac{2v^2}{(v+u)^2}\left\{[\frac{1-e^{j(u_0-v)D_1}}{u_0-v}]-[\frac{1}{u_0+u}-\frac{1}{v+v_0}]D_1'^2 e^{j(u_0-v)D_1}\right\}e^{+jux-j\beta|z-z_1|-j\beta_0 z_1}dz_1\frac{dv}{\beta}\right]$$

(2.32)

The above equation does not posses a singularity at $u=u_0$ or $v=v_0$ since the potentially singular portions of the principle value in (2.26) are cancelled by the multiplicative terms $(u-u_0)$ or $(v-v_0)$ in (2.30). Note that the term $1/(u_0 - v)$ in the last integral is not a singularity at $v=u_0$ because of the result

$$\lim_{v\to u_0}\left[\frac{1-e^{j(u_0-v)D_1}}{u_0-v}\right] = \left.\frac{\frac{d}{dv}[1-e^{j(u_0-v)D_1}]}{\frac{d}{dv}[u_0-v]}\right|_{v=u_0} = -jD_1 \qquad (2.33)$$

Thus the integration over Ω is now performed along the real u-axes.

To obtain the far field, (2.32) is evaluated using the stationary phase approximation [11]. The first step is to introduce the following change in variables; see Figure 2.7.

$$u_0 = k_0 \cos\phi_0 \ , \ v_0 = k_0\sqrt{\varepsilon_r - \sin^2\phi_0} \ , \ \beta_0 = k_0 \sin\phi_0$$

$$u = k_0 \cos w \ , \ v = k_0\sqrt{\varepsilon_r - \sin^2 w} \ , \ \beta = k_0 \sin w \tag{2.34}$$

$$x = \rho\cos\phi \ , \ z = \rho\sin\phi \, .$$

The field in (2.32) at an observation point $P(x,z)$ is composed of three wave constituents, two incoming (toward the interface) and one outgoing (away from the

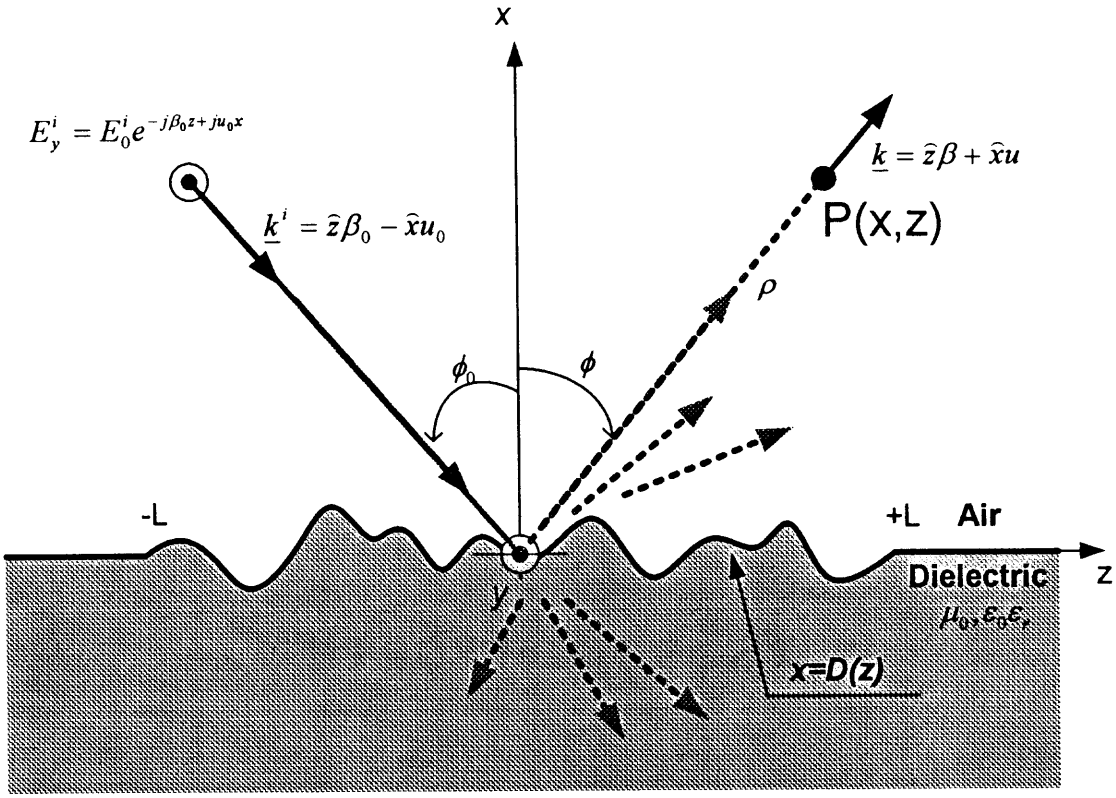

Figure 2.7 Scattering geometry and coordinate variables for the scattered first-order far field in the upper half-space.

interface). Evaluation of the resulting integral over w using the stationary phase approximation is applied only to the outgoing mode spectrum (the first integral in (2.32)) to obtain the far field:

$$E_{ya}^{(1)ff}(\phi,\phi_0)=\left[E_0^i\sqrt{\frac{2\pi}{k_0\rho}}\,e^{-jk_0\rho+j\frac{\pi}{4}}\right]R_{11}(\phi,\phi_0) \tag{2.35}$$

where the scatter pattern (R_{11}) in the upper half-space due to an incident plane wave in the upper half- space is given by

$$R_{11}(\phi,\phi_0)=\left[\frac{k_0^2}{\pi}(\varepsilon_r-1)\right]\left[\frac{u_0u}{(u_0+v_0)(u_0+u)(u+v)}\right]$$

$$\times\int_{-L}^{L}\left\{[1-e^{j(u_0+u)D_1}]-[1-\frac{u_0+u}{v_0+v}]D_1'^2e^{j(u_0+u)D_1}\right\}e^{-j(\beta_0-\beta)z_1}dz_1 \tag{2.36}$$

where

$$u_0=k_0\cos\phi_0\ ,\ v_0=k_0\sqrt{\varepsilon_r-\sin^2\phi_0}\ ,\ \beta_0=k_0\sin\phi_0$$

$$u=k_0\cos\phi\ ,\ v=k_0\sqrt{\varepsilon_r-\sin^2\phi}\ ,\ \beta=k_0\sin\phi$$

$$D_1=D(z_1),\quad D_1'=\left.\frac{dD(z)}{dz}\right|_{z=z_1}$$

which is valid for $-\pi/2\le\phi\le\pi/2$, $-\pi/2\le\phi_0\le\pi/2$.

2.3.2 Lower Half-Space

The first-order field in the lower half-space (in the dielectric) is determined by a superposition of orthogonal mode fields employing the same mode groups that were used to find the field in the upper half-space. Thus,

$$E_{yb}^{(1)}(x,z)=\int_{-L}^{L}\int_{0}^{\infty}E_{yb}^{g1}(x,z;z_1;u)dudz_1+\int_{-L}^{L}\int_{0}^{\infty}E_{yb}^{g2}(x,z;z_1;v)dvdz_1 \tag{2.37}$$

The deformed path Ω in Figure (2.5) is used again to avoid the singularity in E_{yb}^{g1} at $u=u_0$, and in E_{yb}^{g2} at $v=v_0$; hence, the order of the double integrations in (2.37) can then be interchanged. Substituting (2.14d) and (2.15d) into (2.37) gives:

$$E_{yb}^{(1)}(x,z) = \int_{\Omega}\int_{-L}^{L} E_0^{g1}(z_1,u)\left(\frac{2u}{u+v}\right)e^{-jvx}e^{-j\beta|z-z_1|}dz_1du$$

$$+\int_{\Omega}\int_{-L}^{L} E_0^{g2}(z_1,v)\left[e^{jvx}+\left(\frac{v-u}{u+v}\right)e^{-jvx}\right]e^{-j\beta|z-z_1|}dz_1dv \quad (2.38)$$

In (2.38), $D(z)=0$ since it is assumed that $z>|L|$.

To obtain the far field in the lower half-space, only propagating modes need be considered. In the first integral in (2.38) this means that both β and v are positive real. Hence, the range of integration over u in the first integral in (2.38) is $0 \le u \le k_0$; see Figure 2.8. For the second integral expression in (2.38), propagating modes are those plane waves that possess β real (v is already real for mode group-2); hence, the range of integration over v is in the range $0 \le v \le k_\varepsilon$. Note that u does not have to be real even though v is real so that u^* cannot be changed to u for group-2 modes.

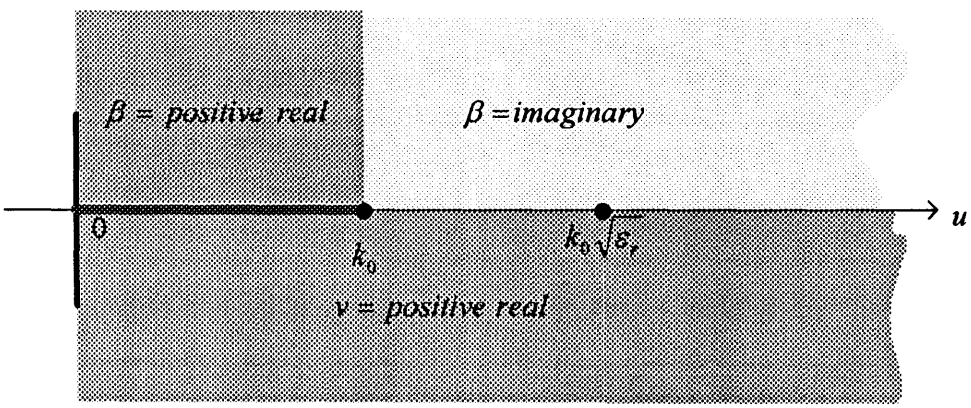

Figure 2.8 Dependency of v and β on u for mode group-1 in the lower half-space.

Substituting (2.24) for modal amplitudes and using (2.30) for integral evaluation over z_1, the first-order electric field in the lower half-space can be shown to reduce to

$$E_{yb}^{(1)}(x,z)=\left[\frac{E_0^i}{\pi}\frac{u_0}{u_0+v_0}k_0^2(\varepsilon_r-1)\right]$$

$$\times\left[\int_0^{k_0}\int_{-L}^{L}\frac{u}{(v+u)(u+u_0)}\left\{[1-e^{j(u_0+u)D_1}]-[1-\frac{u+u_0}{v+v_0}]D_1'^2e^{j(u_0+u)D_1}\right\}e^{-jvx-j\beta|z-z_1|-j\beta_0 z_1}dz_1\frac{du}{\beta}\right.$$

$$+\int_0^{k_0\sqrt{\varepsilon_r}}\int_{-L}^{L}\frac{v}{(v+u^*)}\left\{[\frac{1-e^{j(u_0-v)D_1}}{u_0-v}]-[\frac{1}{u_0+u^*}-\frac{1}{v+v_0}]D_1'^2e^{j(u_0-v)D_1}\right\}e^{+jvx-j\beta|z-z_1|-j\beta_0 z_1}dz_1\frac{dv}{\beta}$$

$$\left.+\int_0^{k_0\sqrt{\varepsilon_r}}\int_{-L}^{L}\frac{v-u}{(v+u)}\left\{[\frac{1-e^{j(u_0-v)D_1}}{u_0-v}]-[\frac{1}{u_0+u^*}-\frac{1}{v+v_0}]D_1'^2e^{j(u_0-v)D_1}\right\}e^{-jvx-j\beta|z-z_1|-j\beta_0 z_1}dz_1\frac{dv}{\beta}\right]$$

(2.39)

For the scattering geometry depicted in Figure 2.9 (compare to the previous scatter geometry in Figure 2.7), the following change of variables are introduced

$$u_0=k_0\cos\phi_0\ ,\ v_0=k_0\sqrt{\varepsilon_r-\sin^2\phi_0}\ ,\ \beta_0=k_0\sin\phi_0$$

$$u=k_0\sqrt{1-\varepsilon_r\sin^2 w}\ ,\ v=\sqrt{\varepsilon_r}k_0\cos w\ ,\ \beta=\sqrt{\varepsilon_r}k_0\sin w \qquad (2.40)$$

$$x=\rho\cos\bar{\phi}\ ,\ z=\rho\sin\bar{\phi}$$

The far field is obtained by using the stationary phase approximation. This is applied only to the second integral in (2.39) since that integral alone involves the out-going modes in lower half-space:

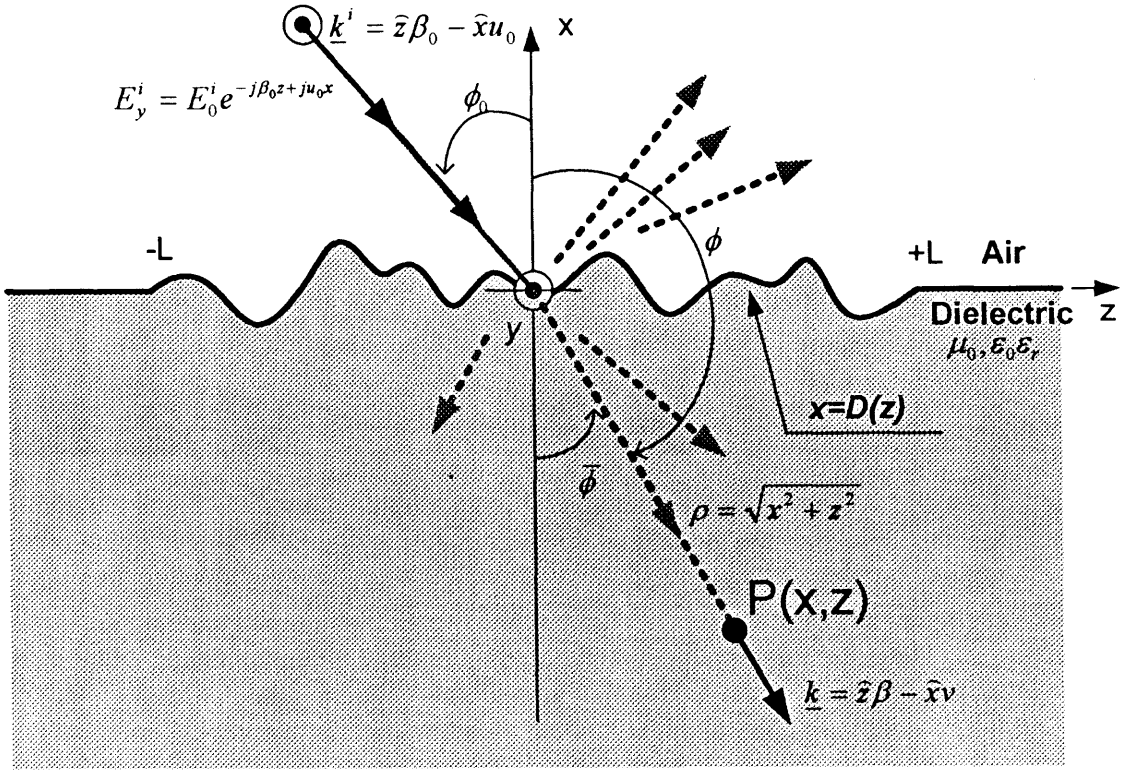

Figure 2.9 Scattering geometry and coordinate variables for the scattered first-order far field in the lower half-space.

$$E_{yb}^{(1)ff}(\bar{\phi},\phi_0) = \left[E_0^i \sqrt{\frac{2\pi}{k_\varepsilon \rho}}\, e^{-jk_\varepsilon \rho + j\frac{\pi}{4}} \right] R_{12}(\bar{\phi},\phi_0) \tag{2.41}$$

Hence, the scattering pattern R_{12} in the lower half-space due to an incident angle in the upper half-space is given by

$$R_{12}(\bar{\phi},\phi_0) = \left[\frac{k_0^2}{\pi}(\varepsilon_r - 1) \right] \left[\frac{u_0 v}{(u_0 + v_0)(u^* + v)} \right]$$

$$\times \int_{-L}^{L} \left\{ \left[\frac{1 - e^{j(u_0 - v)D_1}}{u_0 - v} \right] - \left[\frac{1}{u_0 + u^*} - \frac{1}{v + v_0} \right] D_1'^2 e^{j(u_0 - v)D_1} \right\} e^{-j(\beta_0 - \beta)z_1} dz_1 \tag{2.42}$$

where

$$u_0 = k_0 \cos\phi_0 \quad , \quad v_0 = k_0 \sqrt{\varepsilon_r - \sin^2 \phi_0} \quad , \quad \beta_0 = k_0 \sin \phi_0$$

$$u^* = k_0 \sqrt{\varepsilon_r \sin^2 \bar{\phi} - 1} \quad , \quad v = \sqrt{\varepsilon_r} k_0 \cos\bar{\phi} \quad , \quad \beta = \sqrt{\varepsilon_r} k_0 \sin \bar{\phi}$$

and remains valid for $-\pi/2 \le \bar{\phi} \le \pi/2$, $-\pi/2 \le \phi_0 \le \pi/2$.

CHAPTER 3

THE TM CASE

For the TM polarization case, only a y-directed magnetic field exists in addition to x and z components of the electric field, as shown in Figure 3.1. The procedure to get the TM solution follows closely the TE case, but is more complicated and requires additional

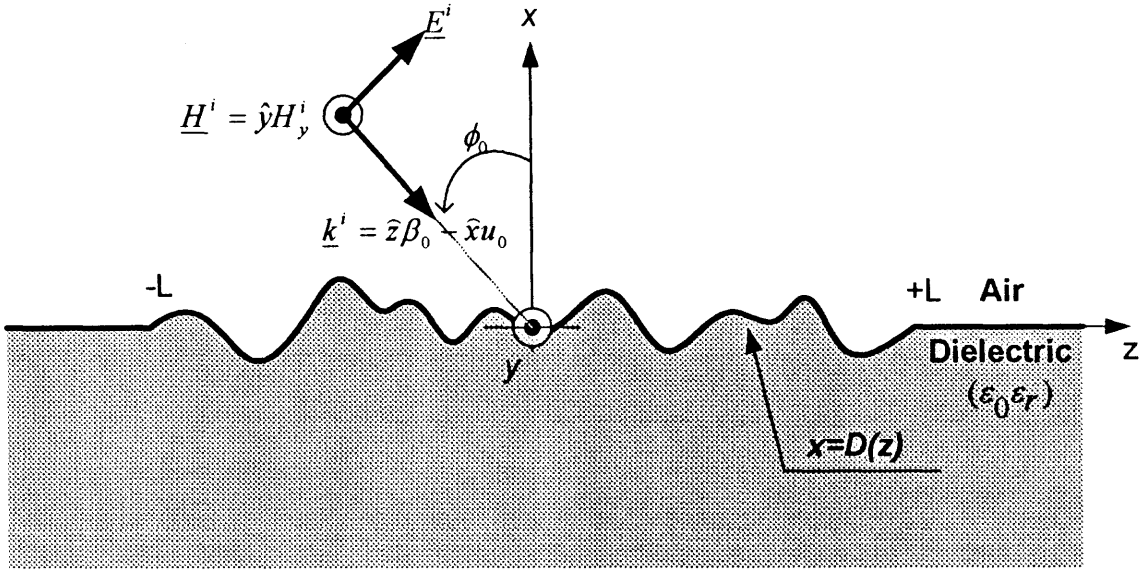

Figure 3.1 Geometry for TM case.

considerations. While the TE- primary field for rough surface scattering was readily constructed to satisfy surface boundary conditions by reference to the associated scatter problem for a flat interface, the TM- primary field that satisfies surface boundary conditions requires the introduction of a fictitious surface magnetic current distribution. This introduces mores complexity to the TM case. In other words, in constructing a primary field solution in the TM case that satisfies all boundary conditions and in addition is a solution of Maxwell's equations, not only is it necessary to introduce a

fictitious volume current density (which is now magnetic) but it is also necessary to introduce a fictitious surface current (also magnetic) along the interface between air and the dielectric. As was done in the TE case, a superposition of fictitious sheet currents is introduced to eliminate the above-mentioned fictitious volume and surface magnetic currents. Again, the sheet current density is obtained by appropriately constructing modal fields.

3.1 Primary Field

For the rough surface, the primary wave field is assumed to be expressed as

$$H_{ya}^{p} = H_{y}^{i} + H_{y}^{r} \quad , \quad x > D(z) \tag{3.1a}$$

$$H_{yb}^{p} = H_{y}^{t} \quad , \quad x < D(z) \tag{3.1b}$$

such that the incident wave in air is unaltered and assumed to be

$$\underline{H}^{i} = \hat{y} H_{y}^{i} = \hat{y} \frac{1}{\eta_0} E_0^{i} e^{-j\beta_0 z + j u_0 x} \tag{3.2}$$

where all subscripts and superscripts are same as in the TE case. In the TM case, Maxwell's equations with source terms (2.1) become

$$\eta \frac{\partial H_y}{\partial z} = -jkE_x - J_x \tag{3.3a}$$

$$\eta \frac{\partial H_y}{\partial x} = jkE_z + J_z \tag{3.3b}$$

$$\left[\frac{\partial E_x}{\partial z} - \frac{\partial E_z}{\partial x} \right] = -jk\eta H_y - M_y \tag{3.3c}$$

The primary field components in the TM case are inferred from the associated planar surface scattering problem. This results in postulating for the primary magnetic

field components (3.4a) and (3.5a) as given below. Using (3.3a,b) with $J_x = J_z = 0$, the primary field components in the upper half-space ($x > D(z)$) are obtained as

$$H_{ya}^{p} = \frac{E_0^i}{\eta_0}[e^{-j\beta_0 z + ju_0 x} - \frac{v_0 - \varepsilon_r u_0}{v_0 + \varepsilon_r u_0} e^{-j\beta_0 z - ju_0(x-2D)}] \tag{3.4a}$$

$$E_{za}^{p} = \frac{u_0}{k_0} E_0^i [e^{-j\beta_0 z + ju_0 x} + \frac{v_0 - \varepsilon_r u_0}{v_0 + \varepsilon_r u_0} e^{-j\beta_0 z - ju_0(x-2D)}] \tag{3.4b}$$

$$E_{xa}^{p} = \frac{E_0^i}{k_0}[\beta_0 e^{-j\beta_0 z + ju_0 x} - (\frac{v_0 - \varepsilon_r u_0}{v_0 + \varepsilon_r u_0})(\beta_0 - 2u_0 D')e^{-j\beta_0 z - ju_0(x-2D)}] \tag{3.4c}$$

and in the lower half- space ($x < D$)

$$H_{yb}^{p} = \frac{E_0^i}{\eta_0}(\frac{2\varepsilon_r u_0}{v_0 + \varepsilon_r u_0})e^{-j\beta_0 z + jv_0 x + j(u_0 - v_0)D} \tag{3.5a}$$

$$E_{zb}^{p} = \frac{v_0}{k_0} E_0^i (\frac{2u_0}{v_0 + \varepsilon_r u_0})e^{-j\beta_0 z + jv_0 x + j(u_0 - v_0)D} \tag{3.5b}$$

$$E_{xb}^{p} = \frac{E_0^i}{k_0}(\frac{2u_0}{v_0 + \varepsilon_r u_0})[\beta_0 - (u_0 - v_0)D']e^{-j\beta_0 z + jv_0 x + j(u_0 - v_0)D} \tag{3.5c}$$

The fields (3.4) and (3.5) satisfy all boundary conditions for a planar interface (i.e., $D = 0$) but the tangential electric field is not continuous at a rough interface (i.e., $D \neq 0$). The boundary condition of continuity of tangential electric fields at a rough interface is expressed as

$$E_{za}^{p} + D'E_{xa}^{p} = E_{zb}^{p} + D'E_{xb}^{p} \quad @\ x = D(z) \tag{3.6}$$

Because this boundary condition is not satisfied, the primary volume current density, obtained by substituting primary fields (3.4) and (3.5) into (3.3c), does not, by itself, lead to the construction of a solution as was done in the TE case. As will be shown shortly, equivalent surface currents that are introduced by the discontinuity of the tangential

electric field on the surface will have to be added to the volume current density formed by using (3.3c). This will be shown in Section 3.2.2.

3.2 Sheet Current

The fictitious magnetic sheet current that is needed to eliminate all the fictitious magnetic current densities both volume and surface in the TM case will now be developed in a fashion similar to that which was done in the TE case. Assume for the moment that only a volume magnetic current density is removed by the fictitious sheet current (refer to Figure 2.3 and replace all electric current densities ($\boldsymbol{J}$, $\boldsymbol{J}_s$) by magnetic current densities ($\boldsymbol{M}$, $\boldsymbol{M}_s$), respectively). The mathematical expression for the cancellation of magnetic volume current density at an arbitrary point $P(x,z_1)$, takes the form:

$$M_y(x,z_1;u_0)+\int_{u=0}^{\infty} M_{sy}(x,z=z_1,u)du=0 \tag{3.7}$$

where M_y and M_{sy} denote magnetic volume current density and magnetic sheet current density, respectively.

3.2.1 Mode Structure

The modal field structure is illustrated in Figure 3.2. The out-going modal amplitude with a particular wave number u and originated from the reference plane $z=z_1$ is denoted

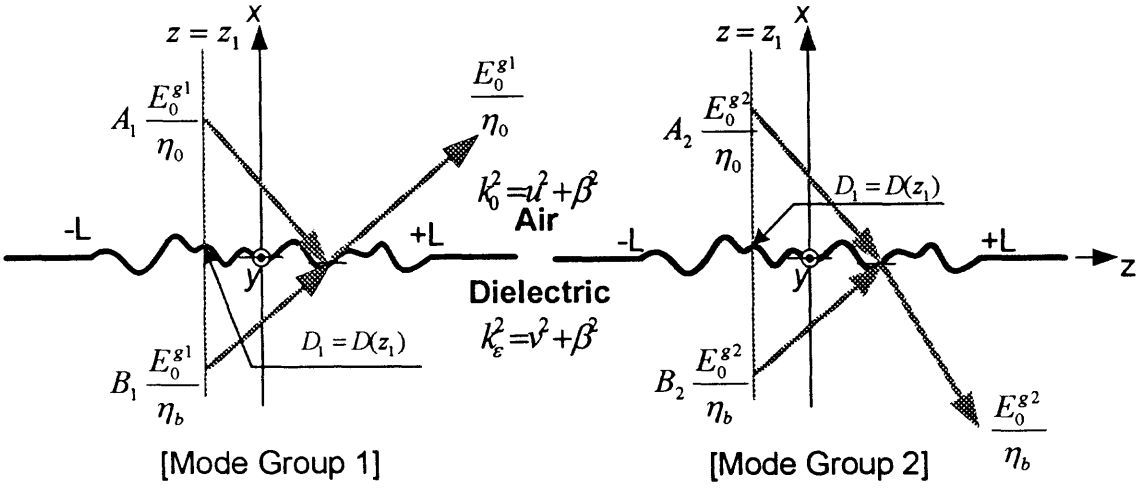

Figure 3.2 Mode structure for TM case.

E_0/η. The subscript g_1 and g_2 denote mode group-1 and group-2, respectively. Intrinsic impedance η is η_0 in air and η_b in the dielectric. A_1 and B_1 (A_2 and B_2) are relative amplitudes determined by the boundary conditions and are given by

$$A_1 = \frac{\varepsilon_r u - v}{\varepsilon_r u + v} \tag{3.8a}$$

$$B_1 = \frac{2\sqrt{\varepsilon_r}\, u}{\varepsilon_r u + v} \tag{3.8b}$$

$$A_2 = \frac{2\sqrt{\varepsilon_r}\, v}{\varepsilon_r u + v} \tag{3.8c}$$

$$B_2 = \frac{v - \varepsilon_r u}{v + \varepsilon_r u} \tag{3.8d}$$

With (3.8), all first-order field components in mode group-1 are obtained as

$$H_{ya}^{g1}(x,z)=\frac{E_0^{g1}}{\eta_0}[e^{-jux}+(\frac{\varepsilon_r u-v}{\varepsilon_r u+v})e^{ju(x-2D)}]e^{-j\beta|z-z_1|} \tag{3.9a}$$

$$E_{za}^{g1}(x,z)=-\frac{u}{k_0}E_0^{g1}[e^{-jux}-(\frac{\varepsilon_r u-v}{\varepsilon_r u+v})e^{ju(x-2D)}]e^{-j\beta|z-z_1|} \tag{3.9b}$$

$$E_{xa}^{g1}(x,z)=\frac{E_0^{g1}}{k_0}[\ddot{\beta}e^{-jux}+(\ddot{\beta}+2uD')(\frac{\varepsilon_r u-v}{\varepsilon_r u+v})e^{ju(x-2D)}]e^{-j\beta|z-z_1|} \tag{3.9c}$$

$$H_{yb}^{g1}(x,z)=\frac{E_0^{g1}}{\eta_0}(\frac{2\varepsilon_r u}{\varepsilon_r u+v})[e^{-jvx-j(u-v)D}]e^{-j\beta|z-z_1|} \tag{3.9d}$$

$$E_{zb}^{g1}(x,z)=-\frac{E_0^{g1}}{k_0}(\frac{2uv}{u+v})[e^{-jvx-j(u-v)D}]e^{-j\beta|z-z_1|} \tag{3.9e}$$

$$E_{xb}^{g1}(x,z)=\frac{E_0^{g1}}{k_0}(\frac{2u}{\varepsilon_r u+v})[\{\ddot{\beta}+(u-v)D'\}e^{-jvx-j(u-v)D}]e^{-j\beta|z-z_1|} \tag{3.9f}$$

The field components in mode group-2 are

$$H_{ya}^{g2}(x,z)=\frac{E_0^{g2}}{\eta_b}(\frac{2v}{v+\varepsilon_r u})[e^{jux-j(u-v)D}]e^{-j\beta|z-z_1|} \tag{3.10a}$$

$$E_{za}^{g2}(x,z)=\frac{E_0^{g2}}{k_\varepsilon}(\frac{2\varepsilon_r uv}{v+\varepsilon_r u})[e^{jux-j(u-v)D}]e^{-j\beta|z-z_1|} \tag{3.10b}$$

$$E_{xa}^{g2}(x,z)=\frac{E_0^{g2}}{k_\varepsilon}(\frac{2\varepsilon_r v}{v+\varepsilon_r u})[\{\ddot{\beta}+(u-v)D'\}e^{jux-j(u-v)D}]e^{-j\beta|z-z_1|} \tag{3.10c}$$

$$H_{yb}^{g2}(x,z)=\frac{E_0^{g2}}{\eta_b}[e^{jvx}+(\frac{v-\varepsilon_r u}{v+\varepsilon_r u})e^{-jv(x-2D)}]e^{-j\beta|z-z_1|} \tag{3.10d}$$

$$E_{zb}^{g2}(x,z)=\frac{E_0^{g2}}{k_\varepsilon}v[e^{jvx}-(\frac{v-\varepsilon_r u}{v+\varepsilon_r u})e^{-jv(x-2D)}]e^{-j\beta|z-z_1|} \tag{3.10e}$$

$$E_{xb}^{g2}(x,z)=\frac{E_0^{g2}}{k_\varepsilon}[\ddot{\beta}e^{jvx}+(\ddot{\beta}-2vD')(\frac{v-\varepsilon_r u}{v+\varepsilon_r u})e^{-jv(x-2D)}]e^{-j\beta|z-z_1|} \tag{3.10f}$$

where $\ddot{\beta}=\mathrm{sgn}(z-z_1)\beta$ as in TE case. The first-order (mode) field is fully specified upon determining the unknown modal amplitudes E_0^{g1} and E_0^{g2}. The modal volume current densities for both mode groups are calculated by substituting (3.9) and (3.10) into (3.3c). Thus

$$M_{ya}^{g1}(x,z)=j\frac{E_0^{g1}}{k_0}(2u\frac{\varepsilon_r u-v}{\varepsilon_r u+v})[2\ddot{\beta}D'+2uD'^2+jD'']e^{ju(x-2D)-j\beta|z-z_1|} \tag{3.11a}$$

$$M_{yb}^{g1}(x,z)=j\frac{E_0^{g1}}{k_0}(2u\frac{u-v}{\varepsilon_r u+v})[2\ddot{\beta}D'+(u-v)D'^2+jD'']e^{-jvx-j(u-v)D-j\beta|z-z_1|} \tag{3.11b}$$

$$M_{ya}^{g2}(x,z)=j\frac{E_0^{g1}}{k_\varepsilon}(2\varepsilon_r v\frac{u-v}{\varepsilon_r u+v})[2\ddot{\beta}D'+(u-v)D'^2+jD'']e^{jux-j(u-v)D-j\beta|z-z_1|} \tag{3.11c}$$

$$M_{yb}^{g2}(x,z)=j\frac{E_0^{g2}}{k_\varepsilon}(2v\frac{\varepsilon_r u-v}{\varepsilon_r u+v})[2\ddot{\beta}D'-2vD'^2+jD'']e^{-jv(x-2D)-j\beta|z-z_1|} \tag{3.11d}$$

which may the mode field errors.

3.2.2 Modal Amplitude

The modal amplitudes are determined by (3.7) using the magnetic sheet current density, which is fictitious, and from the discontinuity of the tangential magnetic field at the z=z_1. The boundary conditions at z=z_1 are given by

$$J_{sx}=\left[H_{y>}-H_{y<}\right]_{z=z_1}=0 \tag{3.12a}$$

$$M_{sy}=-\left[E_{x>}-E_{x<}\right]_{z=z_1}\neq 0 \tag{3.12b}$$

$$\rho_s/\varepsilon_0=\left[E_{z>}-E_{z<}\right]_{z=z_1}=0 \tag{3.12c}$$

Equation (3.12a) implies that $E_0^{g1} = E_{0>}^{g1} = E_{0<}^{g1}$, $E_0^{g2} = E_{0>}^{g2} = E_{0<}^{g2}$ at $z=z_1$. The sheet current density is determined by substituting (3.9)-(3.10) into (3.12b):

$$M_{sy}^{g1} = F_1(u)\psi_{TM}^{g1}(x, z_1; u) \tag{3.13a}$$

$$M_{sy}^{g2} = F_2(v)\psi_{TM}^{g2}(x, z_1; v) \tag{3.13b}$$

where

$$F_1(u) = -E_0^{g1}\frac{2\beta(u)}{k_0} \tag{3.14a}$$

$$F_2(v) = -E_0^{g2}\frac{2\beta(v)}{k_\varepsilon} \tag{3.14b}$$

and

$$\psi_{TM}^{g1}(x, z_1; u) = \begin{cases} e^{-jux} + \dfrac{\varepsilon_r u - v}{\varepsilon_r u + v} e^{ju(x-2D_1)} = \psi_a^{g1}, x > D_1 \\ \dfrac{2u}{\varepsilon_r u + v} e^{-jvx - j(u-v)D_1} = \psi_b^{g1}, \quad x < D_1 \end{cases} \tag{3.15a}$$

$$\psi_{TM}^{g2}(x, z_1; v) = \begin{cases} \dfrac{2\varepsilon_r v}{v + \varepsilon_r u} e^{jux - j(u-v)D_1} = \psi_a^{g2}, \quad x > D_1 \\ e^{jvx} + \dfrac{v - \varepsilon_r u}{v + \varepsilon_r u} e^{-jv(x-2D_1)} = \psi_b^{g2}, x < D_1 \end{cases} \tag{3.15b}$$

Note that the mode functions ψ_{TM}^{g1} and ψ_{TM}^{g2} are different from the TE case. The orthogonality relations for the mode functions, proved in Appendix A, are

$$\int_{x=-\infty}^{+\infty} \varepsilon_r(x)\psi_{TM}^{g1}(x, z_1; u')\psi_{TM}^{*g1}(x, z_1; u)dx = 2\pi\delta(u - u') \tag{3.16a}$$

$$\int_{x=-\infty}^{+\infty} \frac{1}{\bar{\varepsilon}_r(x)}\psi_{TM}^{g2}(x, z_1 v')\psi_{TM}^{*g2}(x, z_1; v)dx = 2\pi\delta(v - v') \tag{3.16b}$$

$$\int_{x=-\infty}^{+\infty} \varepsilon_r(x)\psi_{TM}^{g2}(x,z_1;v')\psi_{TM}^{*g1}(x,z_1;v)dx = 0 \tag{3.16c}$$

$$\int_{x=-\infty}^{+\infty} \frac{1}{\bar{\varepsilon}_r(x)}\psi_{TM}^{g1}(x,z_1u')\psi_{TM}^{*g2}(x,z_1;u)dx = 0 \tag{3.16d}$$

where

$$\varepsilon_r(x) = \begin{Bmatrix} 1, & x > D_1 \\ \varepsilon_r, & x < D_1 \end{Bmatrix}$$

$$\bar{\varepsilon}_r(x) = \begin{Bmatrix} \varepsilon_r, & x > D_1 \\ 1, & x < D_1 \end{Bmatrix}$$

The condition for all the fictitious sheet current densities to cancel all the fictitious volume current densities is expressed as (3.7). Note that the primary volume current density has not yet been completely determined since the primary field distribution violates boundary condition in (3.6), i.e., the tangential electric field is not continuous at the interface. This discontinuity is extracted by integration by parts as shown in the following discussion.

The sheet current density M_{sy} in (3.7) is a superposition of the sheet currents in each mode group. Hence (3.7) is rewritten as

$$M_y(x,z_1;u_0) + \int_{u'=0}^{\infty} M_{sy}^{g1}(x,z_1,u')du + \int_{v'=0}^{\infty} M_{sy}^{g2}(x,z_1,v')dv = 0 \tag{3.17}$$

Substitute (3.13) with (3.14)-(3.15) into (3.17), multiply by $\varepsilon_r(x)\psi_{TM}^{*g1}(x,z_1;u)$, and integrate with respect to x from -∞ to +∞ to obtain

$$\int_{-\infty}^{+\infty} \varepsilon_r(x)M_y\psi_{TM}^{*g1}dx + \int_{-\infty}^{+\infty}\int_{0}^{+\infty} F_1(u')\varepsilon_r(x)\psi_{TM}^{g1}\psi_{TM}^{*g1}du'dx + \int_{-\infty}^{+\infty}\int_{0}^{+\infty} F_2(v')\varepsilon_r(x)\psi_{TM}^{g2}\psi_{TM}^{*g1}dv'dx = 0 \tag{3.18}$$

Use of the orthogonality relations in (3.16) reduces (3.18) to

$$\int_{-\infty}^{+\infty} \varepsilon_r(x) M_y \psi_{TM}^{*g1} dx = -2\pi F_1(u) \tag{3.19a}$$

Multiply (3.17) by $\frac{1}{\bar{\varepsilon}_r(x)} \psi_{TM}^{*g2}(x, z_1; v)$ and integrate with respect to x from -∞ to +∞ yields

$$\int_{-\infty}^{+\infty} \frac{1}{\bar{\varepsilon}_r(x)} M_y \psi_{TM}^{*g2} dx = -2\pi F_2(v) \tag{3.19b}$$

The integrations in (3.19a,b) separate into two regions, above and below the surface:

$$\int_{D}^{+\infty} M_{ya} \psi_a^{*g1} dx + \varepsilon_r \int_{-\infty}^{D} M_{yb} \psi_b^{*g1} dx = -2\pi F_1(u) \tag{3.20a}$$

$$\frac{1}{\varepsilon_r} \int_{D}^{+\infty} M_{ya} \psi_a^{*g2} dx + \int_{-\infty}^{D} M_{yb} \psi_b^{*g2} dx = -2\pi F_2(v) \tag{3.20a}$$

where the volume current densities (M_{ya} and M_{yb}) are founded from Maxwell's equation (3.3c):

$$M_y = \left[\frac{\partial E_x}{\partial z} - \frac{\partial E_z}{\partial x} \right] - jk\eta H_y \tag{3.21}$$

Substituting (3.21) into (3.20a) allows the first integral in (3.20a) is expressed as

$$\int_{D}^{+\infty} M_{ya} \psi_a^{*g1} dx = \int_{D}^{+\infty} \frac{\partial E_{za}}{\partial x} \psi_a^{*g1} dx - \int_{D}^{+\infty} \frac{\partial E_{xa}}{\partial z} \psi_a^{*g1} dx - j\omega\mu_0 \int_{D}^{+\infty} H_{ya} \psi_a^{*g1} dx \tag{3.22}$$

Employing the relations

$$\frac{\partial E_{xa}}{\partial z} \psi_a^{*g1} = \frac{\partial}{\partial z} [E_{xa} \psi_a^{*g1}] - E_{xa} \frac{\partial}{\partial z} \psi_a^{*g1} \tag{3.23}$$

and applying Lebniz's theorem [12] gives

$$\frac{\partial}{\partial z} \int_{D(z)}^{+\infty} E_{xa} \psi_a^{*g1} dx = \int_{D}^{+\infty} \frac{\partial}{\partial z} [E_{xa} \psi_a^{*g1}] dx + E_{xa} \psi_a^{*g1} D' \Big|_{x=\infty} - E_{xa} \psi_a^{*g1} D' \Big|_{x=D} \tag{3.24}$$

where the second term of the right-hand side in (3.24) vanishes. Substituting (3.22)-(3.24) into (3.20a) and integrating by parts, yields for the first integral of (3.20a)

$$\int_{D}^{+\infty} M_{ya}\psi_a^{*g1}dx = \int_{D}^{\infty}[-E_{za}\frac{\partial}{\partial x}\psi_a^{*g1} + E_{xa}\frac{\partial}{\partial z}\psi_a^{*g1}]dx - \frac{\partial}{\partial z}\int_{D}^{+\infty} E_{xa}\psi_a^{*g1}dx$$

$$- j\omega\mu_0\int_{D}^{+\infty} H_{ya}\psi_a^{*g1}dx - [E_{za} + D'E_{xa}]\psi_a^{*g1}\Big|_{x=D} \qquad (3.25)$$

The second integral in (3.20a) can be expanded in a similar fashion. Equation (3.20a) then becomes

$$\int_{D}^{+\infty} M_{ya}\psi_a^{*g1}dx + \varepsilon_r\int_{-\infty}^{D} M_{yb}\psi_b^{*g1}dx =$$

$$\int_{D}^{\infty}[-E_{za}\frac{\partial}{\partial x}\psi_a^{*g1} + E_{xa}\frac{\partial}{\partial z}\psi_a^{*g1}]dx + \varepsilon_r\int_{-\infty}^{D}[-E_{zb}\frac{\partial}{\partial x}\psi_b^{*g1} + E_{xb}\frac{\partial}{\partial z}\psi_b^{*g1}]dx$$

$$-\frac{\partial}{\partial z}\left[\int_{D}^{+\infty} E_{xa}\psi_a^{*g1}dx + \varepsilon_r\int_{-\infty}^{D} E_{xb}\psi_b^{*g1}dx\right] - j\omega\mu_0\left[\int_{D}^{+\infty} H_{ya}\psi_a^{*g1}dx + \varepsilon_r\int_{-\infty}^{D} H_{yb}\psi_b^{*g1}dx\right]$$

$$-\left[(E_{za} + D'E_{xa}) - (E_{zb} + D'E_{xb})\right]_{x=D}\psi_D^{*g1} \qquad (3.26)$$

where

$$\psi_D^{*g1} = \psi_a^{*g1}\Big|_{x=D} = \varepsilon_r\psi_b^{*g1}\Big|_{x=D} \qquad (3.27)$$

The last term in (3.26) is recognizable as the discontinuity in the tangential electric field at the surface $x=D(z)$, as opposed to continuity expressed in (3.6). This electric field discontinuity can be viewed as being equivalent to a magnetic current distribution on the surface. This surface magnetic current must also be reduced to zero by the fictitious sheet currents so that the boundary condition that the tangential electric field at the surface be continuous is satisfied. This is accomplished by introducing an "effective

fictitious volume current density (M_y^{eff})" that includes the above equivalent magnetic surface current density so that both the volume and equivalent magnetic surface current densities will be cancelled by a superposition of sheet current densities. Mathematically this is accomplished by replacing M_y in (3.19a) by M_y^{eff} which is defined in (3.29) and repeating the steps leading to (3.26):

$$\int_{-\infty}^{+\infty} \varepsilon_r(x) M_y^{eff} \psi_{TM}^{*g1} dx =$$

$$\int_{D}^{\infty} [-E_{za} \frac{\partial}{\partial x} \psi_a^{*g1} + E_{xa} \frac{\partial}{\partial z} \psi_a^{*g1}] dx + \varepsilon_r \int_{-\infty}^{D} [-E_{zb} \frac{\partial}{\partial x} \psi_b^{*g1} + E_{xb} \frac{\partial}{\partial z} \psi_b^{*g1}] dx$$

$$-\frac{\partial}{\partial z}\left[\int_{D}^{+\infty} E_{xa} \psi_a^{*g1} dx + \varepsilon_r \int_{-\infty}^{D} E_{xb} \psi_b^{*g1} dx\right] - j\omega\mu_0 \left[\int_{D}^{+\infty} H_{ya} \psi_a^{*g1} dx + \varepsilon_r \int_{-\infty}^{D} H_{yb} \psi_b^{*g1} dx\right] \quad (3.28)$$

with M_y^{eff} defined to include the discontinuity in the tangential electric field at x=D:

$$M_y^{eff} = M_y + [(E_{za} + D'E_{xa}) - (E_{zb} + D'E_{xb})]\delta(x - D) \quad (3.29)$$

Hence, (3.7) is reformulated in terms of the effective volume current density denoted M_y^{eff}. Thus (3.19a) in view of (3.28) becomes

$$\int_{D}^{\infty} [-E_{za}^p \frac{\partial}{\partial x} \psi_a^{*g1} + E_{xa}^p \frac{\partial}{\partial z} \psi_a^{*g1}] dx + \varepsilon_r \int_{-\infty}^{D} [-E_{zb}^p \frac{\partial}{\partial x} \psi_b^{*g1} + E_{xb}^p \frac{\partial}{\partial z} \psi_b^{*g1}] dx$$

$$-\frac{\partial}{\partial z}\left[\int_{D}^{+\infty} E_{xa}^p \psi_a^{*g1} dx + \varepsilon_r \int_{-\infty}^{D} E_{xb}^p \psi_b^{*g1} dx\right] - j\omega\mu_0 \left[\int_{D}^{+\infty} H_{ya}^p \psi_a^{*g1} dx + \varepsilon_r \int_{-\infty}^{D} H_{yb}^p \psi_b^{*g1} dx\right] = -2\pi F_1^{(1)}(u)$$

(3.30a)

where superscripts p and (1) denote primary and first-order, respectively. This procedure can be used to show that (3-19b) becomes

$$\int_{D}^{\infty}[-E_{za}^{p}\frac{\partial}{\partial x}\psi_{a}^{*g2}+E_{xa}^{p}\frac{\partial}{\partial z}\psi_{a}^{*g2}]dx+\varepsilon_{r}\int_{-\infty}^{D}[-E_{zb}^{p}\frac{\partial}{\partial x}\psi_{b}^{*g2}+E_{xb}^{p}\frac{\partial}{\partial z}\psi_{b}^{*g2}]dx$$

$$-\frac{\partial}{\partial z}\left[\int_{D}^{+\infty}E_{xa}^{p}\psi_{a}^{*g2}dx+\varepsilon_{r}\int_{-\infty}^{D}E_{xb}^{p}\psi_{b}^{*g2}dx\right]-j\omega\mu_{0}\left[\int_{D}^{+\infty}H_{ya}^{p}\psi_{a}^{*g2}dx+\varepsilon_{r}\int_{-\infty}^{D}H_{yb}^{p}\psi_{b}^{*g2}dx\right]=-2\pi F_{2}^{(1)}(v)$$

(3.30b)

Substituting (3.4)-(3.5), (3.14)-(3.15) into (3.30), the first-order modal amplitudes for mode group-1 and mode group-2 are obtained to be

$$E_{0}^{g1}(z_{1},u;u_{0})=j\frac{E_{0}^{i}}{2\pi\beta}\left(\frac{u_{0}}{v_{0}+\varepsilon_{r}u_{0}}\right)e^{-j\beta_{0}z_{1}+j(u_{0}+u)D_{1}}\left[W_{1}(D_{1})\left(\frac{(v_{0}-\varepsilon_{r}u_{0})(v^{*}+\varepsilon_{r}u_{0})}{v^{*}+\varepsilon_{r}u}\right)\varsigma_{1}(u,u_{0})\right.$$

$$\left.+W_{2}(D_{1})\left(\frac{-j2\varepsilon_{r}u(v_{0}-u_{0})}{(v^{*}+v_{0})(v^{*}+\varepsilon_{r}u)}\right)+(\varepsilon_{r}-1)W_{3}(D_{1})\frac{2\varepsilon_{r}u}{v^{*}+\varepsilon_{r}u}\right] \quad (3.31a)$$

$$E_{0}^{g2}(z_{1},v;u_{0})=j\frac{E_{0}^{i}}{2\pi\beta}\left(\frac{u_{0}\sqrt{\varepsilon_{r}}}{v_{0}+\varepsilon_{r}u_{0}}\right)\left(\frac{v-\varepsilon_{r}u^{*}}{v+\varepsilon_{r}u^{*}}\right)e^{-j\beta_{0}z_{1}+j(u_{0}-v)D_{1}}\left[W_{1}(D_{1})\left(\frac{-j2v}{(v+\varepsilon_{r}u^{*})(u^{*}+u_{0})}\right)\right.$$

$$\left.+W_{2}(D_{1})\left(\frac{(v_{0}-u_{0})(v_{0}+\varepsilon_{r}u)}{(v+\varepsilon_{r}u^{*})}\right)\varsigma_{2}(v,v_{0})-(\varepsilon_{r}-1)W_{3}(D_{1})\frac{2v}{v+\varepsilon_{r}u^{*}}\right] \quad (3.31b)$$

where $W_1(D_1)$,$W_2(D_1)$ and $\varsigma_1(u,u_0)$, $\varsigma_1(u,u_0)$ are given in (2.25) and (2.26), respectively, and

$$W_{3}(D_{1})=\beta_{0}D_{1}'-u_{0}D_{1}'^{2} \quad (3.32)$$

The third term in the bracket is a consequence of incorporating the equivalent magnetic surface current density in M_{y}^{eff} which is not presented in the TE case.

3.3 First-order Scattered Far Field

The first-order field is obtained by superimposing the modes of both groups as given by (3.9)-(3.10) with the modal amplitudes E_0^{g1}, E_0^{g2} specified in (3.31).

3.3.1 Upper Half-Space

The first-order field in the upper half-space ($x>D(z)=0$ for $|z|>L$) is expressed as a superposition of the orthogonal mode fields belonging to the mode group-1 and the mode group–2 as follows:

$$H_{ya}^{(1)}(x,z) = \int_{-L}^{L}\int_{0}^{\infty} H_{ya}^{g1}(x,z;z_1,u)dudz_1 + \int_{-L}^{L}\int_{0}^{\infty} H_{ya}^{g2}(x,z;z_1,v)dvdz_1 \tag{3.33}$$

where H_{ya}^{g1} and H_{ya}^{g2} are given in (3.9a) and (3.10a), and which are expressed in terms of mode function given in (3.15):

$$H_{ya}^{g1}(x,z,z_1;u) = \frac{E_0^{g1}(z_1,u)}{\eta_0}\psi_{TM}^{g1}(x,z_1;u)e^{-j\beta|z-z_1|} \tag{3.34a}$$

$$H_{ya}^{g2}(x,z,z_1;v) = \frac{E_0^{g2}(z_1,v)}{\eta_b}\psi_{TM}^{g2}(x,z_1;v)e^{-j\beta|z-z_1|} \tag{3.34b}$$

Substituting (3.34) into (3.33) with (3.31) for modal amplitudes (E_0^{g1}, E_0^{g2}) and (3.15) for mode functions ($\psi_{TM}^{g1}, \psi_{TM}^{g2}$), interchanging the order of integration after deforming the u-integration off the real u-axis (as in Figure 2.5), integrating over z_1 using (2.30), and employing

$$\int_{-L}^{L} W_3(D_1) e^{j(u_0+u)D_1 - j\beta|z-z_1| - j\beta_0 z_1} dz_1$$

$$= \frac{\beta_0(\beta-\beta_0)}{(u_0+u)} \int_{-L}^{L} \left[1 - \left\{ 1 + \frac{u_0(u_0+u)}{\beta_0(\beta-\beta_0)} D_1'^2 \right\} e^{j(u_0+u)D_1} \right] e^{-j\beta|z-z_1| - j\beta_0 z_1} dz_1 \quad (3.35)$$

where $W_3(D_1)$ is given in (3.32) and $D(\pm L)=D'(\pm L)=0$ yields

$$H_{ya}^{(1)}(x,z) = \frac{E_0^i}{\eta_0}\left(\frac{\varepsilon_r - 1}{\pi}\right)\int_0^{k_0}\left(\frac{u_0 u}{(v_0+\varepsilon_r u_0)(v+\varepsilon_r u)(u_0+u)}\right) e^{-jux - j\beta z}$$

$$\times \left[(\varepsilon_r \beta_0 \beta - v_0 v) \int_{-L}^{L} \left\{ 1 - e^{j(u_0+u)D_1} \right\} e^{j(\beta-\beta_0)z_1} dz_1 \right.$$

$$\left. + \left(\frac{\varepsilon_r k_0^2 (u_0 + u - v_0 - v)}{v_0 + v} + (v_0 v - \varepsilon_r u_0 u) \right) \int_{-L}^{L} D_1'^2 e^{j(u_0+u)D_1 + j(\beta-\beta_0)z_1} dz_1 \right] \frac{du}{\beta} \quad (3.36)$$

Note that (3.36) does not include in-coming modes since it is already known that only propagating out-going modes from the surface contribute to the far field. For modes propagating in air, the wave numbers β and u are positive real within $0 \le u, \beta \le k_0$. This means from (2.12) that v is also real; hence u and v replace u^* and v^*, respectively, in (3.36). The integration with respect to u is evaluated by the stationary phase approximation similar to the TE case. The magnetic far field is then obtained to be

$$H_{ya}^{(1)ff}(\phi,\phi_0) = \left[\frac{E_0^i}{\eta_0} \sqrt{\frac{2\pi}{k_0 \rho}}\, e^{-jk_0\rho + j\frac{\pi}{4}} \right] R_{11}^{TM}(\phi,\phi_0) \quad (3.37)$$

where the scatter pattern (R_{11}) in the upper half-space due to an incident plane wave in the upper half-space is given by

$$R_{11}^{TM}(\phi,\phi_0)=\left(\frac{\varepsilon_r-1}{\pi}\right)\left[\frac{u_0u(\varepsilon_r\beta_0\beta-v_0v)}{(v_0+\varepsilon_r u_0)(v+\varepsilon_r u)(u_0+u)}\right]$$

$$\times\int_{-L}^{L}\left[1-\left\{1-\frac{C_{11}}{(\varepsilon_r\beta_0\beta-v_0v)}D_1'^2\right\}e^{j(u_0+u)D_1}\right]e^{-j(\beta_0-\beta)z_1}dz_1 \quad (3.38)$$

where

$$C_{11}=\frac{\varepsilon_r k_0^2(u_0+u-v_0-v)}{v_0+v}+(v_0v-\varepsilon_r u_0u),$$

and

$$u_0=k_0\cos\phi_0\ ,\ v_0=k_0\sqrt{\varepsilon_r-\sin^2\phi_0}\ ,\ \beta_0=k_0\sin\phi_0$$

$$u=k_0\cos\phi\ ,\ v=k_0\sqrt{\varepsilon_r-\sin^2\phi}\ ,\ \beta=k_0\sin\phi$$

$$D_1=D(z_1),\quad D_1'=\left.\frac{dD(z)}{dz}\right|_{z=z_1}$$

which is valid for $-\pi/2\le\phi\le\pi/2$, $-\pi/2\le\phi_0\le\pi/2$. The scattering geometry is depicted in Figure 2.7 with incident magnetic field given by (3.2).

3.3.2 Lower Half-Space

The first-order field in the dielectric is determined by a superposition of the all mode fields in the lower half-space:

$$H_{yb}^{(1)}(x,z)=\int_{-L}^{L}\int_{0}^{\infty}H_{yb}^{g1}(x,z,z_1;u)dudz_1+\int_{-L}^{L}\int_{0}^{\infty}H_{yb}^{g2}(x,z,z_1;v)dvdz_1 \quad (3.39)$$

Evaluation of the integrals in the above equation follows the procedure described in Section 3.3.1 by using the integral evaluations in (2.30) and (3.35), after substituting (3.9d) and (3.10d) with (3.15) and (3.31) into (3.39):

$$H_{yb}^{(1)ff}(x,z)=\frac{E_0^i}{\eta_0}\left(\frac{\varepsilon_r(\varepsilon_r-1)}{\pi}\right)\int_0^{k_0\sqrt{\varepsilon_r}}\left(\frac{u_0 v}{(v_0+\varepsilon_r u_0)(v+\varepsilon_r u^*)}\right)e^{jvx-j\beta z}$$

$$\times\left[\frac{v_0u^*+\beta_0\beta}{u_0-v}\int_{-L}^{L}\left\{1-e^{j(u_0-v)D_1}\right\}e^{j(\beta-\beta_0)z_1}dz_1\right.$$

$$\left.+\left(\frac{k_0^2(\varepsilon_r u_0+\varepsilon_r u^*-v_0-v)+(u_0u^*-u^*v_0)(v_0-u^*)}{(u_0+u^*)(v_0+v)}\right)\int_{-L}^{L}D_1'^2e^{j(u_0-v)D_1+j(\beta-\beta_0)z_1}dz_1\right]\frac{dv}{\beta}$$

(3.40)

Note that u^* can not be replaced by u since u does not have to be real even though v is real for propagating modes in the lower half-space; see (2.12) for $0\le v\le k\sqrt{\varepsilon_r}$. The above result omits incoming modes that do not contribute to the far field. The integral evaluation can be realized by stationary phase approximation. The magnetic far field in the dielectric is obtained as

$$H_{yb}^{(1)ff}(\bar{\phi},\phi_0)=\left[\frac{E_0^i}{\eta_0}\sqrt{\frac{2\pi}{k_\varepsilon\rho}}\,e^{-jk_b\rho+j\frac{\pi}{4}}\right]R_{12}^{TM}(\phi,\phi_0) \tag{3.41}$$

where the scatter pattern (R_{12}) in the lower half-space due to an incident plane wave in the upper half-space is given by

$$R_{12}^{TM}(\phi,\phi_0)=\left(\frac{\varepsilon_r(\varepsilon_r-1)}{\pi}\right)\left[\frac{u_0 v}{(v_0+\varepsilon_r u_0)(v+\varepsilon_r u^*)}\right]$$

$$\times\int_{-L}^{L}\left[\frac{v_0u^*+\beta_0\beta}{u_0-v}\left\{1-e^{j(u_0-v)D_1}\right\}+C_{12}D_1'^2e^{j(u_0-v)D_1}\right]e^{j(\beta-\beta_0)z_1}dz_1 \tag{3.42}$$

where

$$C_{12}=\frac{k_0^2(\varepsilon_r u_0+\varepsilon_r u^*-v_0-v)+(u_0u^*-u^*v_0)(v_0-u^*)}{(u_0+u^*)(v_0+v)},$$

and

$$u_0 = k_0 \cos\phi_0 \quad , \quad v_0 = k_0\sqrt{\varepsilon_r - \sin^2\phi_0} \quad , \quad \beta_0 = k_0 \sin\phi_0$$

$$u^* = k_0\sqrt{\varepsilon_r \sin^2\bar{\phi} - 1} \quad , \quad v = \sqrt{\varepsilon_r}k_0 \cos\bar{\phi} \quad , \quad \beta = \sqrt{\varepsilon_r}k_0 \sin\bar{\phi}$$

The scatter pattern expression in (3.42) is valid for $-\pi/2 \le \bar{\phi} \le \pi/2$, $-\pi/2 \le \phi_0 \le \pi/2$. The scattering geometry is depicted in Figure 2.9 where the incident field is now given by H_y^i in (3.2).

CHAPTER 4

VERIFICATION OF THEORY

In the previous chapters, the first-order fields were determined. The actual field is then approximated by adding the primary field to the first-order field; higher-order terms are neglected. That all higher-order terms are small is inferred by the numerical results presented in Chapter 5 where comparisons are made to data generated using a Method of Moments (MoM) evaluation of exact integral equations. This check on the accuracy of the solution is limited since it is a purely numerical check and is performed for a finite number of surface parameters. In this chapter, first-order field solutions are verified by showing that they satisfy reciprocity and obey an error criterion.

4.1 Reciprocity

Reciprocity is a well-known physical principle. In circuit analysis, reciprocity is written for a 2-port passive linear network as

$$V^A I^B = V^B I^A \tag{4.1}$$

where superscripts A and B denotes two states. This relation states that the output short circuit current I^A due to an input voltage V^A is the same as the short circuit current I^B at the input due to V^B in the output terminal if V^B is equal to V^A. The more general reciprocity relationship is obtained from Maxwell's equations and is called the "Lorentz reciprocity theorem". For the bounded domain V with boundary surface S, the Lorentz theorem in integral form is written as [7]

$$\oiint_S (\underline{E}^A \times \underline{H}^B - \underline{E}^B \times \underline{H}^A) \cdot d\underline{s} = \iiint_V (\underline{E}^A \times \underline{J}^B + \underline{H}^B \times \underline{M}^A - \underline{E}^B \times \underline{J}^A - \underline{H}^A \times \underline{M}^B) dv \tag{4.2}$$

where $\underline{J}$ and $\underline{M}$ denote electric and magnetic current density, respectively. In a source-free region, the reciprocity theorem written in (4.2) reduces to

$$\oiint_S (\underline{E}^A \times \underline{H}^B - \underline{E}^B \times \underline{H}^A) \cdot d\underline{s} = 0 \tag{4.3}$$

Let the total fields be expressed as incident ($\underline{E}^i$, $\underline{H}^i$) and scattered ($\underline{E}^s$, $\underline{H}^s$) fields; equation (4.3) then becomes

$$\oiint_S (\underline{E}^{i,A} \times \underline{H}^{s,B} - \underline{E}^{s,B} \times \underline{H}^{i,A}) \cdot d\underline{s} = \oiint_S (\underline{E}^{i,B} \times \underline{H}^{s,A} - \underline{E}^{s,A} \times \underline{H}^{i,B}) \cdot d\underline{s} \tag{4.4}$$

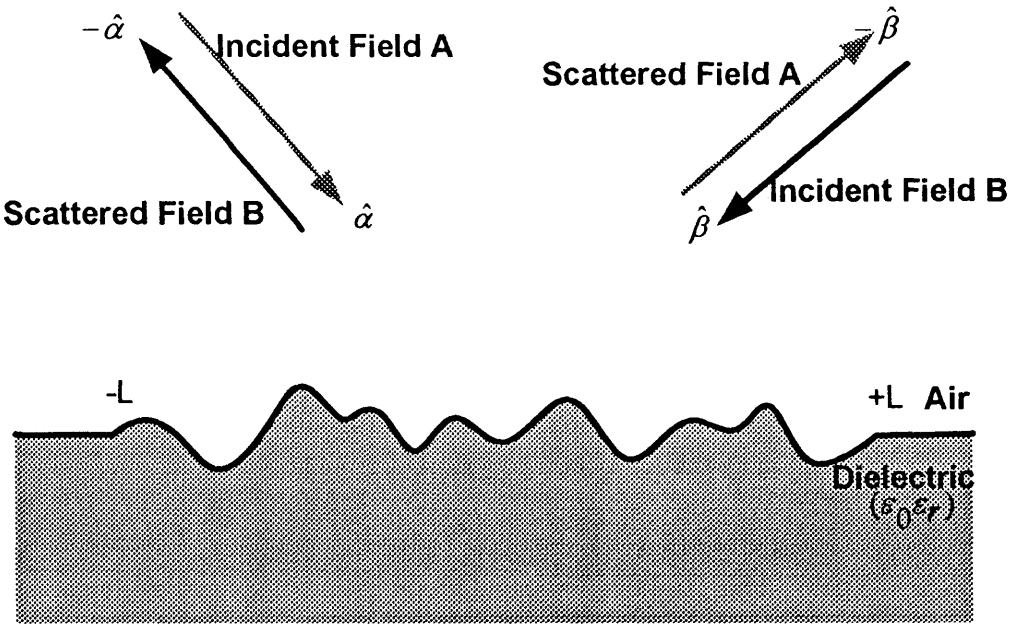

Figure 4.1 Illustration for reciprocity relation between two states of incident and scattered fields with their wave vector directions.

Let each incident plane wave field take the form

$$\left\lfloor \underline{E}^{i,A}, \underline{H}^{i,A} \right\rfloor = \left\lfloor \underline{e}^i_{\hat{\alpha}}, \underline{h}^i_{\hat{\alpha}} \right\rfloor \exp(-jk_0 \hat{\alpha} \cdot \underline{r}) \tag{4.5a}$$

$$\left\lfloor \underline{E}^{i,B}, \underline{H}^{i,B} \right\rfloor = \left\lfloor \underline{e}^{i}_{\hat{\beta}}, \underline{h}^{i}_{\hat{\beta}} \right\rfloor \exp(-jk_0 \hat{\beta} \cdot \underline{r}) \tag{4.5b}$$

where $\hat{\alpha}$ and $\hat{\beta}$ are the unit vectors representing the direction of propagation; see figure 4.1. For plane wave excitation of the scattering surface, $\left\lfloor \underline{E}^{s,A}, \underline{H}^{s,A} \right\rfloor$ and $\left\lfloor \underline{E}^{s,B}, \underline{H}^{s,B} \right\rfloor$ can be expressed as

$$\left\lfloor \underline{E}^{s,A}, \underline{H}^{s,A} \right\rfloor = \left\lfloor e^{s}_{\hat{\alpha}}, \underline{h}^{s}_{\hat{\alpha}} \right\rfloor \exp(-jk_0 \hat{\alpha}_s \cdot \underline{r}) \tag{4.5c}$$

$$\left\lfloor \underline{E}^{s,B}, \underline{H}^{s,B} \right\rfloor = \left\lfloor \underline{e}^{s}_{\hat{\beta}}, \underline{h}^{s}_{\hat{\beta}} \right\rfloor \exp(-jk_0 \hat{\beta}_s \cdot \underline{r}) \tag{4.5d}$$

where $\underline{r} = \underline{\rho} = \hat{x}x + \hat{z}z$. Substituting (4.5) into (4.4), the reciprocity relation is obtained [13]:

$$\underline{e}^{i}_{\hat{\alpha}} \cdot \underline{e}^{s}_{\hat{\beta}}(-\hat{\alpha}) = \underline{e}^{i}_{\hat{\beta}} \cdot \underline{e}^{s}_{\hat{\alpha}}(-\hat{\beta}) \tag{4.6}$$

$$\underline{h}^{i}_{\hat{\alpha}} \cdot \underline{h}^{s}_{\hat{\beta}}(-\hat{\alpha}) = \underline{h}^{i}_{\hat{\beta}} \cdot \underline{h}^{s}_{\hat{\alpha}}(-\hat{\beta}) \tag{4.7}$$

For the scatter geometry studied, now the reciprocity theorem requires with the solutions (2.36) and (3.38) and using (4.6)-(4.7) that:

$$R(\phi_s = -\phi_0, \phi_i = -\phi) = R(\phi_s = \phi, \phi_i = \phi_0) \tag{4.8}$$

where ϕ_i and ϕ_s are incident and scattering angle, respectively, and R denotes a scatter pattern of both TE- and TM- polarization case, written in (2.36) and (3.38), respectively. This is rewritten using the scattering geometry in Figure (2.7) as follows:

$$R_{11}^{TE,TM}(-\phi_0, -\phi) = R_{11}^{TE,TM}(\phi, \phi_0) \tag{4.9}$$

Replacing ϕ and ϕ_0 by $-\phi_0$ and $-\phi$ in both (2.36) and (3.38), respectively, shows reciprocity is satisfied. An alternative form of the reciprocity relation is

$$R_{11}^{TE,TM}(u_0, v_0, -\beta_0, u, v, -\beta) = R_{11}^{TE,TM}(u, v, \beta, u_0, v_0, \beta_0) \tag{4.10}$$

which is simply obtained by interchanging the angles of incident and scattered so each of x- and z- directed wave number is replaced as (4.10).

For the scatter pattern in the lower half space, reciprocity relation given in (4.8) must also be satisfied, i.e.,

$$R_{22}^{TE,TM}(-\phi_0,-\phi) = R_{22}^{TE,TM}(\phi,\phi_0) \tag{4.11}$$

To prove (4.11) for the scatter pattern in the lower half-space due to an incident plane wave in lower half-space in TE- and TM- polarization, one needs to derive $R_{22}^{TM}(\phi,\phi_0)$ and $R_{22}^{TE}(\phi,\phi_0)$. These expressions are obtained by following the procedure presented in Chapter 2 and 3. The result for TE- polarization case is

$$R_{22}^{TE}(\phi,\phi_0) = \left[-\frac{k_0^2}{\pi}(\varepsilon_r - 1)\right]\left[\frac{v_0 v}{(u_0+v_0)(u^*+v)}\right]$$

$$\times \int_{-L}^{L}\left\{\left[\frac{1-e^{j(v_0+v)D_1}}{u_0+v}\right]+\left[\frac{1}{u_0+u^*}-\frac{1}{v+v_0}\right]D_1'^2 e^{j(v_0+v)D_1}\right\}e^{-j(\beta_0-\beta)z_1}dz_1 \tag{4.12}$$

and TM polarization case is

$$R_{22}^{TM}(\phi,\phi_0) = \left(\frac{\varepsilon_r - 1}{\pi}\right)\left[\frac{v_0 v(\varepsilon_r u_0 u^* - \beta_0\beta)}{(v_0+\varepsilon_r u_0)(v+\varepsilon_r u^*)(v_0+v)}\right]$$

$$\times \int_{-L}^{L}\left[1-\left\{1-\frac{C_{22}}{(\varepsilon_r u_0 u^* - \beta_0\beta)}D_1'^2\right\}e^{-j(v_0+v)D_1}\right]e^{-j(\beta_0-\beta)z_1}dz_1 \tag{4.13}$$

where

$$C_{22} = \frac{\varepsilon_r k_0^2(v_0+v-u_0-u^*)+(\varepsilon_r u_0 u^* - v_0 v)(u_0+u^*)}{(u_0+u^*)}$$

The reciprocity relation given in (4.11) is verified by using the relation (4.10) into (4.12) and (4.13) for both polarization cases in lower half space. Note that reciprocity relation

does not give assurance that the scatter pattern is correct. Satisfaction of reciprocity is a necessary condition for scattered patterns to be a valued solution.

4.2 Error Criterion

Since the actual scattered field solution is approximated only to first-order, its accuracy needs to be quantified. This is accomplished by formulating an error criterion. Such a criterion is used to indicate the range of surface parameters for which the fictitious current solution is expected to yield sufficiently accurate results. In Chapter 2, the FC-theory introduces radiation modes, which provide a complete, orthogonal system that are used to represent the scattered field. Individually, these modes satisfy Maxwell's equations:

$$\nabla \times \boldsymbol{E}^M = -jk\eta \boldsymbol{H}^M - \boldsymbol{M}^M \tag{4.14a}$$

$$\nabla \times \boldsymbol{H}^M = j\frac{k}{\eta}\boldsymbol{E}^M + \boldsymbol{J}^M \tag{4.14b}$$

where, k and η represent the wavenumber and intrinsic wave impedance, respectively, in each half-space. $\boldsymbol{E}^M$, $\boldsymbol{H}^M$ denote mode fields and $\boldsymbol{J}^M$ and $\boldsymbol{M}^M$ denote passive mode current densities for which explicit expressions are given in Section 2.2.1 for TE polarization and Section 3.2.1 for TM polarization case. In the theory, modes are represented by two independent groups (mode group-1 and mode group-2) and each mode group satisfies (4.14). An error criterion is presented below which, for convenience, applies to the upper half-space ($x > D(z), |z| < \infty$) since numerical evaluations are performed only in the upper half-space and for each polarization case.

For TE-polarization case, $M^M = 0$ and $J^M \neq 0$ in (4.14b). Each higher-order field solution is expressed as a superposition of modes, which satisfy (4.14). The total field is expressed as a summation of the primary field plus all the higher-order scattered fields, i.e.,

$$\underline{E} \approx \underline{E}^p + \underline{E}^{s(1)} + \underline{E}^{s(2)} + \cdots + \underline{E}^{s(m)} + \cdots$$

If the solution is truncated after the mth constituent scattered field then according to the theory all passive volume currents have been eliminated leaving only the volume currents belonging to $\underline{E}^{s(m)}$, namely, $\underline{J}^{(m)}$. This current, if the solution is meaningful, must be converging toward zero. It is expected that the more iterations performed, the better the FC- solution approaches the exact field solution. It is also expected that $\underline{J}^{(m)}$ gets smaller relative to the modal field term on the right-hand side of (4.14b). Hence, to ascertain when this occurs, the following condition should apply:

$$\left\langle \left| J^M \right|^2 \right\rangle << (\frac{k_0}{\eta_0})^2 \left\langle \left| E^M \right|^2 \right\rangle \tag{4.15}$$

where $\langle \cdots \rangle$ denotes averaging over z. If this criterion is satisfied then it is expected that the solution converges to the exact solution when sufficient number of iterations is taken. Using the notation for each mode component in (2.14) to (2.16), inequality (4.15) splits into two mode groups:

$$\left\langle \left| J_{ya}^{g1} \right|^2 \right\rangle << (\frac{k_0}{\eta_0})^2 \left\langle \left| E_{ya}^{g1} \right|^2 \right\rangle, \text{ for mode group-1} \tag{4.16a}$$

$$\left\langle \left| J_{ya}^{g2} \right|^2 \right\rangle << (\frac{k_0}{\eta_0})^2 \left\langle \left| E_{ya}^{g2} \right|^2 \right\rangle, \text{ for mode group-2} \tag{4.16b}$$

Substituting (2.14a) and (2.16a) into (4.16a) and assuming that the surface profile $D(z)$ satisfies the conditions $\langle D' \rangle = \langle D'' \rangle = 0$, $\langle D'^3 \rangle = 0$ it follows that

$$\frac{1}{k_0^2}\left[4\beta^2 < D'^2 > +4u^2 < D'^4 > + < D''^2 >\right] << \frac{k_0^2}{4u^2} \tag{4.17}$$

The scattered field was determined by including only the "propagating" modes, described in the previous chapters. This implies that u is positive real values within $0 \le u \le k_0$ and that $0 \le \beta \le k_0$. Hence, it is reasonable to approximate both u^2 and β^2 in (4.17) by $k_0^2/2$, which is their median value. This assumption is reasonable since the magnitude of the field errors is of interested rather than their exact values. With this assumption, the inequality (4.17) reduces to the following error criterion:

$$Q_{TE}^{g1}(D', D'') = 4\left[< D'^2 > + < D'^4 > + \frac{1}{2k_0^2} < D''^2 >\right] << 1 \tag{4.18}$$

which is only for the TE-polarization case of the mode group-1. Substituting (2.15a) and (2.16c) into (4.16b) for mode group-2 yields

$$\frac{1}{k_0^2}\left[4\beta^2 < D'^2 > +(u-v)^2 < D'^4 > + < D''^2 >\right] << \frac{k_0^2}{(u-v)^2} \tag{4.19}$$

The range $0 \le u^2 \le k_0^2$ and $k_0^2(\varepsilon_r - 1) \le v^2 \le k_0^2 \varepsilon_r$ gives $u<v$ so that inequality (4.19) remains valid even if $(u-v)^2$ is replaced by $(v^2 - u^2)$ since for $u<v$

$$(u-v)^2 = u^2 + v^2 - 2uv < v^2 - u^2 \tag{4.20}$$

Again using the approximation, $u^2 \cong \beta^2 \cong k_0^2/2$, it follows that

$$v^2 - u^2 = (k_0^2 \varepsilon_r - \beta^2) - u^2 \cong k_0^2(\varepsilon_r - 1) \tag{4.21}$$

Applying (4.20) and substituting (4.21) into (4.19) yields an error criterion for the TE-polarization case of mode group-2 as follows

$$Q_{TE}^{g2}(D',D'') = (\varepsilon_r - 1)\left[2 < D'^2 > + (\varepsilon_r - 1) < D'^4 > + \frac{1}{k_0^2} < D''^2 >\right] << 1 \qquad (4.22)$$

In the TE-polarization case, there are two error criteria that are independent and the surface profile has to satisfy both error criteria to insure accuracy. All elements in (4.18) and (4.22) are positive real values. Hence, summing both inequalities yields a single error criterion which takes the form for the TE polarization case:

$$Q_{TE}(D',D'') = \frac{\varepsilon_r - 1}{\varepsilon_r}\left[6 < D'^2 > + (3 + \varepsilon_r) < D'^4 > + \frac{3}{k_0^2} < D''^2 >\right] << 1 \qquad (4.23)$$

This error criterion is somewhat strict because of the approximations used in (4.20) and (4.21), but it can be used to check the accuracy of the solution obtained.

A TM-error criterion is obtained by using (4.14a), which is written as

$$\left\langle \left|M_{ya}^{g1}\right|^2 \right\rangle << (k_0\eta_0)^2 \left\langle \left|H_{ya}^{g2}\right|^2 \right\rangle, \text{ for mode group-1} \qquad (4.24)$$

$$\left\langle \left|M_{ya}^{g2}\right|^2 \right\rangle << (k_0\eta_0)^2 \left\langle \left|H_{ya}^{g2}\right|^2 \right\rangle, \text{ for mode group-2} \qquad (4.25)$$

Substituting (3.9)-(3.11) into (4.16) and again assuming that $\langle D' \rangle = \langle D'^3 \rangle = \langle D'' \rangle = 0$ yields the error criterion for each mode group as follows

$$Q_{TM}^{g1}(D',D'') = 4\left[< D'^2 > + < D'^4 > + \frac{1}{2k_0^2} < D''^2 >\right] << 1 \qquad (4.26)$$

and

$$Q_{TM}^{g2}(D',D'') = (\varepsilon_r - 1)\left[2 < D'^2 > + (\varepsilon_r - 1) < D'^4 > + \frac{1}{k_0^2} < D''^2 >\right] << 1 \qquad (4.27)$$

These are identical to the TE- error criteria in (4.18) and (4.22), respectively. The TM-error criterion, therefore, is written as (4.23). Hence, the error criterion of the fictitious current solution for both polarizations is

$$Q(D',D'') = \frac{\varepsilon_r - 1}{\varepsilon_r}\left[6 < D'^2 > +(3+\varepsilon_r) < D'^4 > + \frac{3}{k_0^2} < D''^2 >\right] << 1 \qquad (4.28)$$

which is independent of the polarization of fields, but depends on the permittivity of the dielectric half-space whose surface is rough.

The error criterion (4.28) is applied to a deterministic rough surfaces with defined roughness profile $D(z)$. But, because natural surfaces are randomly rough, it is important to study scattering from random rough surfaces. This requires using an appropriate statistical description for the surface parameters. The most commonly used statistical description of random rough surfaces assumes that both the height and slope of the random surfaces are characterized by a Gaussian probability density function (pdf). Using this statistical description of the surface parameters, each term in the error criterion (4.28) is expressed in terms of statistical parameters. In the present discussion, an error criterion for a Gaussian random surface will be obtained (a comprehensive discussion of Gaussian surface profiles and the generation of such surfaces will be addressed in Section 5.1.1).

Let D be a Gaussian surface height distribution with $\langle D \rangle = \langle D' \rangle = \langle D'' \rangle = 0$ then

$$\langle D^2 \rangle = \sigma^2 \qquad (4.29)$$

where σ is standard deviation of the random variable D, always a positive value, which is defined as

$$\sigma = \sqrt{\left\langle (D - < D >)^2 \right\rangle} \tag{4.30}$$

Consequently, if standard deviations of D' and D'' are denoted by $\sigma_{D'}$ and $\sigma_{D''}$, respectively, then

$$\left\langle D'^2 \right\rangle = \sigma_{D'}^2 \tag{4.31a}$$

$$\left\langle D''^2 \right\rangle = \sigma_{D''}^2 \tag{4.31b}$$

To determine the average of higher-order derivatives of the surface profile, namely, $\left\langle D'^2 \right\rangle$ and $\left\langle D''^2 \right\rangle$, it is necessary to examine higher-order correlations, i.e. correlation between higher order derivatives of a one-dimensional surface profile, which satisfying the relationships [14][9]:

$$\left\langle \frac{d^p D(z_0)}{dz_0{}^p} \frac{d^q D(z)}{dz^q} \right\rangle = (-1)^p \sigma^2 \frac{d^{p+q} C(z_0 - z)}{dz^{p+q}} \tag{4.32}$$

where $C(z_0 - z)$ is the surface height correlation function which is Gaussian and given by

$$C(Z) = \exp\left(-\frac{Z^2}{l^2} \right) \text{ where } Z = | z_0 - z | \tag{4.33}$$

Equation (4.32) can be used to determine averages of higher-order surface derivatives. This is done by considering the limit as $z_0 \to z$ so that (4.32) reduces to

$$\left\langle \left(\frac{d^i D(z)}{dz^i} \right)^2 \right\rangle = \sigma^2 \left. \frac{d^{2i} C(z_0 - z)}{dz^{2i}} \right|_{z_0 = z} \tag{4.34}$$

which also shows whether differentiability of the correlation function for higher-order surface correlations exist. Substituting (4.33) into (4.34) with i=1 yields

$$\langle D'^2 \rangle = \frac{2\sigma^2}{l^2} \tag{4.35}$$

and similarly,

$$\langle D''^2 \rangle = \frac{12\sigma^2}{l^4} \tag{4.36}$$

where l is the correlation length (which will be described in Section 5.1.1). To determine $\langle D'^4 \rangle$ in (4.28), the moment theorem is used, which states that [15]

$$\langle D'^n \rangle = \frac{1}{j^n} \frac{d^n}{d\omega^n} \Phi_{D'}(\omega) \tag{4.37}$$

where $\Phi_{D'}(\omega)$ is the characteristic function of D'. The surface derivatives are also Gaussian. Therefore $\Phi_{D'}(\omega)$ is

$$\Phi_{D'}(\omega) = \exp\left(-\sigma_{D'}^2 \omega^2 / 2\right) \tag{4.38}$$

Using (4.31a), (4.35), (4.37) and (4.38) yields

$$\langle D'^4 \rangle = 3\sigma_{D'}^4 = 3\left(\frac{2\sigma^2}{l^2}\right)^2 = 12\frac{\sigma^4}{l^4} \tag{4.39}$$

Substituting (4.35)-(4.36) and (4.39) into (4.28) yields the error criterion for random surface with Gaussian pdf:

$$Q(\sigma, l) = 12\frac{\varepsilon_r - 1}{\varepsilon_r}\left[\frac{\sigma^2}{l^2} + (3+\varepsilon_r)\frac{\sigma^4}{l^4} + \frac{3}{k_0^2}\frac{\sigma^2}{l^4}\right] << 1 \tag{4.40}$$

This result is applied to ascertain the accuracy of FC-solutions.

4.3 Reduction to the Scatter Pattern of a Perfect Electric Conductor (PEC)

Another useful check is to verify that the scatter pattern of a rough dielectric surface reduces to the scatter pattern of a rough perfectly conducting surface $R_c(\phi,\phi_0)$ that was derived in [10]. The comparison is performed only for upper half-space since fields do not exist inside a PEC. This is accomplished by replacing ε_r in (2.36) by $-j\infty$ for TE-polarization. It can be shown that

$$\lim_{\varepsilon_r \to -j\infty} [R_{11}^{TE}(\phi,\phi_0)] = \left[\frac{1}{2\pi}\right]\left[\frac{2u_0 u}{(u_0+u)}\right]\int_{-L}^{L}\left\{1-[1+D_1'^2]e^{j(u_0+u)D_1}\right\}e^{-j(\beta_0-\beta)z_1}dz_1 \qquad (4.41)$$

This result is identical to the plane wave scatter pattern of a rough PEC, $R_c(\phi,\phi_0)$, given in [10], i.e.,

$$\lim_{\varepsilon_r \to -j\infty} [R_{11}^{TE}(\phi,\phi_0)] = R_c^{TE}(\phi,\phi_0) \qquad (4.42)$$

For the TM- polarization case, it can be shown by replacing ε_r in (3.38) by $-j\infty$ that:

$$\lim_{\varepsilon_r \to -j\infty} [R_{11}^{TE,TM}(\phi,\phi_0)] = R_c^{TE,TM}(\phi,\phi_0) \qquad (4.43)$$

where ϕ and ϕ_0 are defined over the ranges $-\pi/2 \le \phi \le \pi/2$, $-\pi/2 \le \phi_0 \le \pi/2$ since the fields are zero in the lower half-space occupied by the perfect conductor.

CHAPTER 5

NUMERICAL RESULTS

To verify the validity of the fictitious current method (FCM), numerical comparisons are made with data generated by the Method of Moments (MoM), one of the best-known numerical techniques used to solve scattering problems with highly accurate results. Most numerical methods for the evaluation of scattering from natural rough surfaces are based on the MoM [16]. Scattering coefficients are obtained for two kinds of surfaces. The first coefficient is obtained for random rough surfaces with Gaussian statistics. The second is obtained for a deterministic surface, which is assumed to be sinusoidally varying. Even though random rough surfaces are more general in describing the surfaces found in nature, deterministic surfaces yield valuable results and are useful in device characterization such as scattering by dielectric gratings.

5.1 Scattering Coefficient for Random Surfaces

5.1.1 Random Surface Profiles

A random surface must be generated with the appropriate statistics that can be controlled. A statistical random surface is usually described in terms of its deviation from a reference plane, beyond the rough surface region. Random surfaces are characterized by their surface height distribution functions and surface correlation functions. The Gaussian (normal) probability density function (pdf) is chosen to generate rough surfaces since much of the literature on rough surfaces assumes the surface height distributions are Gaussian.

A surface is represented by the function $D(z)$ described by a Gaussian height distribution, $P(D)$. For convenience, the average height of the random surface is assumed to be zero, i.e.,

$$< D >= \int_{-\infty}^{+\infty} DP(D)dD = 0 \tag{5.1a}$$

where the Gaussian pdf is given by

$$P(D) = \frac{1}{\sigma\sqrt{2\pi}} \exp(-\frac{D^2}{2\sigma^2}) \tag{5.1b}$$

in which σ^2 denotes the variance of D. The variance of a random variable is defined as the mean-squared variation $< \Delta^2 >$, where $\Delta = D - < D >$ [15]. Using the condition (5.1a), standard deviation (σ) can be expressed as

$$\sigma = \sqrt{< D^2 >} \tag{5.2}$$

since $\sigma^2 =< \Delta^2 >=< (D - < D >)^2 >=< D^2 > - < D >^2 =< D^2 >$. This means that root mean square (RMS) height of the surface is equal to the standard deviation for Gaussian distribution with mean zero.

The second characterization of a random surface is its surface correlation. Even surfaces that have the same height distributions and the same RMS heights may be very different because of the different 'length scale' over which height changes along the surface [9]. Figure 5.1 shows that the correlation length can affect the surface profile. Both samples have the same RMS height 0.5λ but have different correlation lengths, 0.5λ for the first sample and 2λ for the second one. This implies that the correlation length can controls the rate of change of the surface heights along the z-plane via the correlation function, which is defined as

$$C(\boldsymbol{Z}) = \frac{< D(z)D(z+\boldsymbol{Z}) >}{\sigma^2} \tag{5.3a}$$

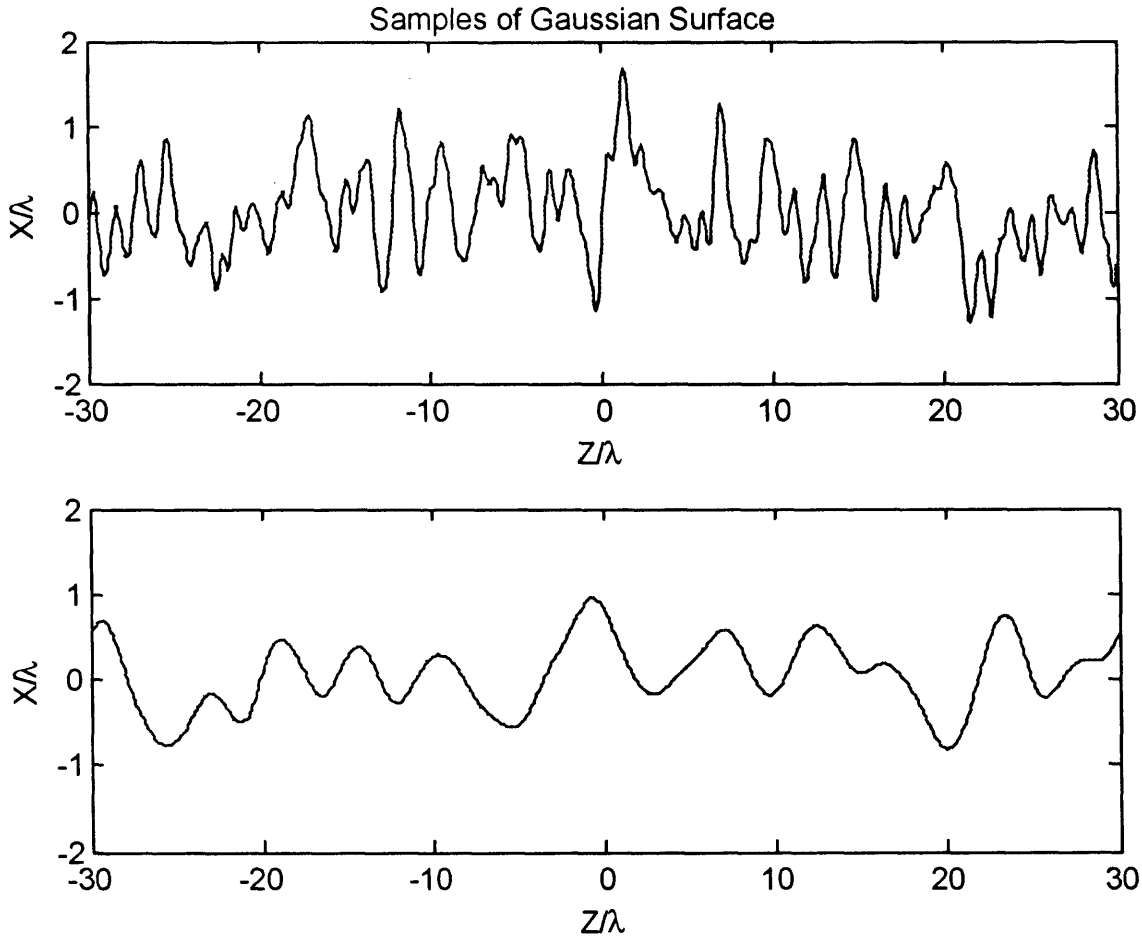

Figure 5.1 Gaussian surfaces of the same RMS height but different correlation lengths.

For this illustration, surface correlation is Gaussian, given by [17]

$$C(\mathbf{Z}) = \exp\left(-\frac{\mathbf{Z}^2}{l^2}\right) \tag{5.3b}$$

where l is usually called the correlation length which is the distance that the correlation function falls by $1/e$. If the surface is isotropic, the vector $\boldsymbol{Z}$ can be changed to scalar Z, i.e., the correlation function is independent of direction along the z axis.

The other parameter used to specify randomly rough surface is the RMS gradient, that is found from the RMS height and correlation length. This is called the RMS slope angle γ; using the relation in (4.35), it is defined as

$$\tan\gamma = \sqrt{<\frac{dD}{dz}>} = \frac{\sigma\sqrt{2}}{l} \tag{5.4}$$

The Gaussian random surface can be generated using several methods such as the moving average, autoregressive method and the spectral method. The numerically efficient method is the spectral method so that is the one used in the present work.

Let a surface sample be generated for $-L \le z \le L$, and let D_n be represented by the Fourier series

$$D_n = \frac{1}{2L}\sum_{i=-N/2+1}^{N/2} F(K_i)e^{jK_i z_n} \tag{5.5}$$

where $z_n = n\Delta z$ and $D_n = D(z_n)$ with $2L = N\Delta z$. The surface spatial wave number is $K_i = (2\pi i)/(2L)$. If the coefficient $F(K_i)$ is chosen using the relation [17]

$$F(K_i) = \sqrt{4\pi L p(K_i)}X_\xi, \qquad i \ge 0 \tag{5.6a}$$

for $i \le 0$, $F(K_i) = F^*(K_{-i})$ which makes D_n real and X_ξ is an uncorrelated random process. The Gaussian power spectrum is taken as

$$P(K_i) = \frac{l\sigma^2}{2\sqrt{\pi}}\exp(-\frac{K_i^2 l^2}{4}) \tag{5.6b}$$

For the case under consideration, $F(K_i)$ is chosen to be

$$F(K_i)=\begin{cases}\sqrt{4\pi Lp(K_0)}G_\alpha, & i=0\\ \sqrt{4\pi Lp(K_{+N/2})}G_\beta, & i=N/2\\ \sqrt{4\pi Lp(K_i)}\left[(G_s+jG_t)/\sqrt{2}\right] & i\neq 0,\ N/2\end{cases} \tag{5.7}$$

where s,t are distinct indices of 1,2,...,N/2 and α,β are chosen to be one of the values of numbers 1,2,...,N/2 such that $\alpha\neq\beta$. Each of the G represents one of N Gaussian random numbers generated by using the MATLAB function with zero mean and unit variance.

Now (5.5) can be performed efficiently using an inverse fast Fourier transform (IFFT). The surface height profile is written as

$$D_n=\frac{e^{-j(n-1)\pi}}{\Delta z}IFFT[Q_m] \tag{5.8}$$

where

$$Q_m=F(K_m)e^{j\frac{2\pi}{N}m},\quad m=1,2,\ldots,N/2-1 \tag{5.9}$$

Q_m is found using $F(K_m)=F^*(K_{-m})$ for $m=-N/2+1,-N/2+2,\ldots,1$,. The new index is needed instead of m to realize IFFT using the standard MATLAB package. Evaluating the derivative of the rough surface profile, yields the simple expression

$$D'_n=\frac{e^{-j(n-1)\pi}}{\Delta z}IFFT[jK_mQ_m] \tag{5.10}$$

5.1.2 Numerical Comparisons

Several analytical methods have appeared in the literature to study scattering from rough surfaces. The two classical approaches are the Kirchhoff method and the small perturbation method. Each method is valid over a range of surface parameters, and may not overlap one another. Verification of these methods is often done by comparison to numerical results. The Method of Moments (MoM) is a numerical technique that has been used extensively in the solution of electromagnetic boundary value and scattering problems. The MoM has been widely used to determine fields scattered by metallic objects in antenna and radar applications, but its use in the evaluation of scattered fields by rough dielectric surfaces is not so widespread and is more recent [18]. The MoM is summarized in Appendix B. The FC- method presented here is compared to numerical results generated by use of the MoM.

To determine the average scattering coefficient, the Monte Carlo technique is used. The Monte Carlo method is a simulation model to generate values for indeterminate variables over and over again. To apply this technique, one discrete random surface profile D_n is generated as described in Section 5.1.1 and is used for D in (2.35 with 2.36) and (3.37 with 3.38) for TE and TM polarization, respectively. The scattered field using the MoM is obtained by evaluating (B.5) and (B.7) for the same surface profile in the FCM. A second surface is then generated and the scattered fields are obtained. In this procedure, scattered fields are obtained repeatedly using N_T surface realizations. Note that N_T surfaces have the same RMS height (σ) and correlation length (l).

The first-order field is calculated using the FC- method; this field does not include the reflected field. The scattered field calculated by the MoM equals the total field minus the incident field. In other words, if the original geometry illustrated in Figure 2.1 is considered with an incident plane wave as the excitation, the total field can be written in different ways according to the method used, i.e.,

$$\boldsymbol{E}^t = \boldsymbol{E}^i + \boldsymbol{E}^r + \boldsymbol{E}^s_{FCM} \quad \text{for FCM} \tag{5.11a}$$

$$\boldsymbol{E}^t = \boldsymbol{E}^i + \boldsymbol{E}^s_{MoM} \quad \text{for MoM} \tag{5.11b}$$

where $\boldsymbol{E}^s_{FCM}$ is the first-order scattered field given in (2.35) and $\boldsymbol{E}^s_{MoM}$ is given in (B.5) which includes the reflected field. Therefore, the MoM scattered field needs to be modified in order for a comparison to be made to the scattered field determined from FCM. The field scattered by a flat dielectric surface of length $2L$ centered about the origin, $\boldsymbol{E}^f$ is added to and subtracted from (5.11b) to produce

$$\boldsymbol{E}^t = \boldsymbol{E}^i + \boldsymbol{E}^f + \boldsymbol{E}^s_{MoM} - \boldsymbol{E}^f \tag{5.12}$$

The scattered field $\boldsymbol{E}^s_{MoM}$ can now be written as the sum of two fields, one scattered by the finite rough surface in the region $|z| \leq L$ denoted $\boldsymbol{E}^L$, and one scattered by the flat surface in the region $|z| > L$ denoted $\boldsymbol{E}^\infty$. Thus

$$\boldsymbol{E}^t = \boldsymbol{E}^i + \boldsymbol{E}^f + \boldsymbol{E}^\infty + \boldsymbol{E}^L - \boldsymbol{E}^f \tag{5.13}$$

Note that $\boldsymbol{E}^f + \boldsymbol{E}^\infty$ is the specularly reflected field from an infinite flat surface which is designated $\boldsymbol{E}^r$ in (5.11a); thus (5.13) reduces to

$$\boldsymbol{E}^t = \boldsymbol{E}^i + \boldsymbol{E}^r + \boldsymbol{E}^L - \boldsymbol{E}^f \tag{5.14}$$

Comparing (5.14) with (5.11a) shows that a scattered field E^{sM}_{MoM} in MoM equals the total field minus the incident and specularly reflected field, i.e.,

$$E^{sM}_{MoM} = E^t - E^i - E^r = E^L - E^f\Big|_{MoM} \tag{5.15}$$

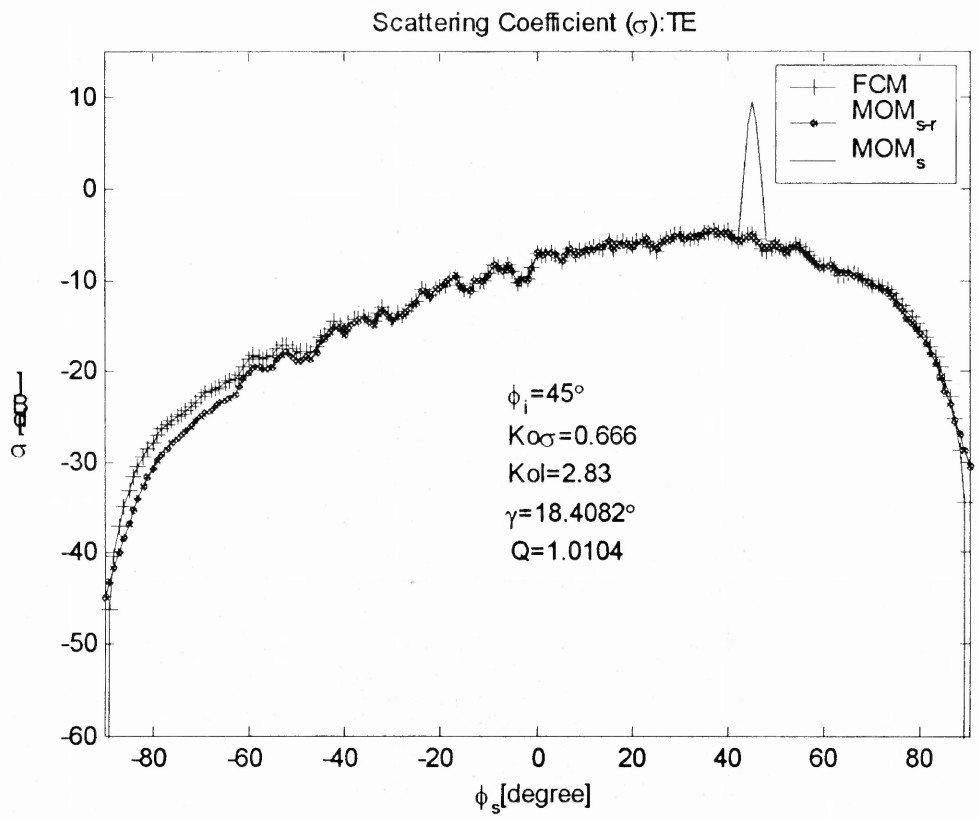

Figure 5.2 Scattering patterns MOM_s and MOM_{s-r} obtained from E^s_{MoM} and E^{sM}_{MoM}, respectively. The surface profile is the same as in Figure 5.5. The large peak in the MOM_s result in the specular direction is due to the reflected field, which is removed from the MOM_{s-r}.

The scattered field E^L is given in (B.5) with integration range $|z| \leq L$ and the scattered field E^f is obtained by setting $D(z)$=0 in (B.5). Figure 5.2 is a sample plot, which shows both E^s_{MoM} and E^{sM}_{MoM} defined in (5.11a) and (5.15), respectively. The appearance of the peak around the specular direction in the MoM result occurs because the MoM solution

includes the reflected field whereas the FC solution does not include the reflected field. For a more accurate comparison, all MoM simulation results in Figures 5.3 to 5.7 are obtained by plotting the modified scattered field, i.e., E_{MoM}^{sM} as denoted in (5.15). Good agreement is then more clearly observed.

In numerical simulations using MoM, the rough surface is truncated at $z = \pm L$. This produces current over-flow at the edge of the rough surface, called the edge effect, which has to be minimized. To reduce the error introduced by this effect, the incident wave is tapered so that the surface currents are small at the edge. The tapered incident plane wave is structured to decay to zero in a Gaussian manner for large z.

All the Monte Carlo data is generated for N=720 with $2L$=60λ, i.e., $\Delta z = 2L/N$. The results did not change when simulations were performed for N=1000 and 1440 with $2L$=60λ, 80λ and 120λ. The incoherent scattering coefficient is obtained after repeating the same process for N_T surface realizations as [19]

$$\sigma = \frac{2\pi\rho}{N_T L_{eff}} \left[\sum_{i=1}^{N_T} |E_y^s|^2 - \frac{1}{N_T} |\sum_{i=1}^{N_T} E_y^s|^2 \right] \tag{5.11}$$

where the effective illuminating length (L_{eff}) is $(g\sqrt{\pi/2})/\cos\phi_i$ for tapered incident plane wave with the Gaussian weighting function having the form $G(z) = \exp[-(z\cos\phi_i / g)^2]$. The tapering constant (g) is usually chosen to be somewhere between $L/2$ to $L/5$ depending on the incident angle. Fifty surface realizations are used for Monte Carlo plots, and the accuracy was checked by increasing this number to 100 with no noticeable change in the results.

Figure 5.3 demonstrates very good agreement between the FCM and the MoM results for both TE- and TM- polarization. The scattering angle ϕ_s is taken at 180 descrete values ranging from –90° to 90° in 1° increments. The incident angle ϕ_i is fixed to 45°. All surface profiles are described in the figure. The error criterion Q for the surface is obtained by usuing (4.40) and has a small value. The surface profile of Figure 5.4 has higher Q value than Figure 5.3 but still satisfies the criterion and the curves in both polarization show good agreement as expected. Figure 5.5 shows the results from the two method under consideration for an increased RMS slope angle γ and for Q=1, which is the same surface profile shown in Figure 5.2. There is small disagreement to MoM over the range $-90^\circ \le \phi_s \le -50^\circ$ in TE-polarization case. Figure 5.6 presents curves for a surface having a very high RMS slope and for Q that is close to 4. Figure 5.5 and 5.6 show that even when the error criterion is not small compared to unity, good results are obtained. Figure 5.7 shows that the scattering coefficients can be very different for surfaces that have the same RMS slope but different RMS height and correlation length. The surface for Figure 5.7 has a very high RMS height, but the scattering pattern indicates that the surface is smooth because the correlation length is larger in Figure 5.7 as compared to the correlation length in Figure 5.4.

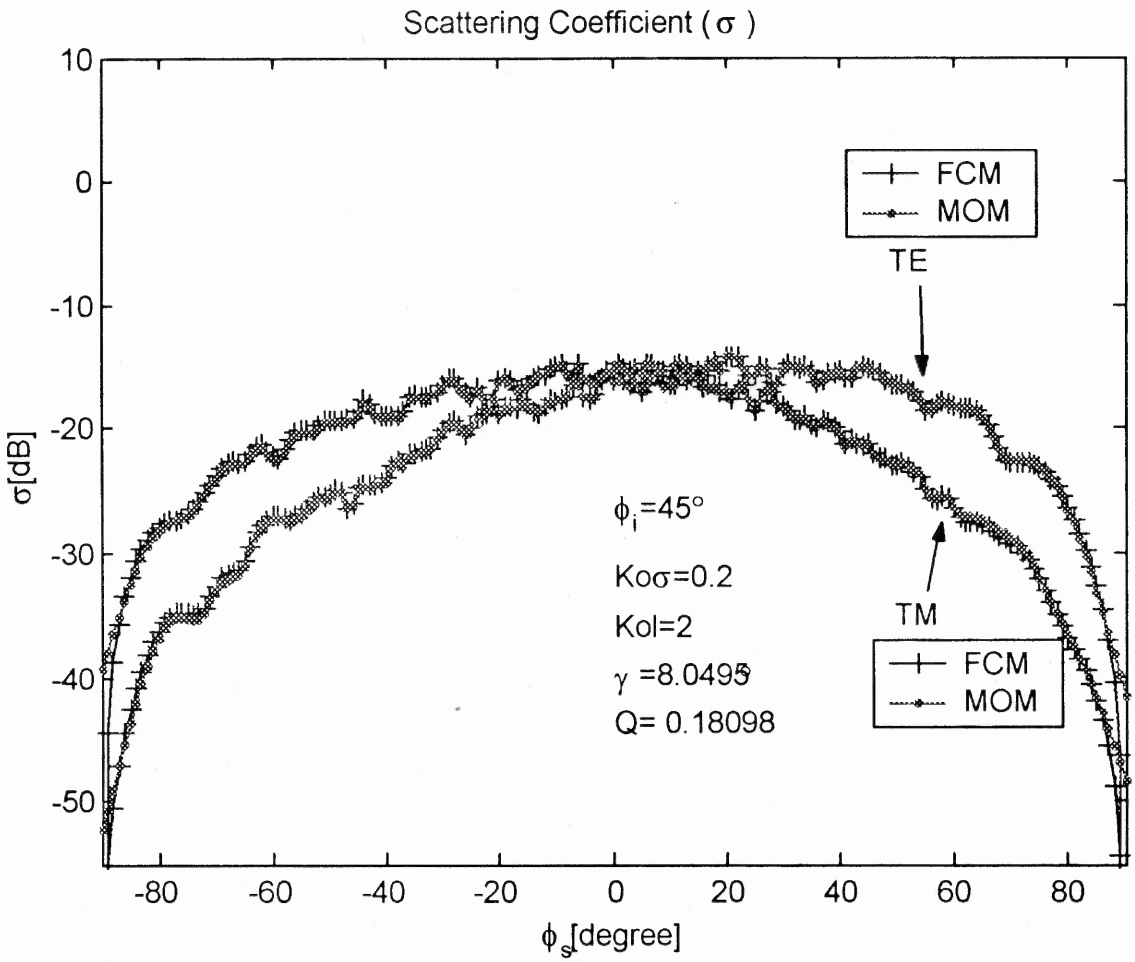

Figure 5.3 Comparisons of Scattering Coefficients for FCM vs. MoM.
$\phi_i = 45^o$, $k_0\sigma = 0.333$, $k_0 l = 2.83$, $\gamma = 9.45^o$, $g = L/2$, where ϕ_i is the angle of incidence, σ is RMS surface height, l is the surface correlation length, γ is the RMS surface slope angle, ϕ_s is scattering angle and Q is error criterion of the given surface profile, both TE- and TM- Polarizations.

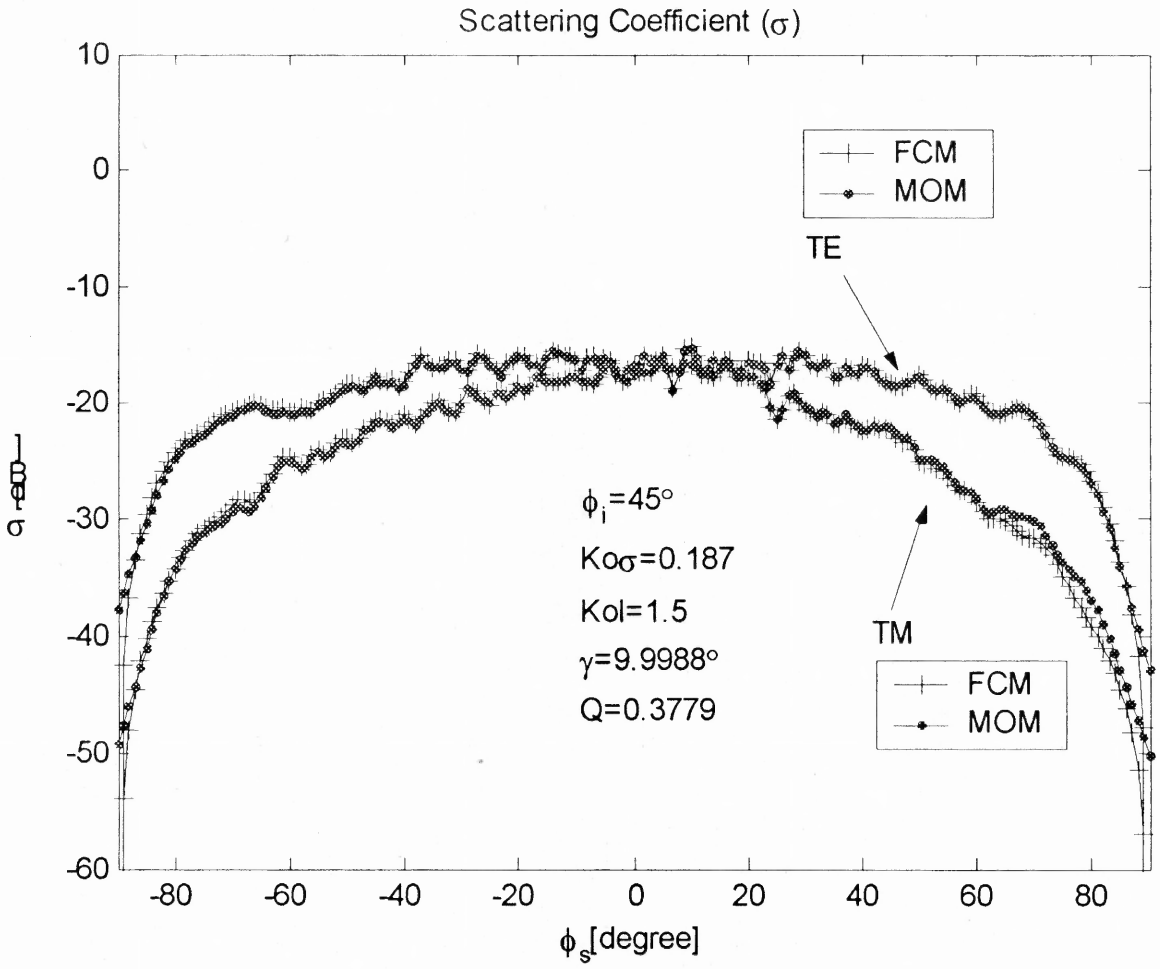

Figure 5.4 Comparisons of Scattering Coefficients for FCM vs. MoM.
ϕ_i is the angle of incidence, σ is RMS surface height, l is the surface correlation length, γ is the RMS surface slope angle, ϕ_s is scattering angle and Q is error criterion of the given surface profile, both TE- and TM- Polarizations.

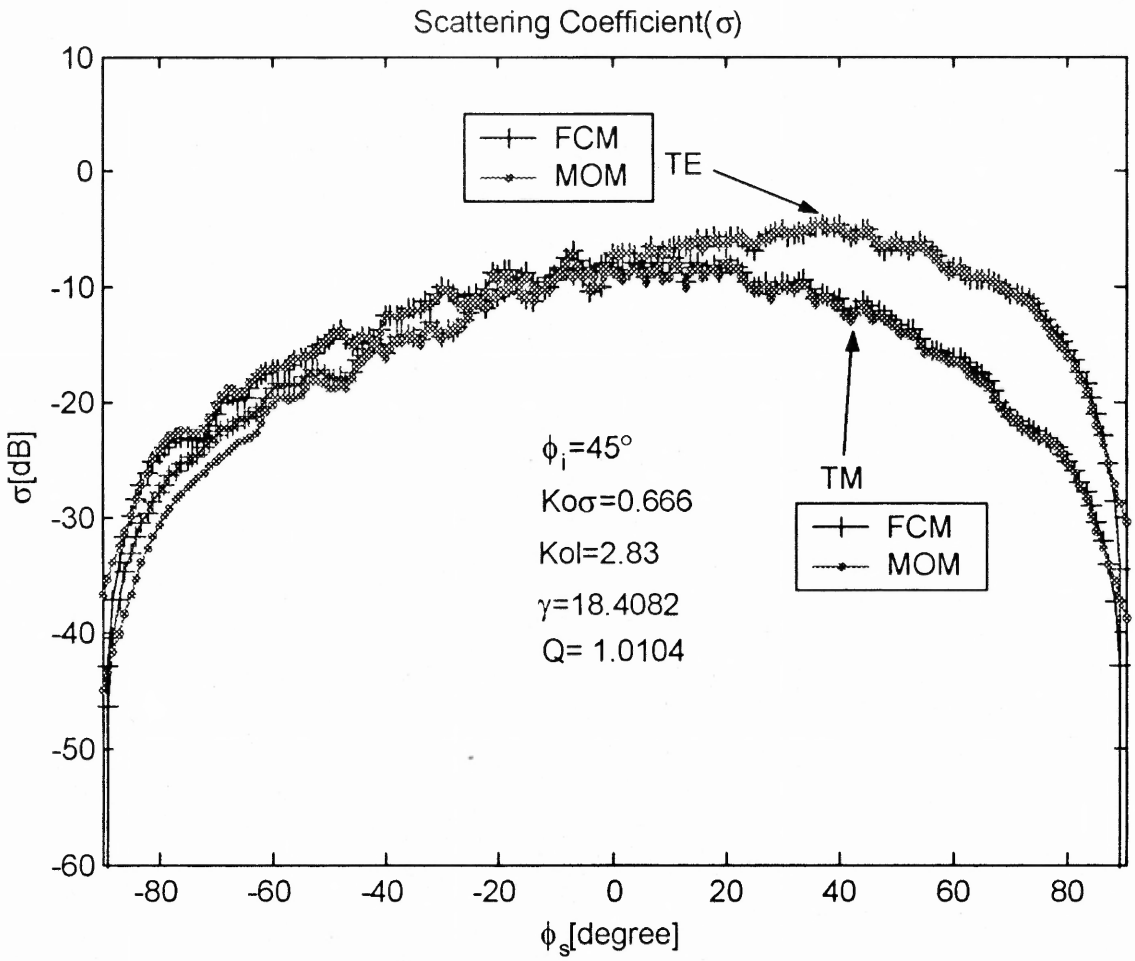

Figure 5.5 Comparisons of Scattering Coefficients for FCM vs. MoM.
ϕ_i is the angle of incidence, σ is RMS surface height, l is the surface correlation length, γ is the RMS surface slope angle, ϕ_s is scattering angle and Q is error criterion of the given surface profile, both TE- and TM- Polarizations.

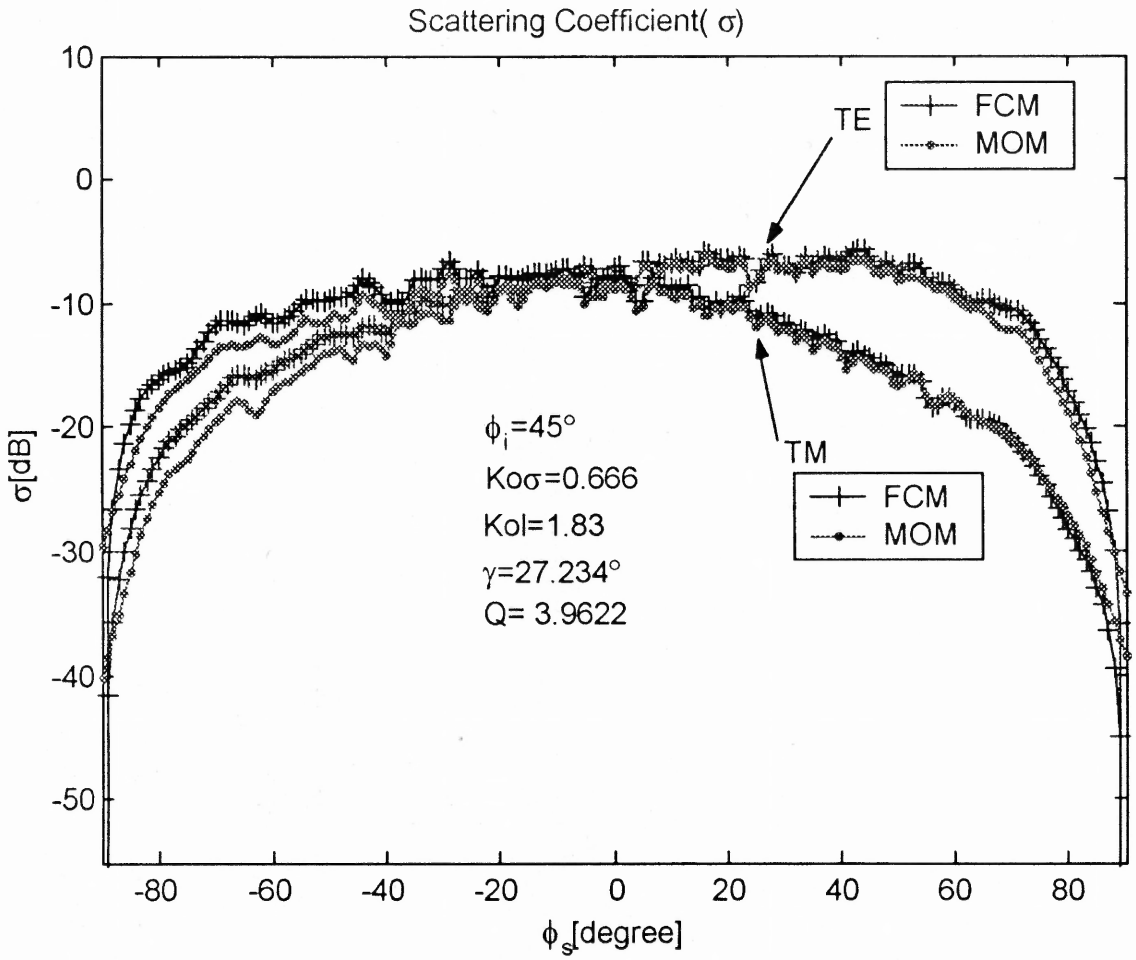

Figure 5.6 Comparisons of Scattering Coefficients for FCM vs. MoM.
ϕ_i is the angle of incidence, σ is RMS surface height, l is the surface correlation length, γ is the RMS surface slope angle, ϕ_s is scattering angle and Q is error criterion of the given surface profile, both TE- and TM- Polarizations.

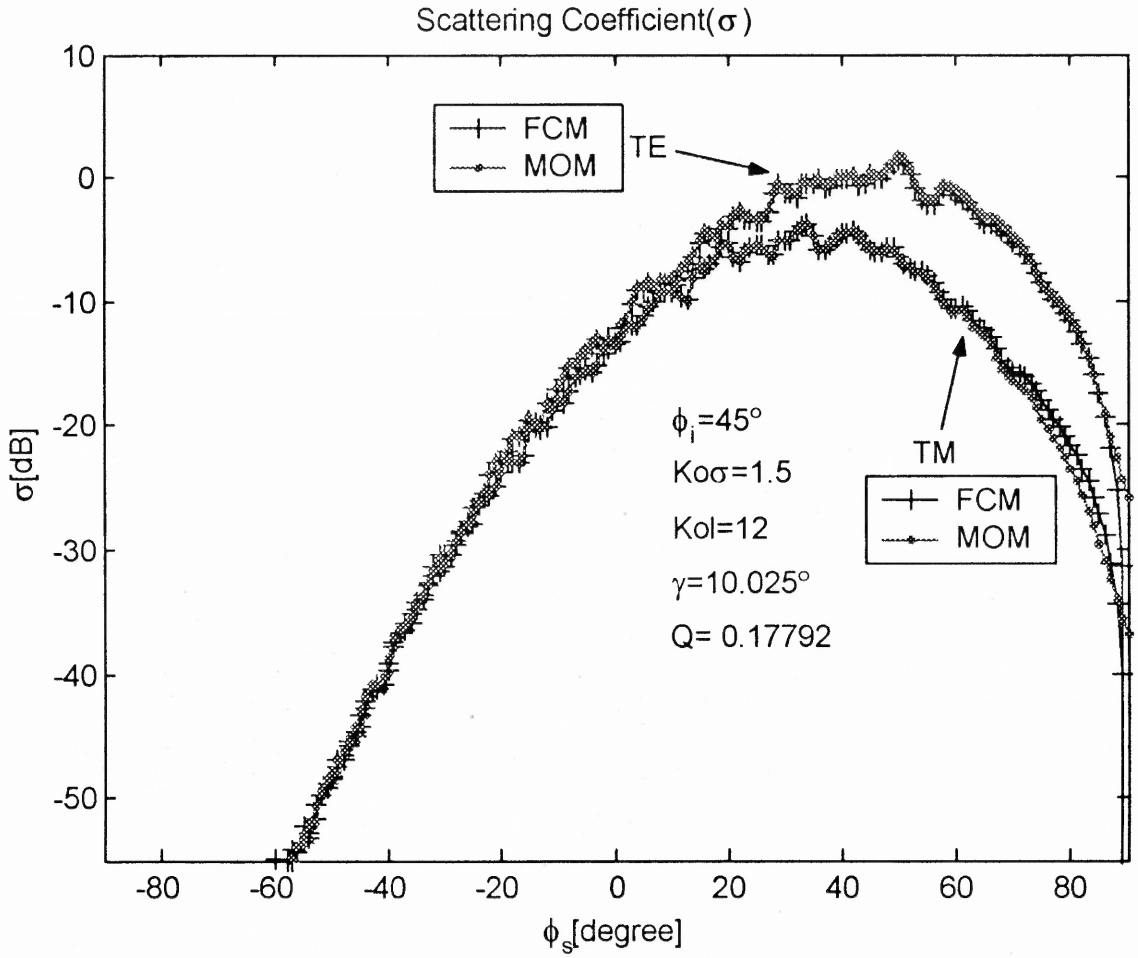

Figure 5.7 Comparisons of Scattering Coefficients for FCM vs. MoM.
ϕ_i is the angle of incidence, σ is RMS surface height, l is the surface correlation length, γ is the RMS surface slope angle, ϕ_s is scattering angle and Q is error criterion of the given surface profile, both TE- and TM- Polarizations.

5.2 Scattering Coefficient for a Given Deterministic Surface

Numerical results for the scattering coefficient can be obtained not only for a statistical random surface, but also for a deterministic surface. A deterministic surface is one that is defined by an explicit mathematical expression. One of the advantages to studying a deterministic surface is that it is simpler to verify using other methods such as the MoM. In this section, a simple periodic sinusoidal surface is specified and the scattering coefficient is obtained. The scattering coefficients determined using the FCM is compared obtained by use of MoM technique described in Appendix B.

A deterministic rough surface is specified to lie between $z = \pm L$. The surface profile is chosen to satisfy the conditions $D(\pm L)=D'(\pm L)=0$, which was assumed previously to evaluate the integrals in (2.30). Under these assumptions, the deterministic surface chosen is defined by the expression

$$D(z)=\begin{cases} D_0\left[1-\cos^{2K}(N_b\frac{L-|z|}{L}\frac{\pi}{2})\right] & |z|\le L \\ 0 & |z|>L \end{cases} \tag{5.12}$$

where D_0, N_b, K are arbitrary positive real numbers. The surface profile given in (5.12) is periodic with period $N_b/(2L)$ so that N_b is the number of bumps within the length of the rough surface $2L$, and D_0 is the maximum height of the surface. The derivative of $D(z)$ in $|z|\le L$ is calculated to be

$$\frac{dD(z)}{dz}=sD_0(2K)\frac{\pi}{2L}\left[\cos^{2K-1}(N_b\frac{L-|z|}{L}\frac{\pi}{2})\right]\left[\sin(N_b\frac{L-|z|}{L}\frac{\pi}{2})\right] \tag{5.13}$$

where s is defined to be the signum function $sign(z)$ which is +1 for $z>0$, −1 for $z<0$ and 0 if $z=0$, i.e., $s=\left[-sign(z)+sign(-z)\right]/2$. The first-order scattered field is obtained by substituting (5.13) into (2.36) and (3.38) for R^{TE} and R^{TM}, respectively.

Numerical comparisons in this section are performed for a surface profile with 5 bumps. The specified surface profile with N_b=5 and K=1 in (5.12) is then

$$D(z)=D_0\left[1-\cos^2\left(\frac{L-|z|}{L}\cdot\frac{5\pi}{2}\right)\right] \tag{5.14}$$

and the surface derivatives are

$$\frac{dD(z)}{dz}=sD_0\frac{5\pi}{2L}\left[\sin\left(\frac{L-|z|}{L}5\pi\right)\right] \tag{5.15a}$$

$$\frac{d^2D(z)}{dz^2}=2D_0\left(\frac{5\pi}{2L}\right)^2\left[\cos\left(\frac{L-|z|}{L}5\pi\right)\right] \tag{5.15b}$$

The surface specified in (5.14) is illustrated in Figure 5.8.

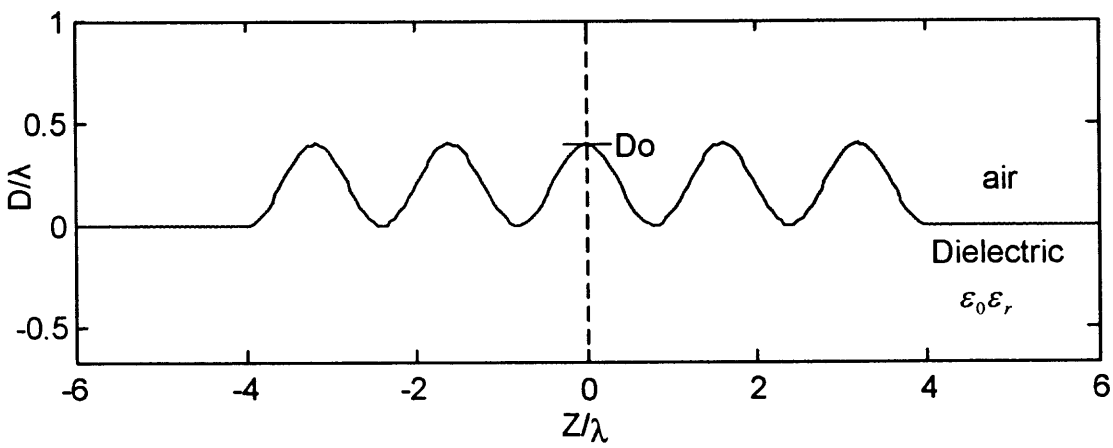

Figure 5.8 Given deterministic surface $D(z)$ described in (5.14).

Spatial resolution (N) in the simulation is set to 230 for $2L=8\lambda$, which is chosen after confirming that no changes occur in the results by increasing for N to 1200 with a dielectric constant of 5.6. The scattering coefficient (σ) is defined as

$$\sigma = \begin{cases} 2\pi\rho \dfrac{\left|E_{ya}^{(1)ff}\right|^2}{\left|E_y^i\right|^2 \lambda} & \text{for TE Polarization} \\ 2\pi\rho \dfrac{\left|H_{ya}^{(1)ff}\right|^2}{\left|H_y^i\right|^2 \lambda} & \text{for TM Polarization} \end{cases} \tag{5.16}$$

where $E_{ya}^{(1)ff}$ and $H_{ya}^{(1)ff}$ are given in (2.35) and (3.37), respectively. Incident fields of both polarizations, E_y^i and H_y^i, are given in (2.3) and (3.2), respectively. The wavelength of the incident wave (λ) is normalized to $1m$ and ρ is the distance from orgin to the observation point. In terms of the scatter pattern (R_{11}) defined in (2.35) and (3.37), the scattering coefficient in (5.16) is rewritten as

$$\sigma = \begin{cases} 2\pi\left|R_{11}^{TE}(\phi_s,\phi_i)\right|^2 & \text{TE Polarization} \\ 2\pi\left|R_{11}^{TM}(\phi_s,\phi_i)\right|^2 & \text{TM Polarization} \end{cases} \tag{5.17}$$

where $R_{11}^{TE}(\phi_s,\phi_i)$ and $R_{11}^{TM}(\phi_s,\phi_i)$ are given in (2.36) and (3.38), respectively. Scattering angle ϕ_s is taken at 180 descrete values ranging from –90° to 90° in 1° increments. The incident angle ϕ_i is fixed at 45°.

All of the plots are obtained for the same surface profile, but with D_o varying from 0.1λ to 0.8λ in 0.1λ increments. All simulation results for the deterministic surface are present in Figures 5.9-5.16. Each figure consists of a set of two polarization cases, TE and TM, for the same surface profile. Changing D_o change the value of Q in (4.28).

Q is evaluated by substituting the surface profile given in (5.14) into (4.28) with expressions for each term given by

$$< D'^2 >= \frac{1}{2}\left(\frac{5\pi}{2L}\right)^2 D_0^2 \tag{5.18a}$$

$$< D'^4 >= \frac{3}{8}\left(\frac{5\pi}{2L}\right)^4 D_0^4 \tag{5.18b}$$

$$< D''^2 >= 2\left(\frac{5\pi}{2L}\right)^4 D_0^2 \tag{5.18c}$$

The above formulas are obtained by using (5.15).

Figure 5.9 and 5.10 show the scattering coefficients for the surfaces defined by (5.14) with D_o=0.1 and 0.2. Both surfaces have small Q values compared to 1 (Q=0.1175 for D_o=0.1λ and Q=0.5173 for D_o=0.2λ). These surfaces satisfy the error criterion given in (4.40). These figures demonstrate excellent agreement in both polarizations between the FCM and MoM. Disagreement around $80° \leq |\phi_s| \leq 90°$ is due to the "edge" effect in the MoM solution due to over-flow currents caused by the truncation of the infinite planar surface. Figure 5.11 to 5.13 show scattering coefficients with bigger heights so that values of Q have values larger than unity, but the curves still show very good agreement over the range $|\phi_s| \leq 70°$. Figures 5.14 to 5.15 for surfaces with very high Q, Q approximately equal to 10, show disagreement between the FCM and MoM for both TE- and TM- Polarization. Figure 5.16 clearly shows a large difference between the FCM and MoM curves. This surface has a very high maximum surface height and a very high Q, namely, 0.8λ and 23.3959, respectively.

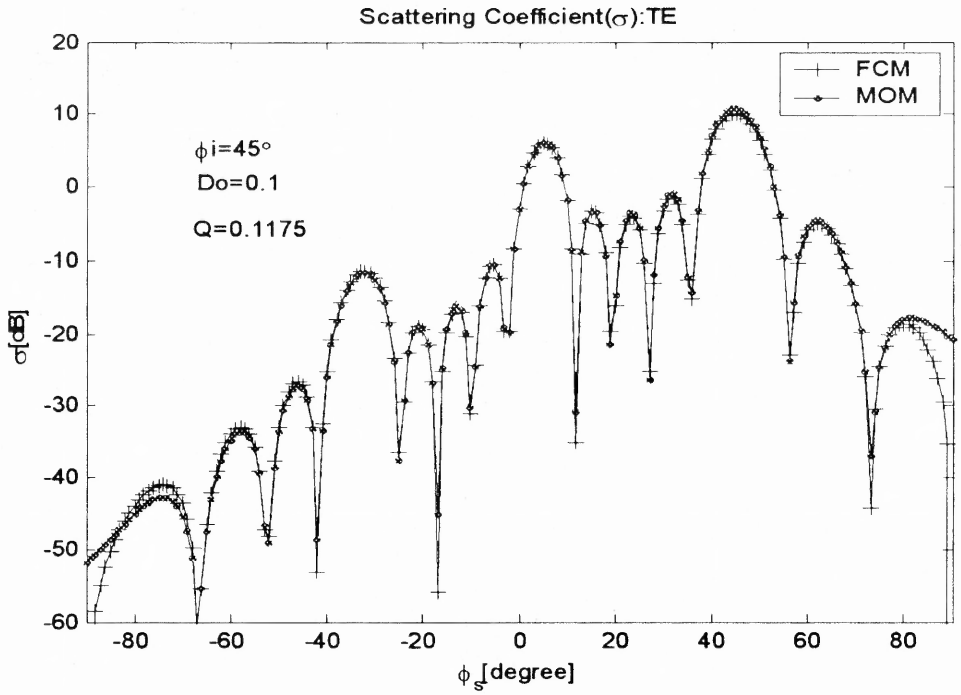

(a)

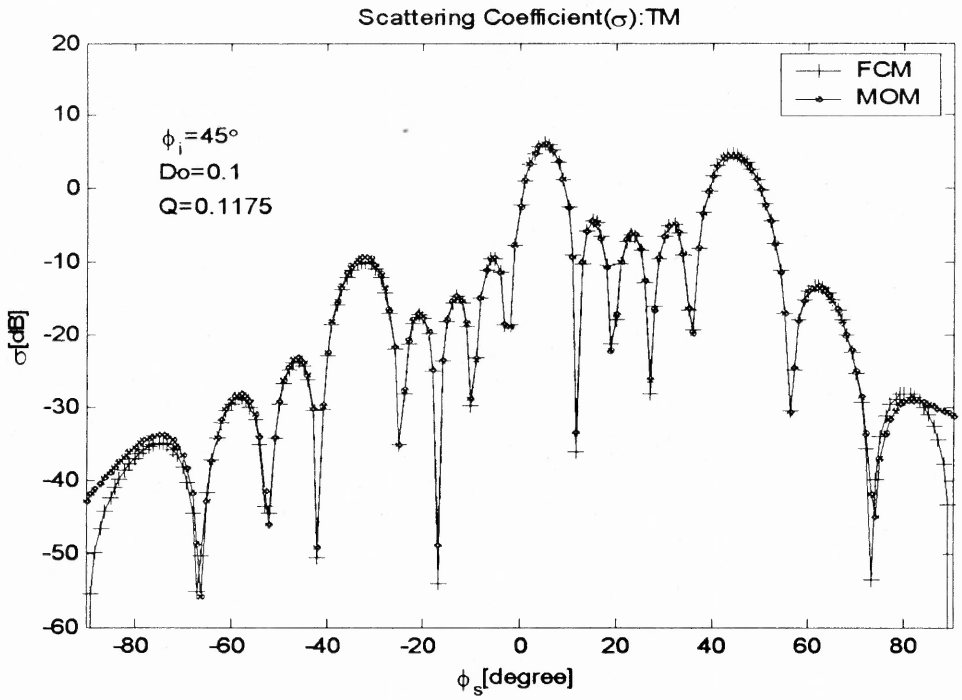

(b)

Figure 5.9 Comparison of scattering coefficients for given deterministic surface. Plots in (a) and (b) are obtained by same surface profile described in (5.14) with D_o=0.1λ. (a) TE polarization (b) TM polarization.

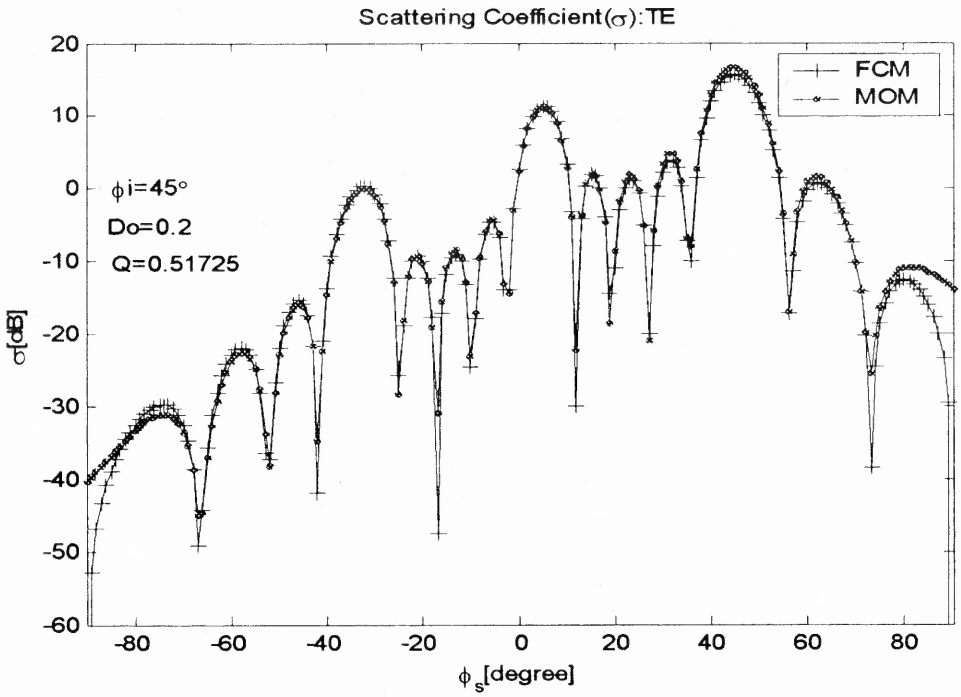

(a)

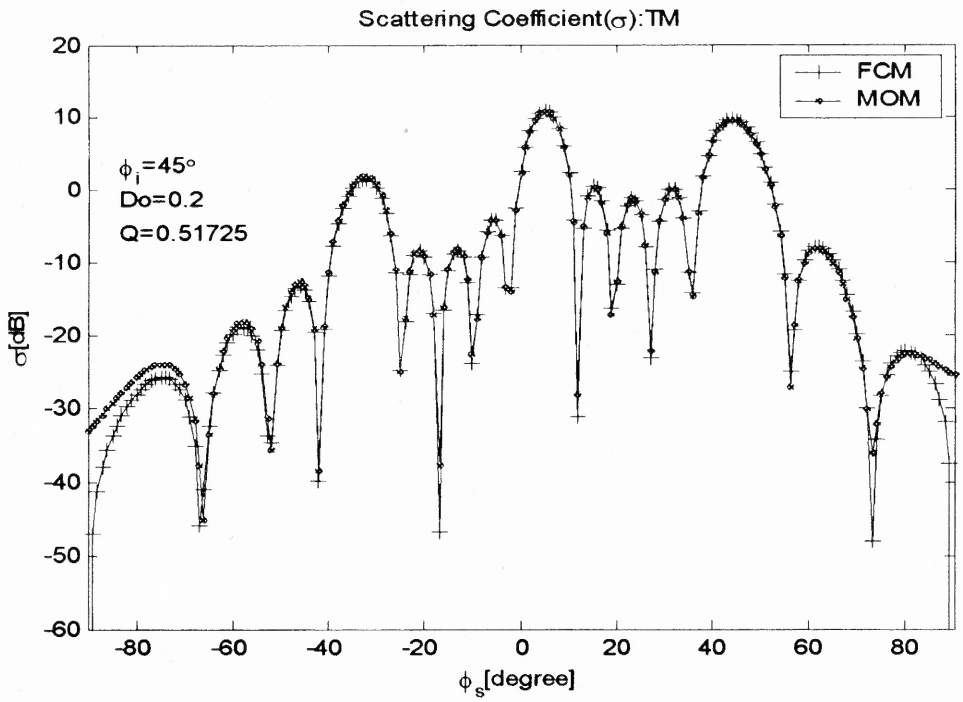

(b)

Figure 5.10 Comparison of scattering coefficients for given deterministic surface. Plots in (a) and (b) are obtained by same surface profile described in (5.14) with D_o=0.2λ. (a) TE polarization (b) TM polarization.

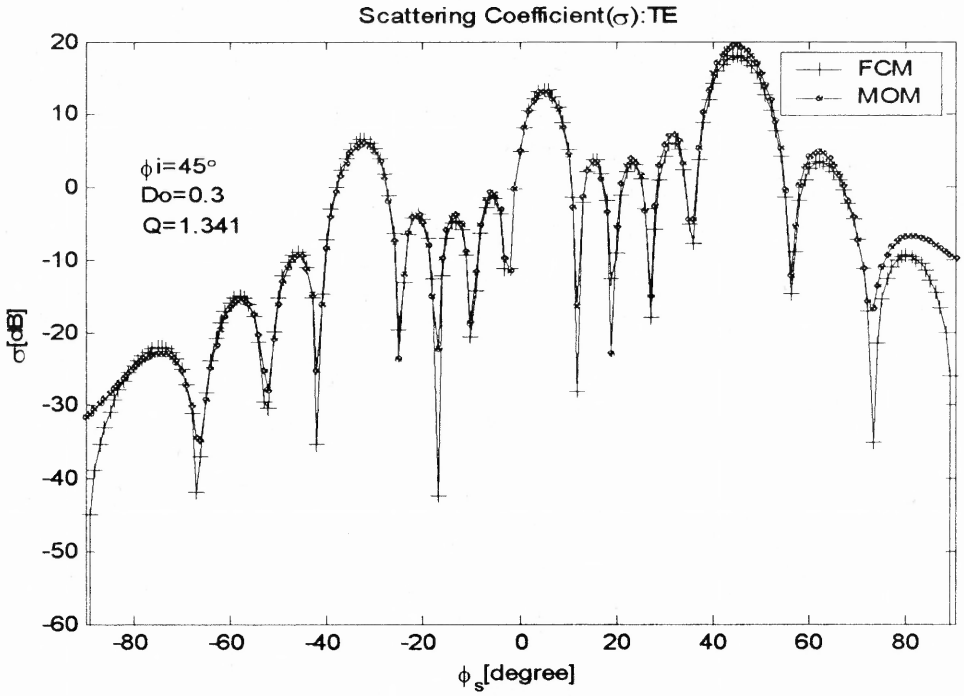

(a)

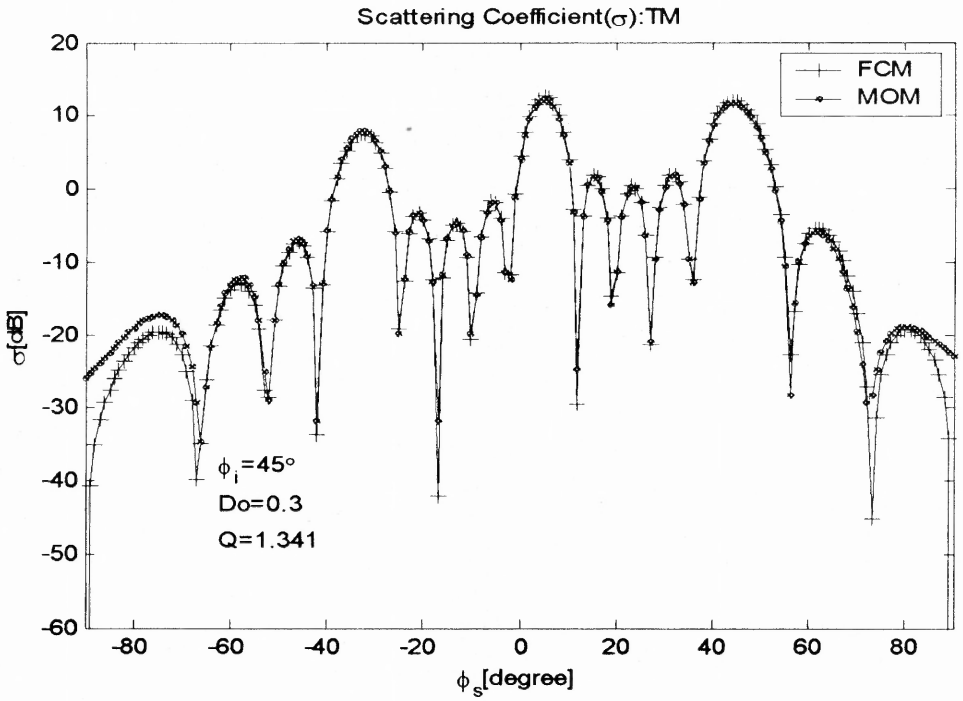

(b)

Figure 5.11 Comparison of scattering coefficients for given deterministic surface. Plots in (a) and (b) are obtained by same surface profile described in (5.14) with D_o=0.3λ. (a) TE polarization (b) TM polarization.

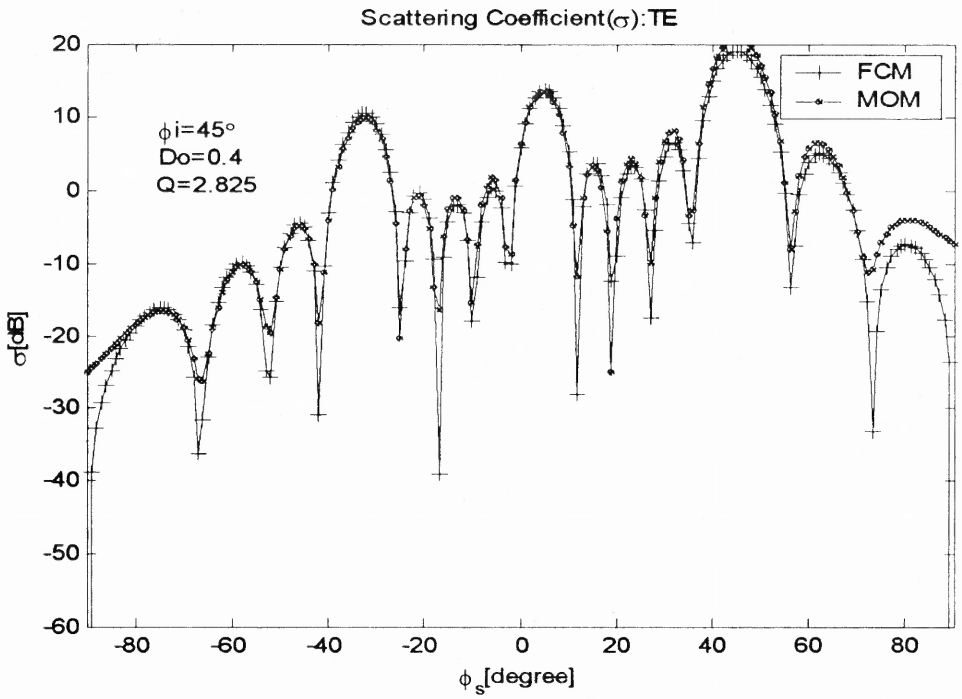

(a)

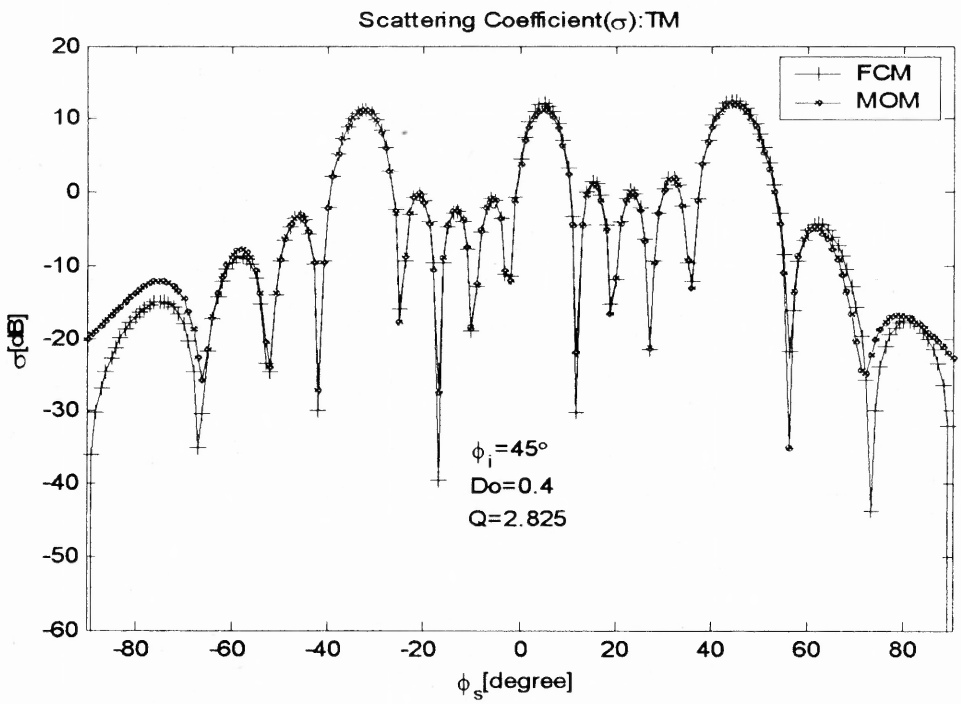

(b)

Figure 5.12 Comparison of scattering coefficients for given deterministic surface. Plots in (a) and (b) are obtained by same surface profile described in (5.14) with D_o=0.4λ. (a) TE polarization (b) TM polarization.

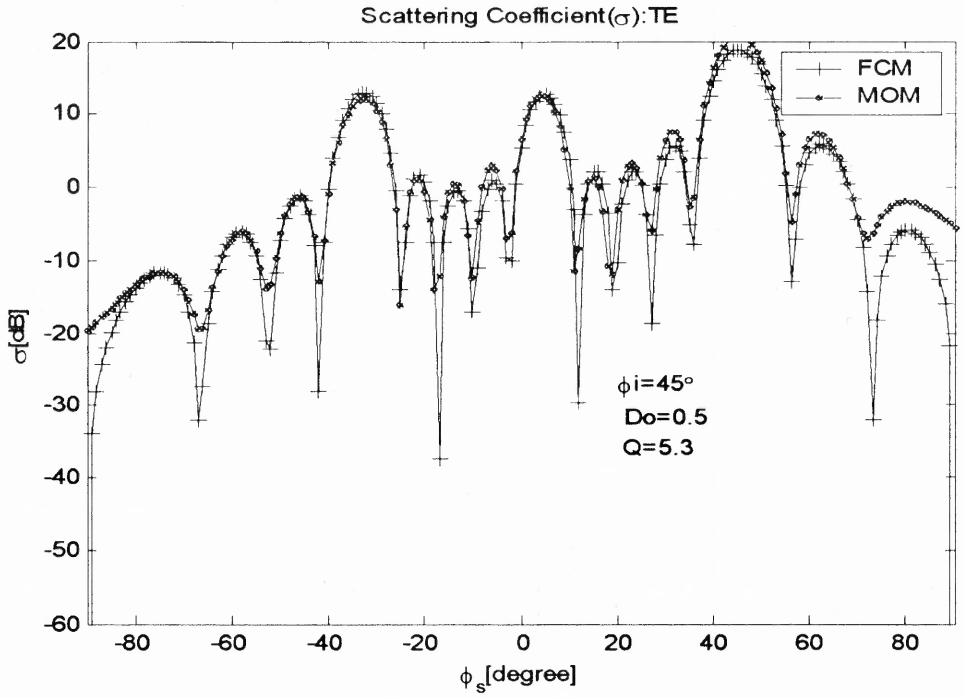

(a)

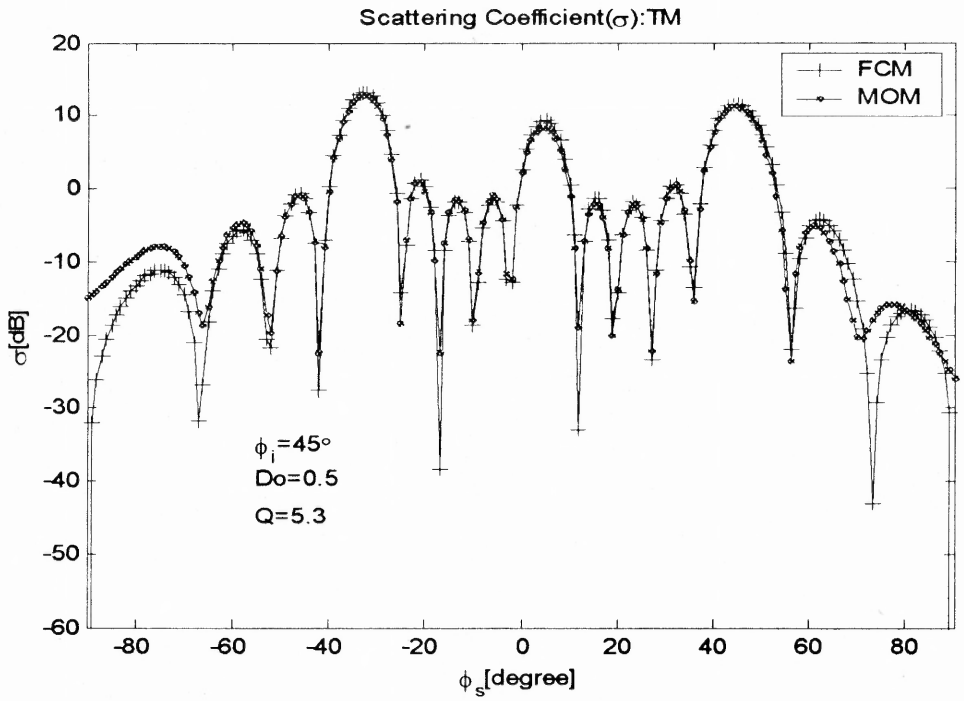

(b)

Figure 5.13 Comparison of scattering coefficients for given deterministic surface. Plots in (a) and (b) are obtained by same surface profile described in (5.14) with D_o=0.5λ. (a) TE polarization (b) TM polarization.

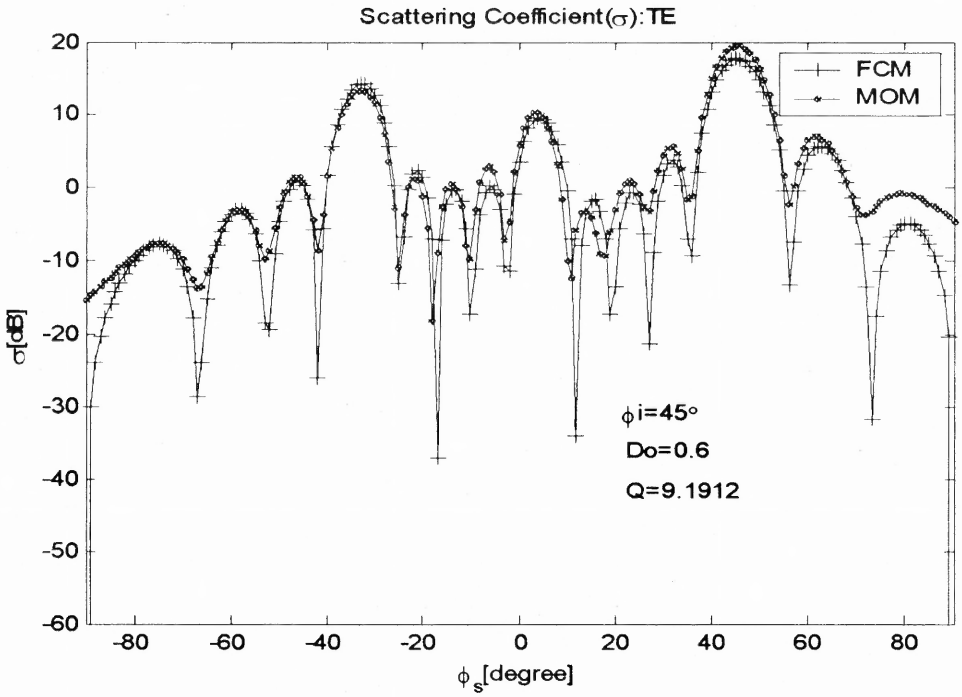

(a)

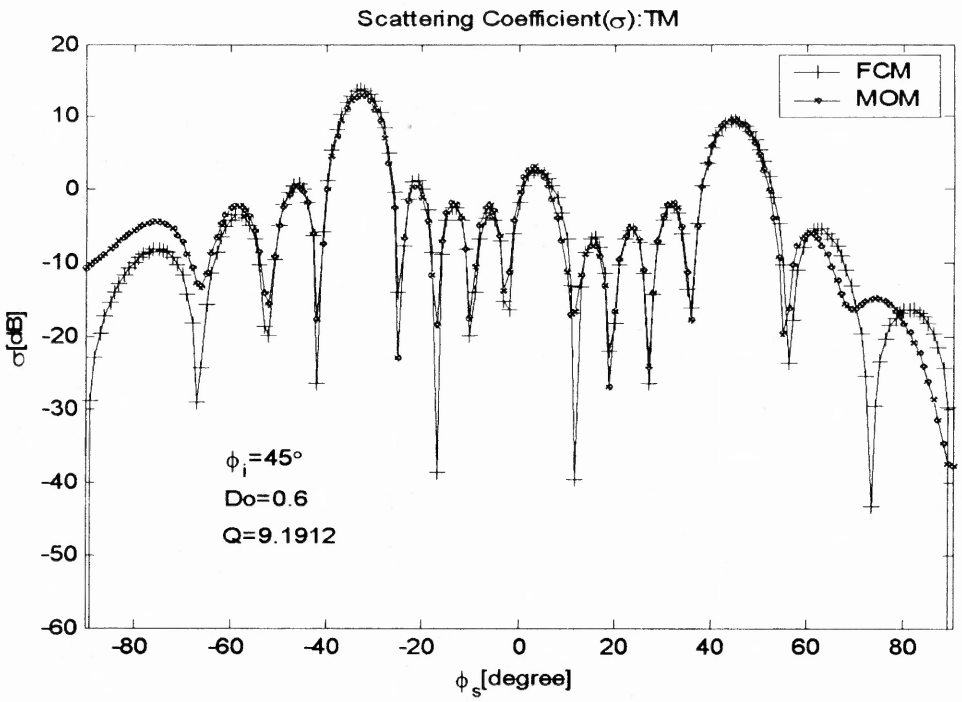

(b)

Figure 5.14 Comparison of scattering coefficients for given deterministic surface. Plots in (a) and (b) are obtained by same surface profile described in (5.14) with D_o=0.6λ. (a) TE polarization (b) TM polarization.

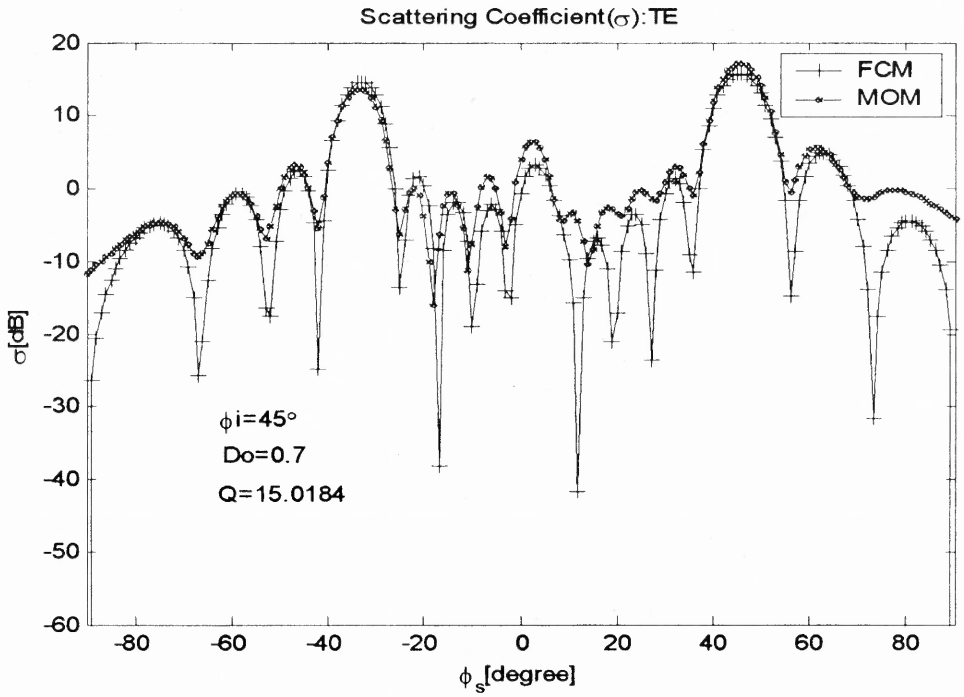

(a)

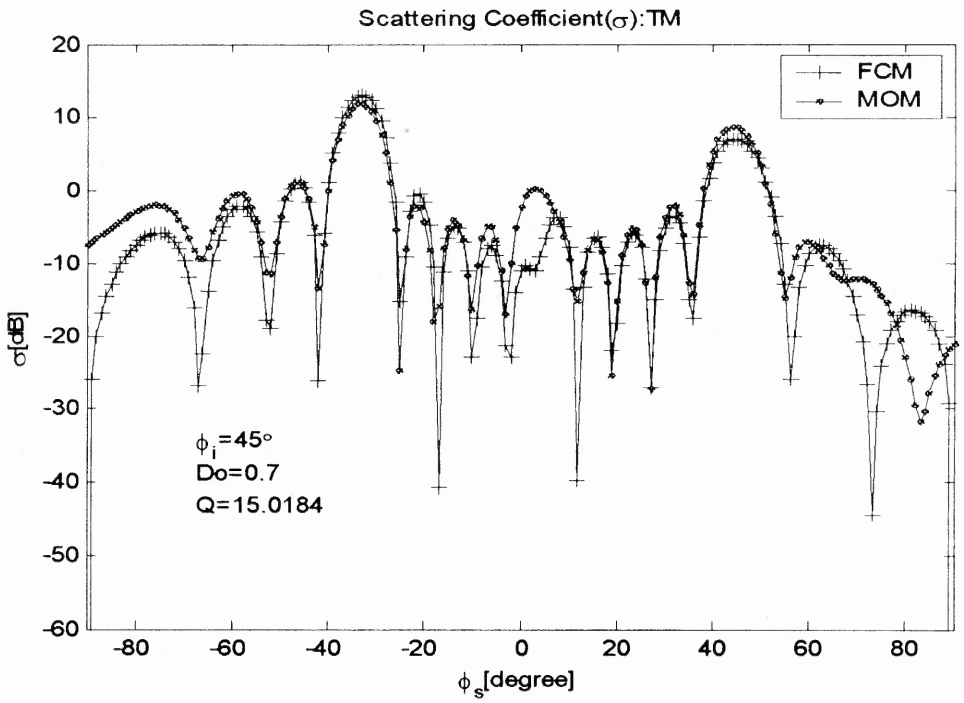

(b)

Figure 5.15 Comparison of scattering coefficients for given deterministic surface. Plots in (a) and (b) are obtained by same surface profile described in (5.14) with D_o=0.6λ. (a) TE polarization (b) TM polarization.

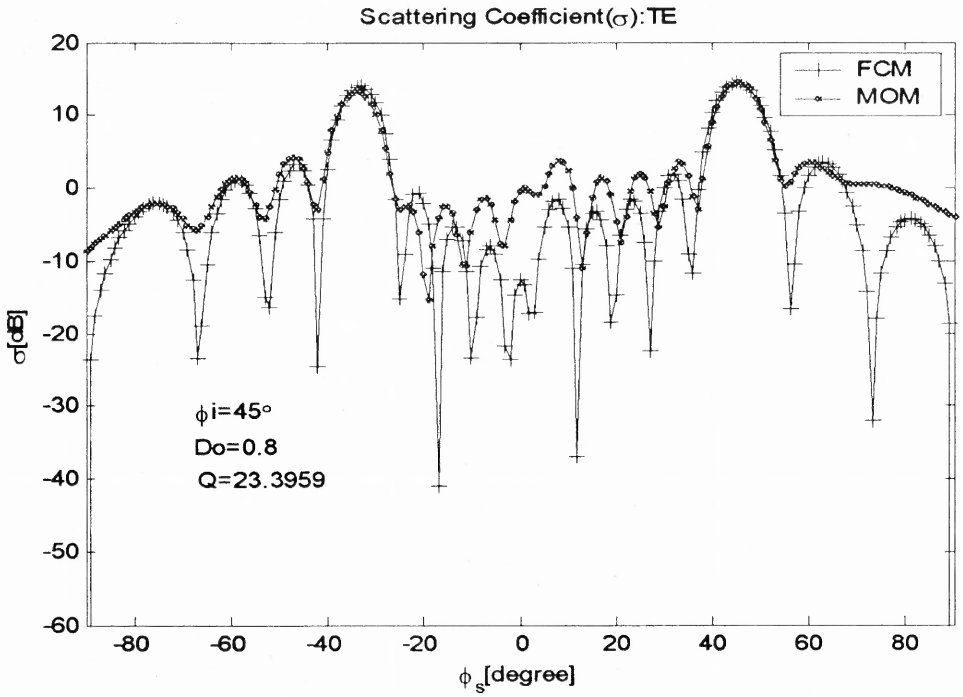

(a)

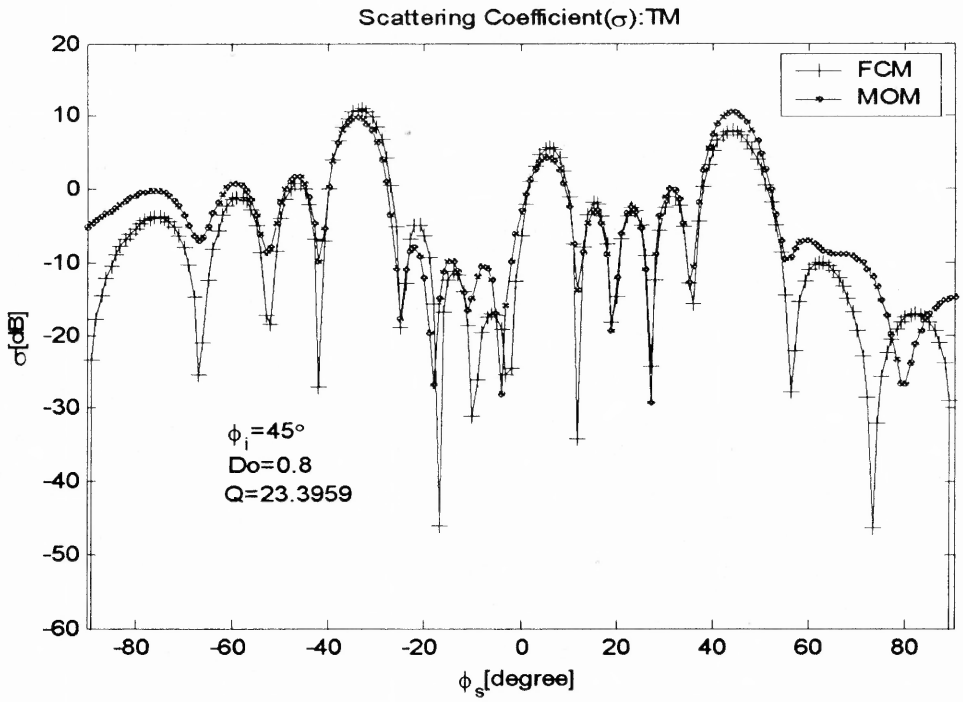

(b)

Figure 5.16 Comparison of scattering coefficients for given deterministic surface. Plots in (a) and (b) are obtained by same surface profile described in (5.14) with D_o=0.8λ. (a) TE polarization (b) TM polarization.

CHAPTER 6

CONCLUSIONS AND FUTURE WORK

A new theory for rough surface scattering has been developed. The approach is very general and can be applied to a broad range of electromagnetics problems. The more common approach to solve electromagnetics problems is by first obtaining a solution to Maxwell's equations and then satisfy the boundary conditions. Here, a zero-order solution is first obtained and fictitious current distributions are introduced to satisfy Maxwell's equations and boundary conditions. The approach is fundamentally new and is being applied to other problems. The specific problem solved here is the scattering of obliquely incident plane waves from an infinite, lossless, dielectric half-space that has a rough surface over a finite portion of its surface.

Both TE- and TM-scatter patterns are derived by using fictitious current distributions and are compared numerically to the results generated by MoM, which is a numerical technique based on solving an exact integral equation. The results of this comparison show good agreement for scattering by the random rough surfaces examined and by the deterministic surface chosen. An error criterion was developed, which depends on the surface profile and the material (the dielectric constant). The scatter patterns obtained were shown to satisfy reciprocity and to reduce to the correct solutions for plane wave scattering from perfectly conducting rough surfaces. Hence, this new full wave theory provides a very good and computationally efficient solution to the problem of scattering from rough surfaces. Further applications include studies of scattering from lossy half-spaces as well as scattering from 2-dimensional rough surfaces.

APPENDIX A

ORTHOGONALITY OF MODE FUNCTIONS

The orthogonality relationships specified in (2.21) and (3.16) need to be proved. The relationship for the mode group-1 in (2.21a) is rewritten here for convenience:

$$\int_{x=-\infty}^{+\infty} \psi_{TE}^{g1}(x,z_1;u')\psi_{TE}^{*g1}(x,z_1;u)dx = 2\pi\delta(u-u') \quad \text{for} \quad 0 \le u,u' < \infty \tag{A.1}$$

where the mode function is given by

$$\psi_{TE}^{g1}(x,z_1;u) = \begin{cases} e^{-jux} + \dfrac{u-v}{u+v}e^{ju(x-2D_1)}, & x \ge D_1 \\ \dfrac{2u}{u+v}e^{-jvx-j(u-v)D_1}, & x \le D_1 \end{cases} \tag{A.2}$$

To prove (A.1), the integral with respect to x needs to be split into two integration range, i.e., over the upper-half space ($x \ge D_1$) and over lower-half space ($x \le D_1$) since the mode function has different forms in the two regions. Thus (A.1) reduces to

$$\int_{\bar{x}=-\infty}^{0} \psi_{TE}^{g1}(\bar{x},z_1;u')\psi_{TE}^{*g1}(\bar{x},z_1;u)d\bar{x} + \int_{\bar{x}=0}^{+\infty} \psi_{TE}^{g1}(\bar{x},z_1;u')\psi_{TE}^{*g1}(\bar{x},z_1;u)d\bar{x} = 2\pi\delta(u-u') \tag{A.3}$$

where $\bar{x} = x - D_1$. Note that $u = u^*$ and $v = v^*$ since v is positive real while u is real to satisfy the relation $v = \sqrt{k_0^2(\varepsilon_r - 1) + u^2}$. Substituting (A.2) into (A.3), the first integral of the left-hand side in (A.3) can be written as

$$\int_{\bar{x}=-\infty}^{0} \psi_{TE}^{g1}(\bar{x},z_1;u')\psi_{TE}^{*g1}(\bar{x},z_1;u)d\bar{x} = e^{-j(u'-u)D_1}\frac{2u'}{u'+v'}\frac{2u}{u+v}\int_{\bar{x}=-\infty}^{0} e^{-jv'\bar{x}+jv\bar{x}}d\bar{x}$$

$$= e^{-j(u'-u)D_1}\frac{2u'}{u'+v'}\frac{2u}{u+v}\int_{\bar{x}=0}^{\infty} e^{j(v'-v)\bar{x}}d\bar{x} = e^{-j(u'-u)D_1}\frac{2u'}{u'+v'}\frac{2u}{u+v}I_0 \tag{A.4}$$

and the second integral on the left-hand side in (A.3) becomes

$$\int_{\bar{x}=0}^{+\infty} \psi_{TE}^{g1}(\bar{x}, z_1; u')\psi_{TE}^{*g1}(\bar{x}, z_1; u)d\bar{x} = e^{-j(u'-u)D_1}\left[I_A + \frac{u'-v'}{u'+v'}\frac{u-v}{u+v}I_B + \frac{u-v}{u+v}I_C + \frac{u'-v'}{u'+v'}I_D\right] \tag{A.5}$$

where,

$$I_0 = \int_{\bar{x}=0}^{\infty} e^{j(v'-v)\bar{x}}d\bar{x} \tag{A.6a}$$

$$I_A = \int_{\bar{x}=0}^{\infty} e^{j(u-u')\bar{x}}d\bar{x} \tag{A.6b}$$

$$I_B = \int_{\bar{x}=0}^{\infty} e^{-j(u-u')\bar{x}}d\bar{x} \tag{A.6c}$$

$$I_C = \int_{\bar{x}=0}^{\infty} e^{-j(u+u')\bar{x}}d\bar{x} \tag{A.6d}$$

$$I_D = \int_{\bar{x}=0}^{\infty} e^{j(u+u')\bar{x}}d\bar{x} \tag{A.6e}$$

The integrals in (A.4) and (A.6) have the form $\int_0^{\infty} e^{j\kappa x}d\kappa$ which can be evaluated by using the relation as follows [20]:

$$-j\lim_{K\to\infty}\int_0^K e^{j\kappa x}dk = \lim_{K\to\infty}\frac{1-e^{jKx}}{x} = \lim_{K\to\infty}\left[\frac{1-\cos Kx}{x} - j\frac{\sin Kx}{x}\right] \equiv P\left(\frac{1}{x}\right) - j\pi\delta(x) \tag{A.7}$$

Note that $P\left(\frac{1}{x}\right)$ is the principal value of $1/x$; it is defined to equal to $1/x$ when $x \neq 0$, but to vanish for $x=0$. Using (A.7), the integral in (A.4) reduces to

$$I_0 = -jP\left(\frac{1}{v-v'}\right) + \pi\delta(v-v') = -jP\left(\frac{v+v'}{u^2-u'^2}\right) + \pi\frac{v}{u}\delta(u-u') \tag{A.8a}$$

which is obtained by using the following relationship:

$$v^2 - v'^2 = u^2 - u'^2$$

and the property of the Dirac delta function:

$$\delta(ax) = \frac{1}{|a|}\delta(x).$$

Integrals in (A.6) are evaluated by using (A.7):

$$I_A = jP\left(\frac{1}{u-u'}\right) + \pi\delta(u-u') \tag{A.8b}$$

$$I_B = -jP\left(\frac{1}{u-u'}\right) + \pi\delta(u-u') \tag{A.8c}$$

$$I_C = -jP\left(\frac{1}{u+u'}\right) + \pi\delta(u+u') \tag{A.8d}$$

$$I_D = jP\left(\frac{1}{u+u'}\right) + \pi\delta(u+u') \tag{A.8e}$$

Substituting (A.8) into (A.4)-(A.5) reduces the left-hand side of (A.3) to

$$2\pi\left[e^{-j(u'-u)D_1}\right]\delta(u-u') = 2\pi\delta(u-u') \tag{A.9}$$

Thus (A.1) is proved for all $0 \le u, u' < \infty$. All the other orthogonality relationships in (2.21) can be shown similarly.

The orthogonality relationships for the mode functions of the TM case are written in (3.16):

$$\int_{x=-\infty}^{+\infty} \varepsilon_r(x)\psi_{TM}^{g1}(x,z_1;u')\psi_{TM}^{*g1}(x,z_1;u)dx = 2\pi\delta(u-u') \tag{A.10}$$

where

$$\varepsilon_r(x) = \begin{Bmatrix} 1, & x > D_1 \\ \varepsilon_r, & x < D_1 \end{Bmatrix} \tag{A.11}$$

Since the mode function takes different forms in the two regions, (A.10) together with (A.11) is written as follows

$$\int_{\bar{x}=-\infty}^{0} \varepsilon_r\psi_{TM}^{g1}(\bar{x},z_1;u')\psi_{TM}^{*g1}(\bar{x},z_1;u)d\bar{x} + \int_{\bar{x}=0}^{+\infty} \psi_{TM}^{g1}(\bar{x},z_1;u')\psi_{TM}^{*g1}(\bar{x},z_1;u)d\bar{x} = 2\pi\delta(u-u') \tag{A.12}$$

where $\bar{x} = x - D_1$ and

$$\psi_{TM}^{g1}(x,z_1;u) = \begin{Bmatrix} e^{-jux} + \dfrac{\varepsilon_r u - v}{\varepsilon_r u + v} e^{ju(x-2D_1)}, & x > D_1 \\ \dfrac{2u}{\varepsilon_r u + v} e^{-jvx - j(u-v)D_1}, & x < D_1 \end{Bmatrix} \tag{A.13}$$

which is given by (3.15a). Substituting (A.13) into (A.12), the first integral of the left-hand side in (A.12) reduces to

$$\int_{\bar{x}=-\infty}^{0} \varepsilon_r\psi_{TM}^{g1}(\bar{x},z_1;u')\psi_{TM}^{*g1}(\bar{x},z_1;u)d\bar{x} = e^{-j(u'-u)D_1}\,\varepsilon_r \frac{2u'}{\varepsilon_r u' + v'}\frac{2u}{\varepsilon_r u + v}\int_{\bar{x}=-\infty}^{0} e^{-jv'\bar{x}+jv\bar{x}}d\bar{x}$$

$$= e^{-j(u'-u)D_1}\varepsilon_r \frac{2u'}{\varepsilon_r u' + v'}\frac{2u}{\varepsilon_r u + v}\int_{\bar{x}=0}^{\infty} e^{j(v'-v)\bar{x}}d\bar{x} = e^{-j(u'-u)D_1}\varepsilon_r \frac{2u'}{\varepsilon_r u' + v'}\frac{2u}{\varepsilon_r u + v} I_0 \tag{A.14}$$

and the second integral on the left-hand side in (A.12) becomes

$$\int_{\bar{x}=0}^{+\infty} \psi_{TM}^{g1}(\bar{x}, z_1; u')\psi_{TM}^{*g1}(\bar{x}, z_1; u)d\bar{x}$$
$$= e^{-j(u'-u)D_1}\left[I_A + \frac{\varepsilon_r u' - v'}{\varepsilon_r u' + v'}\frac{\varepsilon_r u - v}{\varepsilon_r u + v}I_B + \frac{\varepsilon_r u - v}{\varepsilon_r u + v}I_C + \frac{\varepsilon_r u' - v'}{\varepsilon_r u' + v'}I_D\right] \quad \text{(A.15)}$$

where I_0, I_A, I_B, I_C and I_D are given by (A.8). Substituting (A.8) into (A.14)-(A.15) reduces the left-hand side of (A.10) to

$$2\pi\left[e^{-j(u'-u)D_1}\right]\delta(u-u') = 2\pi\delta(u-u') \quad \text{(A.9)}$$

Thus (A.10) is proved for all $0 \le u, u' < \infty$. All the other orthogonality relationships in (3.16) can be shown similarly.

APPENDIX B

METHOD OF MOMENTS (MoM)

The MoM is widely used to evaluate the field scattered by metallic objects in antenna and radar applications, but its use in the evaluation of scattering from rough dielectric surfaces is not so widespread and is more recent [6]. In this section, MoM is recalled and summarized.

For the TE case, the surface electric field can be evaluated by solving the following equation pair that is obtained from application of the equivalence theorem [19].

$$E_y^i(\boldsymbol{r}) = \frac{1}{2}E_y(\boldsymbol{r}) + \int_l \{jw\mu_0 G_0(\boldsymbol{r},\boldsymbol{r}')J_y(\boldsymbol{r}') + E_y(\boldsymbol{r}')[\hat{\boldsymbol{n}}' \cdot \nabla G_0(\boldsymbol{r},\boldsymbol{r}')]\}dl' \qquad \text{(B.1a)}$$

$$0 = \frac{1}{2}E_y(\boldsymbol{r}) - \int_l \{jw\mu_0 G_1(\boldsymbol{r},\boldsymbol{r}')J_y(\boldsymbol{r}') + E_y(\boldsymbol{r}')[\hat{\boldsymbol{n}}' \cdot \nabla G_1(\boldsymbol{r},\boldsymbol{r}')]\}dl' \qquad \text{(B.1b)}$$

where E_y^i and E_y are the incident and total electric field, respectively. J_y is the equivalent electric surface current density found by using $\boldsymbol{J}_s = \hat{n} \times \boldsymbol{H} = \hat{y}J_y$. Both $\boldsymbol{n}$ and $\boldsymbol{n}'$

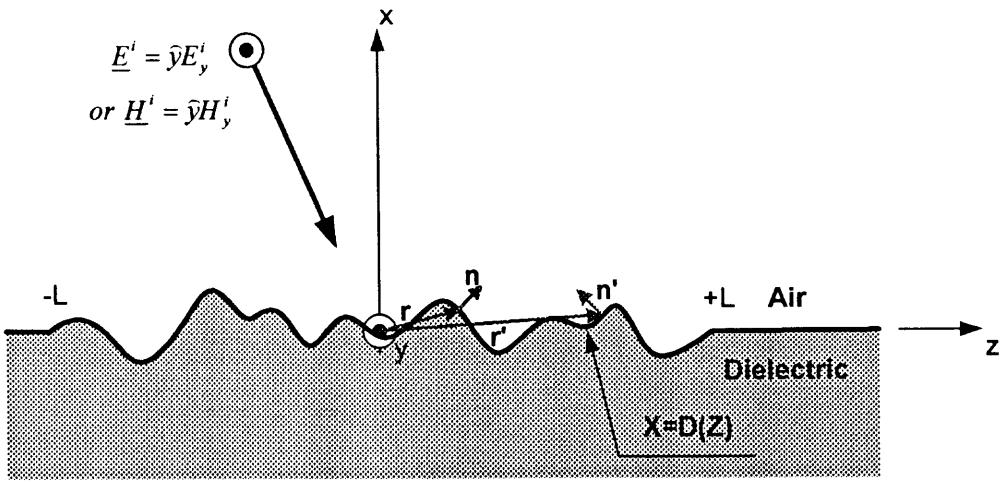

Figure B.1 Geometry for MoM

are unit normal vectors to the surface, matching to the to the terminal point of the vector $\boldsymbol{r}$, from the origin to the observation point, and $\boldsymbol{r}'$, from the origin to the source point, respectively. Both $\boldsymbol{r}$ and $\boldsymbol{r}'$ touch the surface profile $D(z)$; see Figure 5.2. G_0 and G_1 are the Green's function in 2-dimensional space described by

$$G_{0,1}(\boldsymbol{r}-\boldsymbol{r}') = -\frac{j}{4}H_0^{(2)}(k_{0,1}\,|\boldsymbol{r}-\boldsymbol{r}'|) \tag{B.2}$$

where k_0 and k_1 are the wavenumbers in the upper and lower half-space, respectively. $H_0^{(2)}(\cdot)$ is the zero-order Hankel function of the second kind.

With rectangular pulse basis function and the point matching method, (B.1) can be converted into the matrix equation:

$$\begin{bmatrix} Z^{11} & Z^{12} \\ Z^{21} & Z^{22} \end{bmatrix}\begin{bmatrix} E_y \\ J_y \end{bmatrix} = \begin{bmatrix} E_y^i \\ 0 \end{bmatrix} \tag{B.3}$$

The unknowns E_y and J_y are found by following the determination of the explicit form of the elements [19]

$$Z_{mn}^{11} = \begin{cases} \dfrac{1}{2}, & m = n \\ (\hat{\boldsymbol{n}}_n \cdot \hat{\boldsymbol{R}}_{mn})\dfrac{jk_0}{4}H_1^{(2)}(k_0\,|\boldsymbol{r}_m - \boldsymbol{r}_n|)W_n\Delta z_n, & m \neq n \end{cases} \tag{B.4a}$$

$$Z_{mn}^{12} = jk_0\eta_0\begin{cases} -\dfrac{j}{4}\left(1 - \dfrac{2j}{\pi}\ln\dfrac{\gamma k_0 W_n \Delta z_n}{4e}\right), & m = n \\ -\dfrac{j}{4}H_0^{(2)}(k_0\,|\boldsymbol{r}_m - \boldsymbol{r}_n|)W_n\Delta z_n, & m \neq n \end{cases} \tag{B.4b}$$

$$Z_{mn}^{21} = \begin{cases} \dfrac{1}{2}, & m = n \\ -(\hat{\boldsymbol{n}}_n \cdot \hat{\boldsymbol{R}}_{mn})\dfrac{jk_1}{4}H_1^{(2)}(k_0\,|\boldsymbol{r}_m - \boldsymbol{r}_n|)W_n\Delta z_n, & m \neq n \end{cases} \tag{B.4c}$$

$$Z_{mn}^{22} = jk_0\eta_0 \begin{cases} \frac{j}{4}\left(1 - \frac{2j}{\pi}\ln\frac{\gamma k_0 W_n \Delta z_n}{4e}\right), & m = n \\ \frac{j}{4}H_0^{(2)}(k_1 |\boldsymbol{r}_m - \boldsymbol{r}_n|)W_n \Delta z_n, & m \neq n \end{cases} \tag{B.4d}$$

where $W_n = \sqrt{1 + \left(\frac{dx}{dz}\right)_n^2}$, $\hat{\boldsymbol{R}}_{mn} = \frac{\boldsymbol{r}_m - \boldsymbol{r}_n}{|\boldsymbol{r}_m - \boldsymbol{r}_n|}$ and $\Delta z_n = \Delta z = \frac{2L}{N}$. γ is the exponential of the Euler's constant, i.e., $\gamma \cong \exp(0.5772)$. n and m are indices with regard to source and observation points in the interval [1,N], respectively. Each size of the sub-matrix $Z^{11\text{-}22}$ is $N \times N$ so that the total size of Z is $2N \times 2N$. After solving (B.3) using (B.4), the far zone scattered electric field in the upper half-space is evaluated by using

$$E_y^s(\rho) = \frac{k_0}{\sqrt{8\pi k_0 \rho}} e^{-jk_0\rho + j\pi/4} \int_l \left[\eta_0 J_y(\boldsymbol{r}') - (\hat{\boldsymbol{n}}' \cdot \hat{\boldsymbol{n}}_s)E_y(\boldsymbol{r}')\right] e^{jk_0\hat{\boldsymbol{n}}_s \cdot \boldsymbol{r}'} W dz' \tag{B.5}$$

Note that $\boldsymbol{r}' = \hat{z}z' + \hat{x}x'$ reaches points on the surface profile, ρ is a radial distance to a point in the far zone and $\hat{\boldsymbol{n}}_s$ is the unit vector that specifies the scatter direction.

For the TM case with $\boldsymbol{H}^i = H_y^i$, (B.1) can be simply changed in view of the duality theorem. The electric fields and current densities must be replaced by magnetic ones, for example, J_y is replaced by M_y in $\boldsymbol{M}_s = -\hat{n} \times \boldsymbol{E} = \hat{y}M_y$. In addition, μ_0 is replaced by ε_0 in (B.1a) and by ε_d in (B.1b), hence,

$$H_y^i(\boldsymbol{r}) = \frac{1}{2}H_y(\boldsymbol{r}) + \int_l \left\{jw\varepsilon_0 G_0(\boldsymbol{r},\boldsymbol{r}')K_y(\boldsymbol{r}') + H_y(\boldsymbol{r}')[\hat{\boldsymbol{n}}' \cdot \nabla G_0(\boldsymbol{r},\boldsymbol{r}')]\right\} dl' \tag{B.6a}$$

$$0 = \frac{1}{2}H_y(\boldsymbol{r}) - \int_l \left\{jw\varepsilon_1 G_1(\boldsymbol{r},\boldsymbol{r}')M_y(\boldsymbol{r}') + H_y(\boldsymbol{r}')[\hat{\boldsymbol{n}}' \cdot \nabla G_1(\boldsymbol{r},\boldsymbol{r}')]\right\} dl' \tag{B.6b}$$

The TM-polarized far zone scattered magnetic field in the upper half-space then obtained from

$$H_y^s(\rho) = \frac{k_0}{\sqrt{8\pi k_0 \rho}} e^{-jk_0\rho + j\pi/4} \int_l \left[\frac{M_y(\boldsymbol{r}')}{\eta_0} - (\hat{\boldsymbol{n}}' \cdot \hat{\boldsymbol{n}}_s) H_y(\boldsymbol{r}') \right] e^{jk_0 \hat{\boldsymbol{n}}_s \cdot \boldsymbol{r}'} W dz' \tag{B.7}$$

REFERENCES

1. A. G. Voronovich, *Wave Scattering from Rough Surfaces*. Berlin: Springer-Verlag, 1994.

2. D. P. Winebrenner and A. Ishimaru, "Application of the phase-perturbation technique to randomly rough surfaces," *J. Opt. Soc. Am. A*, vol. 2, no. 12, 2285-2293, 1985.

3. A. G.Voronovich, "Small-slope approximation in wave scattering by rough surfaces," *Sov. Phs. JETP*, vol. 62, no. 1, 65-70, 1985.

4. E. Bahar, "Electromagnetic wave propagation in inhomogeneous multi-layered structures of arbitrary thickness-full wave solutions," *J. Math. Phys.*, vol. 14, no. 8, pp. 1030-1036, 1973.

5. R, E. Collin, "Electromagnetic scattering from perfectly conducting rough surfaces," *IEEE Trans. Antennas Propag.*, vol. AP-40, no. 12, pp. 1466-1477, 1992.

6. A. Garcia-Valenzuela and R. E. Collin, "The local spectral expansion method for scattering from perfectly conducting surfaces rough in one dimension" *J. EM Waves and Appl.*, vol. 11, pp 37-63, 1977.

7. C. A. Balanis, *Advanced Engineering Electromagnetics*. New York: John Wiley & Sons, 1989.

8. A. Ishimaru, *Electromagnetic Wave Propagation, Radiation, and Scattering*. New Jersey: Prentice Hall, 1991.

9. J. Ogilvy, *Theory of Wave Scattering from Random Rough Surfaces*. Philadelphia: Institute of Physics, 1991.

10. A. Triolo, *A full wave method for rough surface scattering using fictitious current distributions*. Ph.D. dissertation, NJIT, 1996.

11. L. B. Felsen and N. Marcuvitz, *Radiation and Scattering of Waves*. New York: IEEE Press, 1994.

12. M. Abramowitz and I. Stegun, *Handbook of Mathematical Functions*. New York: Dover Publications, 1965.

13. A. T. De Hoop, Chapter 6 "General considerations on the integral-equation of diffraction problems" in *Modern Topics in Electromagnetics and Antennas*. England: Peter Peregrinus, 1977.

14. A. Paupoulis, *Probability, Random Variables, and Stochastic Processes.* New York: McGraw Hill, 3rd Ed., 1991.

15. A. Neon-Garcia, *Probability and Random Processes for Electrical Engineering.* Addison-Wesley, 2nd Ed., 1994.

16. A. J. Pozzio and E.K. Miller, Ch 4 of *Computer Techniques for Electromagnetics,* Integral equation solution of three dimensional scattering problems, New York, Pergamon, 1973.

17. L. Tsang, J. A. Kong, K-H. Ding, and C. O. Ao, *Scattering of Electromagnetic Waves: Numerical Simulations,* New York, Wiley, 2001.

18. G. Franceschetti, A. Iodice and D. Riccio, Scattering from dielectric random fractal surfaces via method of moments, *IEEE Trans. Geosci. Remote Sensing*, vol. 38, no. 4, pp. 1644-1655, Jul. 2000.

19. M. F. Chen and S-Y. Bay, Computer simulation of wave scattering from a dielectric random surface in two dimensions- cylindrical case, *J. Electromagn. Waves Applicat.*, vol. 4, no. 10, pp. 963-982, 1990.

20. W. Heitler, *The Quantum Theory of Radiation.* New York: Dover, 1984.

21. E. I. Thorsos, "The validity of the Kirchhoff approximation for rough surface scattering using a Gaussian roughness spectrum", *J. Acoust. Soc. Am.*, vol. 83, no.1, pp. 78-92, 1988.

22. E. I. Thorsos and D. R. Jackson, "The validity of the perturbation approximation for rough surface scattering using a Gaussian roughness spectrum", *J. Acoust. Soc.* Am., vol. 86, no. 1, pp. 261-277, 1989.

23. E. I. Thorsos and D. P. Winebrenner, "An examination of the 'full-wave' method for rough surface scattering in the case of small roughness", *J. Geophys. Res.*, vol. 92, no. C9, pp. 17,107-17,121, 1991.